



National Library  
of Canada

Bibliothèque nationale  
du Canada

Acquisitions and  
Bibliographic Services Branch

Direction des acquisitions et  
des services bibliographiques

395 Wellington Street  
Ottawa, Ontario  
K1A 0N4

395, rue Wellington  
Ottawa (Ontario)  
K1A 0N4

*Your file - Votre référence*

*Our file - Notre référence*

## NOTICE

## AVIS

The quality of this microform is heavily dependent upon the quality of the original thesis submitted for microfilming. Every effort has been made to ensure the highest quality of reproduction possible.

La qualité de cette microforme dépend grandement de la qualité de la thèse soumise au microfilmage. Nous avons tout fait pour assurer une qualité supérieure de reproduction.

If pages are missing, contact the university which granted the degree.

S'il manque des pages, veuillez communiquer avec l'université qui a conféré le grade.

Some pages may have indistinct print especially if the original pages were typed with a poor typewriter ribbon or if the university sent us an inferior photocopy.

La qualité d'impression de certaines pages peut laisser à désirer, surtout si les pages originales ont été dactylographiées à l'aide d'un ruban usé ou si l'université nous a fait parvenir une photocopie de qualité inférieure.

Reproduction in full or in part of this microform is governed by the Canadian Copyright Act, R.S.C. 1970, c. C-30, and subsequent amendments.

La reproduction, même partielle, de cette microforme est soumise à la Loi canadienne sur le droit d'auteur, SRC 1970, c. C-30, et ses amendements subséquents.

**Canada**

**SINTERING OF Ti-TiC  
METAL MATRIX COMPOSITES**

by

**Stéphane Debouzy**

**A Thesis Submitted to the Faculty of Graduate Studies  
in Partial Fulfillment of the Requirements for the  
Degree of Master of Engineering**

**Department of Mining and Metallurgical Engineering  
McGill University  
Montreal, Canada  
January, 1994**

©Stéphane Debouzy, 1994



National Library  
of Canada

Bibliothèque nationale  
du Canada

Acquisitions and  
Bibliographic Services Branch

Direction des acquisitions et  
des services bibliographiques

395 Wellington Street  
Ottawa, Ontario  
K1A 0N4

395, rue Wellington  
Ottawa (Ontario)  
K1A 0N4

Your file / Votre référence

Our file / Notre référence

THE AUTHOR HAS GRANTED AN IRREVOCABLE NON-EXCLUSIVE LICENCE ALLOWING THE NATIONAL LIBRARY OF CANADA TO REPRODUCE, LOAN, DISTRIBUTE OR SELL COPIES OF HIS/HER THESIS BY ANY MEANS AND IN ANY FORM OR FORMAT, MAKING THIS THESIS AVAILABLE TO INTERESTED PERSONS.

L'AUTEUR A ACCORDE UNE LICENCE IRREVOCABLE ET NON EXCLUSIVE PERMETTANT A LA BIBLIOTHEQUE NATIONALE DU CANADA DE REPRODUIRE, PRETER, DISTRIBUER OU VENDRE DES COPIES DE SA THESE DE QUELQUE MANIERE ET SOUS QUELQUE FORME QUE CE SOIT POUR METTRE DES EXEMPLAIRES DE CETTE THESE A LA DISPOSITION DES PERSONNE INTERESSEES.

THE AUTHOR RETAINS OWNERSHIP OF THE COPYRIGHT IN HIS/HER THESIS. NEITHER THE THESIS NOR SUBSTANTIAL EXTRACTS FROM IT MAY BE PRINTED OR OTHERWISE REPRODUCED WITHOUT HIS/HER PERMISSION.

L'AUTEUR CONSERVE LA PROPRIETE DU DROIT D'AUTEUR QUI PROTEGE SA THESE. NI LA THESE NI DES EXTRAITS SUBSTANTIELS DE CELLE-CI NE DOIVENT ETRE IMPRIMES OU AUTREMENT REPRODUITS SANS SON AUTORISATION.

ISBN 0-315-99961-6

Canada

*A Pépé*

*...Dans l'Auvergne de mes vacances  
Je gambadais dans la campagne vraie  
Où senteurs étaient mon enfance  
Où genêts en fleur et bovidés  
Dans les prés jolis sentant le bon foin  
Étaient en harmonie avec l'été...*

## ABSTRACT

Particulate Reinforced Metal Matrix Composites, or PMMCs, consist of ceramic particulates dispersed in a metal matrix. Powder metallurgy (P/M) techniques are often employed to fabricate these materials. P/M offers the simplest way to ensure good distribution of reinforcement within the matrix. In this work, TiC particles have been dispersed in a Ti matrix, yielding a composite which combines the high hardness and abrasive nature of the ceramic phase with the refractory, metallic properties of Ti.

The microstructure of this material has been investigated for composites having various TiC content (2.5wt%-20wt%). Furthermore, the effect of sintering temperature and time on the microstructural evolution was investigated. The addition of TiC was seen to enhance the sinterability of Ti, making it possible to attain theoretical densities > 99%. Results show that the optimum density is obtained using 2.5 to 5 wt%TiC at a temperature of 1440-1480°C for 2 hours. This study also illustrates the decrease in the microhardness of the TiC particles due to carbon diffusion from TiC into Ti matrix at high sintering temperatures. On the other hand, the addition of TiC significantly increases the overall hardness compare to that of pure Ti.

## RÉSUMÉ

Les composites à matrice métallique renforcée par des particules ("Particulate Reinforced Metal Matrix Composites" ou PMMCs) sont composés d'une matrice métallique au sein de laquelle sont dispersées des particules de céramique. La métallurgie des poudres est une technique simple, et de fait très employée dans la fabrication de ce type de matériaux. De surcroît, elle permet d'aboutir à une bonne répartition des particules au sein de la matrice. Pour cette thèse des particules de carbure de titane (TiC) ont été dispersées au sein d'une matrice de titane (Ti). Ce composite associe la dureté exceptionnelle du TiC avec les propriétés métalliques et réfractaires du Ti.

La microstructure de ce matériau a été analysée pour différentes teneurs en TiC variant de 2.5 à 20% en poids. L'influence de la température et du temps de frittage sur l'évolution de la microstructure a également été étudiée. Le pouvoir de frittage du Ti s'est vu amélioré par l'ajout de particules de TiC, permettant d'atteindre des densités supérieures à 99% de la densité théorique. Les résultats ont montré un optimum de densité se situant à une température de frittage de 1440°C-1480°C pour un temps de frittage de 2 heures, et ce pour une teneur de 2.5 à 5% en poids de particules de TiC. Cette étude a également permis d'observer une diminution de la microdureté des particules de TiC à haute température de frittage. Cette diminution a été imputée à la diffusion du carbone du TiC vers la matrice de Ti. Finalement, l'ajout de particules de TiC augmente de manière significative la macrodureté du composite par rapport à celle du titane pur.

## ACKNOWLEDGMENTS

I would like to express my sincere gratitude to Professor R.A.L. Drew who gave me the opportunity to come to study at McGill University and to discover this great city of Montréal as well as its people. I thank him also for his valuable help, guidance and understanding. I would like to thank Professor M.D. Pugh for his help in the form of co-supervision during the first six months of my thesis work.

The author would also like to express his appreciation to Alcan International and McGill University for the financial support. The author is grateful to Mrs. H. Campbell and Mr. Glenn Poirier for their technical assistance in using the SEM lab and the electron microprobe analyzer as well as for their kindness.

A special mention goes to my colleagues involved in the Department for their willingness to always discuss numerous questions that I might have had not only regarding the work but also about other aspects of life during my stay at McGill.

Finalement, je voudrais en profiter pour dire ô combien je suis heureux d'avoir connu à Montréal mes amis d'aujourd'hui qui ont toujours su m'écouter, m'encourager et m'aimer. Que Pascale, Claudie, J.C., Régis, Hughes, Sophie, Yann, François, Pat., Thierry, Zickie, Violetta et bien d'autres trouvent en ces mots quelque chaleur pour eux dans mon cœur. Je remercie également mes parents et Cécile pour leur soutien, patience et compréhension tout au long de ces deux années et plus passées au Canada...

## TABLE OF CONTENTS

ABSTRACT	
RESUME	
ACKNOWLEDGMENTS	
TABLE OF CONTENTS	
LIST OF FIGURES	i
LIST OF TABLES	iii
NOMENCLATURE	iv
CHAPTER 1 : INTRODUCTION	1
1.1 HISTORICAL BACKGROUND	1
1.2 METAL-MATRIX COMPOSITES	2
1.3 APPLICATIONS	3
CHAPTER 2 : LITERATURE REVIEW	5
2.1 DEFINITION OF METAL MATRIX COMPOSITES	5
2.2 MATRIX MATERIALS	6
2.3 PHYSICAL AND MECHANICAL PROPERTIES OF PMMCs	7
2.4 REINFORCEMENT SELECTION	9
2.5 MATRIX-CERAMIC INTERFACES	11
2.6 CURRENTLY AVAILABLE Ti MATRIX COMPOSITES	12
2.7 Ti-TiC CHEMISTRY AND CRYSTALLOGRAPHIC PROPERTIES	13
2.7.1 The Ti-TiC phase diagram	13
2.7.2 Structure of Ti and TiC	15
2.8 Ti AND TiC POWDER PRODUCTION	17
2.8.1 Production of Ti powder	17
2.8.2 Production of TiC powder	18
2.9 Ti-TiC COMPOSITES	19
2.9.1 General background	19
2.9.2 Current research on Ti-TiC PMMCs	21

2.10	Ti6Al4V-TiC COMPOSITES	23
2.11	FUNDAMENTALS OF CONSOLIDATION AND SINTERING	24
2.11.1	Introduction	24
2.11.2	Driving forces and material transport in sintering	25
2.11.3	Homogenization during sintering	30
2.12	COMMERCIAL PROCESSING, CONSOLIDATION AND SINTERING	31
2.12.1	Composite powder metallurgical techniques	32
2.12.2	High-energy-high rate processes	34
2.13	Ti POWDER METALLURGY	34
CHAPTER 3 : OBJECTIVES		35
CHAPTER 4 : EXPERIMENTAL PROCEDURE		36
4.1	STARTING MATERIALS	36
4.2	POWDER PREPARATION MEASUREMENTS	39
4.2.1	Particle size characteristics	39
4.2.1.1	Particle size distribution	
4.2.1.2	Screening	
4.2.1.3	Sedimentation	
4.2.2	Powder preparation	41
4.3	GREEN COMPACT FABRICATION	43
4.3.1	Die-pressing	43
4.3.2	Isostatic compaction	44
4.4	SINTERING	44
4.5	MATERIAL CHARACTERIZATION	47
4.5.1	Measurement of density	47
4.5.2	Porosimetry measurements	48
4.5.2.1	Mercury porosimeter	
4.5.2.2	Theory	
4.5.2.3	Principles of operation	
4.5.3	Preparation for microscopic examination	49
4.5.4	X-ray diffraction analysis (XRD)	50
4.5.5	SEM analysis	50
4.5.6	X-ray mapping	51
4.5.7	Image analysis	52
4.5.8	Microprobe analysis	53
4.5.9	Vickers microhardness and Rockwell testing	54

CHAPTER 5 : RESULTS AND DISCUSSION	55
5.1 POWDER ANALYSIS AND PREPARATION	55
5.2 SINTERING	64
5.3 MICROSTRUCTURE	82
5.4 MICROPROBE ANALYSIS AND CARBON DIFFUSION STUDY	91
CHAPTER 6 : CONCLUSIONS AND RECOMMENDATIONS	102
REFERENCES	105
APPENDICES	

## LIST OF FIGURES

- Figure 1.1 Various P/M components
- Figure 2.1 Phase diagrams of the Ti-TiC system as a function of (a) weight percent C and (b) atomic ratio C/Ti
- Figure 2.2 B1 structure of TiC
- Figure 2.3 Density of Ti/10%TiC and pure Ti vs temperature
- Figure 2.4 Microhardness of TiC particles Ti/10%TiC PMMC vs temperature
- Figure 2.5 Macrohardness of the Ti-TiC PMMCs vs TiC content
- Figure 2.6 The two classes of sintering mechanisms as applied to sphere-sphere sintering
- Figure 2.7 Interparticle bond development during sintering (pore spheroidization)
- Figure 2.8 The ALCOA process
- Figure 2.9 The CERACON process
- Figure 4.1 SEM micrograph of as-received Ti powder
- Figure 4.2 SEM micrograph of TiC powder
- Figure 4.3 Functional diagram of the Sedigraph
- Figure 4.4 Schematic of an attrition mill
- Figure 4.5 Processing route for attrition milling powder
- Figure 4.6 Processing route for fabricating pressed pellets
- Figure 4.7 Water-cooled graphite element furnace
- Figure 4.8 A typical time/temperature furnace cycle
- Figure 5.1 Sedigraph of (a) Ti and (b) TiC
- Figure 5.2 Histogram plot of the particle size
- Figure 5.3 Cumulative particle size distribution plot
- Figure 5.4 (a) Pure Ti isopressed compact ( $\times 350$ )  
(b) Pure Ti isopressed compact ( $\times 1,300$ )
- Figure 5.5 (a) Cumulative volume and (b) porosity vs pore size of a pure Ti and a 20wt%TiC green compacts isopressed at 207 MPa
- Figure 5.6 Relative density of pure Ti attrition milled and non attrition milled at 1440°C
- Figure 5.7 Relative density vs temperature for (a) 0% (b) 5% (c) 10% and (d) 20%
- Figure 5.8 Change in relative density with time at (a) 1300°C (b) 1440°C (c) 1480°C and (d) 1600°C
- Figure 5.9 Change in relative density with TiC content
- Figure 5.10 Comparison between the *Archimedes* densities and the *Image analysis* densities (a) at 1440°C and (b) for 2 hours
- Figure 5.11 (a) Non-polished Ti-5wt%TiC sintered at 1300°C/4 hrs ( $\times 20$ )  
(b) Well sintered particles in the middle of the sample ( $\times 200$ )  
(c) Poorly-sintered structure at the edge of the sample ( $\times 200$ )  
(d) Ti-5wt%TiC sintered at 1300°C/ 4 hrs ( $\times 370$ ) showing a higher porosity of  $\sim 100 \mu\text{m}$  at the surface  
(e) Ti-5wt%TiC sintered at 1480°C/2 hrs ( $\times 650$ ) showing a higher porosity of  $\sim 30 \mu\text{m}$  at the surface

- Figure 5.12 Microhardness of TiC particles vs temperature for (a) 5%TiC and (b) 10%TiC and time for (c) 5%TiC and (d) 10%TiC
- Figure 5.13 Microhardness of Ti matrix vs temperature for (a) 5%TiC and (b) 10%TiC and time for (c) 5%TiC and (d) 10%TiC
- Figure 5.14 Microhardness of TiC vs TiC content for (a) 0.5 hour and (b) 2 hours
- Figure 5.15 (a) Hardness vs TiC content (t=2 hrs)  
(b) Hardness vs sintering temperature (t=2 hrs)
- Figure 5.16 (a) Ti-TiC 10wt% 1300°C/0.5 hr (× 400)  
(b) Ti-TiC 10wt% 1300°C/4 hrs (× 200)  
(c) Ti-TiC 10wt% 1440°C/0.5 hr (× 200)  
(d) Ti-TiC 10wt% 1440°C/4 hrs (× 200)  
(e) Ti-TiC 10wt% 1600°C/0.5 hr (× 400)  
(f) Ti-TiC 10wt% 1600°C/4 hrs (× 200)
- Figure 5.17 (a) Agglomerates of TiC in a Ti-10wt%TiC sintered at 1300°C/0.5 hr (× 2,000)
- Figure 5.18 Ti-2.5wt%TiC sintered for 1300°C/4 hrs (× 200)
- Figure 5.19 Ti-2.5wt%TiC sintered for 1300°C/4 hrs (× 3,000)  
Neck formation between particles of Ti
- Figure 5.20 The pore coarsening effect
- Figure 5.21 Ti-10wt%TiC sintered for 1600°C/0.5 hour (× 650)
- Figure 5.22 (a) TiC particle size vs temperature  
(b) Pore diameter vs temperature
- Figure 5.23 Ti-TiC phase diagram
- Figure 5.24 10wt% TiC/1440°C/4 hours showing the position of point source for microprobe analysis in Table 5.6
- Figure 5.25 X-ray mapping of Ti-10wt%TiC, 1440°C, 2 hours, 10kV (× 600)
- Figure 5.26 X-ray mapping of Ti-10wt%TiC, 1440°C, 2 hours, 10kV (× 3,000)
- Figure 5.27 Carbon diffusion profile
- Figure 5.28 Microhardness vs C/Ti ratio
- Figure 5.29 Ti-TiC phase diagram

## LIST OF TABLES

Table 2.1	Properties of ceramic reinforcements
Table 2.2	Structure and lattice parameter of Ti and TiC
Table 2.3	Some properties of elemented Ti
Table 2.4	Some properties of the TiC element
Table 4.1	Chemical composition of Ti powder
Table 4.2	Chemical composition of TiC powder
Table 4.3	The calculated density of the composites for each TiC content
Table 5.1	(a) Ti and (b) TiC particle size distribution data
Table 5.2	Particle size for different cumulative percent
Table 5.3	Densities and relative green densities for each TiC content
Table 5.4	Image analysis results for Ti-5wt%TiC composites
Table 5.5	Particle size and pore sizes results for Ti-5wt%TiC composites
Table 5.6	EPMA analysis of Ti content
Table 5.7	Atomic ratio C/Ti from EPMA and calculated from equation 5.4

## NOMENCLATURE

$d$	crystalline interplanar spacing
$D$	diameter
$D$	diffusion coefficient
$D_m$	dry mass
$\eta$	viscosity
$dG$	Gibb's free energy
$\gamma$	surface tension
$K_i$	constant
$L_0$	distance between two particle centers
$M$	saturated mass
$\mu$	chemical potential
$dn$	number of moles
$N$	Avogadro's number
$\Omega$	atomic volume
$\Omega_m$	molar volume
$P$	pressure
$Q$	activation energy
$R$	universal gas constant
$R_i$	spherical particle diameter
$RD$	relative density
$\rho$	density
$S$	mass while suspended in water
$dS$	elementary surface
$T$	temperature
$\theta$	contact angle
$V_B$	bulk volume
$dV$	elementary volume
$X$	neck radius

# Chapter 1

## Introduction

### 1.1 HISTORICAL BACKGROUND

Long before furnaces that could approach the melting point of metals were developed, powder metallurgy (P/M) principles were used. In about 3000 B.C. the Egyptians used "sponge iron" for making tools. Powder metallurgy practices were used by the Incas and their predecessors in consolidating platinum (Pt) before Columbus made his first voyage.

The first real commercial application of powder metallurgy occurred when carbon (C) (1878-1898), osmium (Os) (1898-1900), zirconium (Zr), vanadium (V), tantalum (Ta) (1903-1911), and tungsten (W) (Coolidge process), and later molybdenum (Mo), were used for incandescent lamp filaments. Following these developments, the need for a harder material to withstand greater wear became urgent and processes for cemented carbides were perfected in the 1920's.

The next major development in P/M was the production of composite metals used for heavy-duty contacts, electrodes, counterweights and radium containers. All of these composites contain refractory metal particles and a cementing phase with a lower melting point, e.g. copper (Cu) alloys and silver are frequently used, and to a lesser extent cobalt (Co), iron (Fe) and nickel (Ni)<sup>1</sup>.

In addition, another important area of powder metallurgy in the early 1900's was that of porous metal bearings (usually made of Cu, tin (Sn) and graphite) with special types referred to as self-lubricating<sup>1</sup>.

The advent of mass production in the automotive industry made possible the use of iron and copper powders in large tonnages and spawned many of the technological advances of the modern P/M industry. Since the end of World War II, with the advent of aerospace and nuclear technologies, developments have been widespread with regard to the powder metallurgy of refractory and reactive metals such as W, Mo, niobium (Nb), titanium (Ti), and Ta and of nuclear metals such as beryllium (Be), uranium (U), Zr, and thorium (Th).

The 1950's and 1960's witnessed the emergence of P/M wrought products. Hot isostatically pressed superalloys, P/M forgings, P/M tool steels, roll compact strip, and dispersion strengthened copper are all examples.

The late 1970's and 80's witnessed a significant metallurgical breakthrough in the recognition of P/M techniques for eliminating segregation and ensuring a fully homogeneous, fine-grained, pore-free and high-alloy structure. The 1980's also saw commercialization of ultra-rapid solidification and injection moulding technologies.

## 1.2 METAL-MATRIX COMPOSITES

Metal-matrix composites (MMCs) represent a new materials group and, as such, provide potential solutions to design problems such as requirements for stiffness, reduced weight, or strength at elevated temperatures. Many forming, machining and assembly techniques of MMC components have proven to be effective. MMCs consist of a "light" metallic alloy - typically Al, Mg or Ti - which contains reinforcement additives in the form of particles, whiskers, wires or filaments<sup>2</sup>. The incorporation of a second phase aims at improving a desired mechanical or physical property.

MMCs properties are dictated by the type of metallic alloy used as a matrix, the nature of the reinforcement used and the interaction of the two. Reinforcements may be made from a variety of high-performance metallic, ceramic or organic materials such as boron or graphite.

A driving force for the existence of such composites is their capability to be designed to provide a specific type of material behaviour referred to as tailorability<sup>3</sup>. Not only stiffness and strength have received careful attention as

tailorable properties, but also a wider range of operating temperatures or a lower creep rate; and, in more recent years, controlled coefficient of thermal expansion, thermal conductivity, dimensional stability, and abrasive characteristics. Now, according to the type of composite which is considered, MMCs can be made highly directional or virtually isotropic. Tailoring is primarily achieved by selecting the reinforcement (type, shape, size, and concentration) and the matrix metal.

There is little information available on the sintering of Ti-TiC composites over a wide range of temperatures and TiC contents. The objective of this work was to study the sintering behaviour of Ti matrix composites with various amounts of titanium carbide (TiC) particulate reinforcement and to evaluate the optimum experimental parameters for potential composite fabrication.

A literature review is first presented in Chapter 2 in order to clarify the context, define the complex world of composites, and review the work that has been done to date. Chapter 3 will outline the objectives and Chapter 4 will describe the experimental methods used. Then, Chapter 5 presents the results of this study which are assessed and discussed. Finally, overall conclusions are drawn in Chapter 6.

### 1.3 APPLICATIONS

Applications are as diverse as the types of MMCs and a tremendous number of prototypes have been fabricated for applications ranging from tennis racquets to spacecraft parts. The most notable production applications to date are the space shuttle struts (Al reinforced with B fibers), NASA space telescope waveguides, and diesel engine pistons made by Toyota (Al locally reinforced with ceramic fibers) and Mitsubishi (Al reinforced with SiC whiskers). The use of MMCs in automotive pistons is very significant in that this class of materials are being fabricated on a very large scale (350,000 pistons/year by Toyota). They are reliable while functioning in a severe environment and still competitive in the cost-sensitive world automotive market. Other components such as connecting rods are under development (e.g. Renault, France). Indeed there is currently a very significant growth in the use of a wide variety of P/M components in the North American car industry. Numerous other programs are under way to apply MMCs to Army, Navy,

and Air Force structural components. Below (Figure 1.1), an array of powder metal (P/M) components of various configurations demonstrates the economical manufacturing technology in commercial, industrial, and aerospace applications. This economically advantageous process is applicable to most metals and their alloys including Ti, steel, Al, Ni, Ta, Nb, Mo, and Pt.

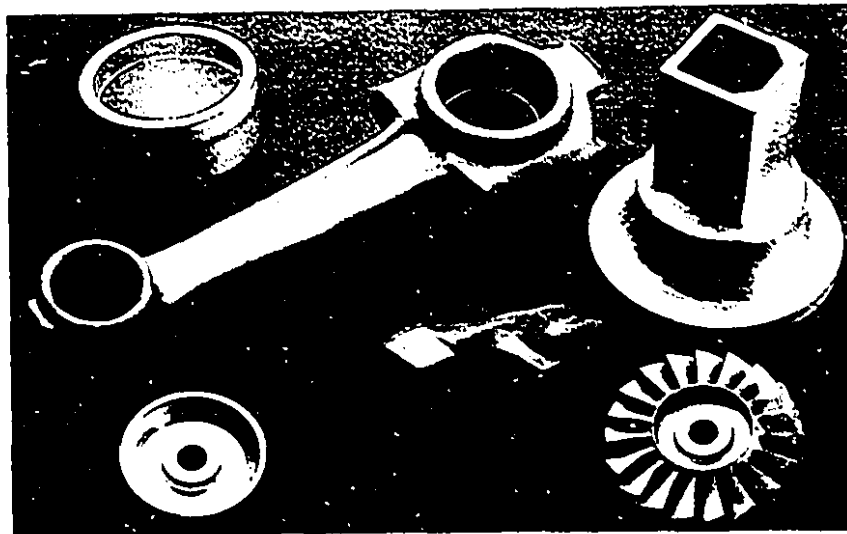


Figure 1.1 - Various P/M components<sup>1</sup>

Although the unique physical and mechanical properties of MMCs are beginning to be understood, many combinations of MMCs remain to be exploited. Several combinations of matrices and reinforcements have been tried since work on metal matrix composites began in the late 1950s. Whatever the future reserves for materials science, the unique features of MMC materials promise to allow for many performance breakthroughs and other spectacular systems will undoubtedly emerge.

---

<sup>1</sup> Courtesy of Dynamet Technology Inc.

# Chapter 2

## Literature review

### 2.1 DEFINITION OF METAL MATRIX COMPOSITES

Besides dispersion-strengthened composites, Metal Matrix Composites (MMCs) are divided in two groups which are continuous fiber (large length-to-diameter ratio) or wires (e.g. Nb-Ti and Nb-Sn wires reinforced Copper matrix or W, Be, Ti, and Mo reinforced superalloy matrices) and discontinuous fiber reinforced composites. Discontinuously reinforced composites encompass short fibers, whiskers and particulates (PMMCs). By comparison to continuous fiber-reinforced composites, discontinuously reinforced composites can be fabricated using near-standard metal-working practices and have more isotropic properties. With the exception of wires, which are metals, reinforcements generally are ceramics.

In order not to confuse the reader regarding these types of composites, a definition of each is required<sup>4</sup> :

- dispersion-strengthening : this composite is characterized by a microstructure consisting of an elemental matrix within which fine particles are uniformly dispersed. The particle diameter ranges from about 0.01 to 0.1  $\mu\text{m}$  and the volume fraction of particles from 1 to 15%.
- fiber (including whiskers) reinforced : the fiber spans the entire size range from 0.1 to 250  $\mu\text{m}$  in length with a volume fraction of a few percent to greater than 70%. Whiskers have a more distinct l/d ratio and are single crystals.
- particulate reinforced : these are characterized by dispersed particles of greater than 1.0  $\mu\text{m}$  in diameter with a volume fraction of 5 to 40%.

In recent years Particulate Metal Matrix Composites (PMMCs) have been of major interest due to their ease of formability which results in reproducible microstructures and properties<sup>5</sup> at modest cost.

## 2.2 MATRIX MATERIALS

Historically, selection of matrix materials has been empirically based, using readily available alloys with little regard to how the matrix may influence the - ultimate mechanical performance of the composite system.

While the selection of matrix composition may be relatively unimportant for unidirectional continuously reinforced MMCs, the same is not true when particulate/whisker-reinforced composites are considered. It has been recently recognized that introducing a reinforcement into a metal matrix produces a new material which may not be expected to respond to processing in a manner similar to its unreinforced counterpart. For example, SiC particulate reinforcement may alter an alloy's aging response.

Al matrix alloys are still the most widely available, the trend to use PMMCs for increasingly elevated temperature applications necessitates the presence of thermodynamically stable dispersoids. This requirement has been achieved by using systems in which elemental solubility, solid state diffusion and interfacial energies are minimized (cf. 2.5), thereby limiting coarsening and interfacial reactions<sup>6</sup>.

Several studies have shown that low matrix alloying additions result in better combinations of strength, ductility and toughness. The pressing need for high temperature, low density materials for advanced airplane structural and engine components has triggered a trend towards exploring intermetallic compounds as matrices<sup>1</sup>. The goal is to develop materials with the service temperature capability of superalloys and the strength-to-density ratio of Ti. Intermetallic Matrix Composites (IMCs) potentially can meet this goal. IMCs typically have matrices based on aluminide or silicide intermetallic systems. Such systems are now being fabricated in the laboratory, based primarily on aluminide matrices (e.g.  $Ti_3Al$ ,  $TiAl$ ,

FeAl, NiAl). For example, Ti additions to Al are attractive because they promote the precipitation of the  $Al_3Ti$  phase. This phase enhances the thermal stability and structural efficiency of the matrix as a result of a high melting point (1330°C), low density (3.3 g/cm<sup>3</sup>) and low diffusivity in Al<sup>7,8</sup>.

Some other minor elements such as Mn and Cr used in wrought alloys as grain refiners have been acknowledged as quite unnecessary in PMMCs<sup>9</sup>. Furthermore, sometimes they can result in the formation of coarse intermetallic compounds during consolidation and subsequent processing, these additions impair the tensile ductility of the composite.

Most of the conventional Al, Mg, Ti, Cu, Ni, or Fe metals have been successfully employed as matrices while research has turned to the use of more ordered alloys (intermetallic compounds) for high temperature applications.

In the 1990s, the tendency will be to minimize quench rate sensitivity in aluminum MMC systems by incorporating, for example, Zr<sup>10</sup>. Also, Al-Li alloys will be evaluated as matrix material because they offer the possibility of achieving a higher specific modulus at lower reinforcement contents. Moreover, specific Ti and Mg base alloys<sup>10</sup> that minimize reinforcement/matrix reactivity, will extend the MMC research field. Mg, with a density two-third that of Al (2.7 g/cm<sup>3</sup>), is also an ideal candidate for weight-critical applications. Thus, reinforced Mg MMCs are currently being considered for satellite structural elements.

### 2.3 PHYSICAL AND MECHANICAL PROPERTIES OF PMMCs

PMMC's offer significant opportunities for developing structural materials possessing combinations of physical and mechanical properties which are not achievable with monolithic alloys. The wide selection of matrices and reinforcements permits the development of MMCs with low density, matching coefficient of thermal expansion (CTE), an increase in elastic modulus and thermal conductivity (TC).

Although PMMCs exhibit attractive mechanical properties, such as high tensile

strength, creep and fatigue resistance, less than optimum ductility and fracture behaviour have limited their widespread usage.

Low density MMCs require the selection of matrices using low density alloys such as those based on Al ( $2.70 \text{ g/cm}^3$ ), Mg ( $1.74 \text{ g/cm}^3$ ), and even Ti ( $4.51 \text{ g/cm}^3$ ). However, when MMCs with optimal strength-density ratio and thermal stability are required, Ni ( $8.90 \text{ g/cm}^3$ ) and Ti base alloys are preferred.

Whereas most metallic matrices exhibit reasonably high thermal conductivity (TC), their CTEs are substantially higher than of most of the reinforcements available (Table 2.1 in section 2.4). Since a number of reinforcements (especially carbides) exhibit very low CTEs ( $3\text{-}10 \times 10^{-6} \text{ K}^{-1}$ ), these enable PMMCs to achieve quite low CTEs. The prediction of the properties of MMCs from the properties of the individual components has been formulated using different mathematical models of which the rule-of-mixture (ROM) is the simplest and generally gives higher values compare to other models. The ROM is expressed as follows :

$$\alpha_c = \alpha_m V_m + \alpha_r V_r \quad 21$$

where  $\alpha$  is a property,  $V$  the volume fraction and the subscripts c, m, and r refer to the composite, matrix, and reinforcement respectively.

Considering the effects of isostatic stress and of thermal barriers at the interfaces, Turner's model<sup>11,12</sup> proposed the following for the calculation of CTE:

$$CTE_c = \frac{(CTE_m V_m K_m + CTE_r V_r K_r)}{(V_m K_m + V_r K_r)} \quad 22$$

where  $K$  is the bulk modulus of the phase.

Hashin and Shtrikman<sup>13</sup> proposed a model for the elastic modulus :

$$E_c = E_m \times \frac{E_m V_r + E_r (V_m + 1)}{E_r V_m + E_m (V_r + 1)} \quad 23$$

where  $E$  is Young's modulus. All these models have been recognized to be in good agreement with experimental values.

There are numerous complex and interrelated factors influencing the yield (YS) and tensile (TS) strength of PMMCs.

Although increasing the volume fraction of reinforcements increases the strength of the MMCs, there is a threshold beyond which the strength decreases (e.g. 30 to 40 vol% SiC in Al-SiC system).

It has been found that the yield stress is higher in compression than in tension, also, although the average residual stress in the MMCs is relatively small, there can be relatively substantial compressive stresses at the matrix-reinforcement interface. Finally, in the matrix region between the reinforcement, the residual stress will be tensile and plastic deformation is likely to initiate at this point since fewer dislocations exist when compared to the reinforcement-matrix interface.

Regarding deformation and fracture mechanisms in PMMCs, our knowledge is still limited. The critical factors affecting the dependence of fracture toughness and the size and distribution of strengthening phases have yet to be established.

## 2.4 REINFORCEMENT SELECTION

Selection criteria for the ceramic particulate reinforcement include :

1. elastic modulus
2. tensile strength (TS)
3. density
4. melting temperature
5. thermal stability
6. coefficient of thermal expansion (CTE)
7. size and shape
8. compatibility with matrix material
9. cost

Some selected properties of commonly used ceramic reinforcements are shown in Table 2.1<sup>10,12,14,15</sup>.

The structural efficiency of discontinuously reinforced MMCs is a function of the density, elastic modulus and tensile strength of the reinforcing phases. The chemical stability and compatibility of the reinforcements with the matrix material are important for both material fabrication and end application.

Table 2.1 - Properties of ceramic reinforcements

Ceramic	Density (g/cm <sup>3</sup> )	Expansivity (10 <sup>-6</sup> /°C)	Strength (MPa)	Elastic modulus (GPa)
Al <sub>2</sub> O <sub>3</sub>	3.98	7.92	221 (1090°C)	379 (1090°C)
AlN	3.26	4.84	2069 (24°C)	310 (1090°C)
BeO	3.01	7.38	24 (1090°C)	190 (1090°C)
B <sub>4</sub> C	2.52	6.08	2759 (24°C)	448 (24°C)
C	2.18	-1.44	-	690
CeO <sub>2</sub>	7.13	12.42	589 (24°C)	185 (24°C)
HfC	12.20	6.66	-	317 (24°C)
MgO	3.58	11.61	41 (1090°C)	317 (1090°C)
MoSi <sub>2</sub>	6.31	8.91	276 (1090°C)	276 (1260°C)
Mo <sub>2</sub> C	8.90	5.81	-	228 (24°C)
NbC	7.60	6.84	-	338 (24°C)
Si	2.33	3.06	-	112
SiC	3.21	5.40	-	324 (1090°C)
Si <sub>3</sub> N <sub>4</sub>	3.18	3.50	-	207
SiO <sub>2</sub>	2.66	<1.08	-	73
TaC	13.90	6.46	-	366 (24°C)
TaSi <sub>2</sub>	-	10.80	-	338 (1260°C)
ThO <sub>2</sub>	9.86	9.54	193 (1090°C)	200 (1090°C)
TiB <sub>2</sub>	4.50	8.28	-	414 (1090°C)
TiC	4.93	7.60	55 (1090°C)	269 (24°C)
UO <sub>2</sub>	10.96	9.54	-	172 (1090°C)
VC	5.77	7.16	-	434 (24°C)
WC	15.63	5.09	-	669 (24°C)
WSi <sub>2</sub>	9.40	9.00	-	248 (1090°C)
ZrB <sub>2</sub>	6.09	8.28	-	503 (24°C)
ZrC	6.73	6.66	90 (1090°C)	359 (24°C)
ZrO <sub>2</sub>	5.89	12.01	83 (1090°C)	132 (1090°C)

The thermal mismatch strain,  $\epsilon$ , between reinforcement and matrix is an essential consideration for composites that will be exposed to thermal cycling.  $\epsilon$  is a function of the difference between the CTE of the reinforcement and matrix,  $\Delta\alpha$ , according to the following expression :

$$\epsilon = \Delta\alpha \times \Delta T \quad 24$$

where  $\Delta T$  is the temperature change. Hence it is clear that  $\Delta\alpha$  has to be minimum in order to minimize strain accumulation. It is also important to recognize that relaxation of these strains, by the formation of a dislocation network, will alter the response of the PMMC to thermomechanical processing relative to that of unreinforced alloys<sup>10,16</sup>. To date, SiC, Al<sub>2</sub>O<sub>3</sub>, B<sub>4</sub>C and TiB<sub>2</sub> particulates have provided the best characteristics for PMMCs.

## 2.5 MATRIX-CERAMIC INTERFACES

The interface formed between the matrix and the ceramic reinforcement is of major interest since its characteristics determine load transfer and crack resistance of the PMMCs during deformation. It is recognized that trustworthy MMCs require a good bond between the particle (or the fiber) and matrix to allow for load transfer, which is one of the dominant strengthening mechanisms in composites. It is now known that in order to maximize interfacial bond strength, it is necessary to promote wetting, to control chemical interactions and to minimize oxide formation. The interaction may be in the form of mechanical locking or chemical bonding between the matrix and the reinforcement.

In fact, three types of metal/ceramic composite interfaces exist : the first is when the two materials do not react (very unlikely), forming only a mechanical bond characterized by interlocking as a result of residual stresses created from the thermal expansion coefficient mismatch; the second is when one material is adsorbed onto the surface of the other, such that they form some primary or

secondary chemical bond; the third is when the two materials react to form a reaction product at the interface.

Ideally, a strong interface results when the two materials form a monoatomic chemical bond, as this will form the strongest bridge between the two materials. This effect will be more pronounced if the two phases have a similar lattice spacings, as in the case of Ti/TiC, thereby optimizing the matching of the chemical bonds. On the other hand, in a composite materials having a brittle matrix, if the bond at the interfaces is too strong, a propagating crack will either stop at the interface or fracture through the reinforcement if it has enough energy. A weaker interface is often more desirable for high toughness purpose, as this will make a propagating crack path longer and more complex, thereby increasing the energy of fracture ( $G_c$ ). If a reaction layer is produced at the interface (generally brittle in metal/ceramic systems) the interface acts as a weak link which in turns causes premature failure by initiation of microcracks and the eventual coalescence of voids.

## 2.6 CURRENTLY AVAILABLE Ti MATRIX COMPOSITES

The Ti matrix composites field has shown high activity since the early 1980s. As mentioned in previously chapters, Ti matrix composites systems may be made from (1) short fibers, (2) continuous fibers or (3) particulates. In the 1970s only two types of composition were under investigation : silicon carbide (SiC) coated boron (B) filaments (Borsic/Ti) and Be/Ti, where beryllium (Be) metal is used either in powder<sup>17</sup> or continuous filament form. However, the toxicity of Be has led to the search for new types of composite materials.

This past decade, many new Ti-based composites have emerged, especially for aircraft applications, because of their excellent specific strength in spite of their temperature limitation<sup>18</sup> compared to the superalloy-based composites. Advanced alloys, such as  $\beta$ 21S, show higher temperature capabilities<sup>19</sup>. However, strength requirements become more crucial as temperatures are increased. By far,

the most extensively explored Ti matrix composite has been the Ti-SiC system. As a matter of fact, SiC-reinforced Ti-based composites have demonstrated dramatic improvements in maximum temperature capabilities in regimes where previously Ni-based alloys were used<sup>20</sup> with double density. Many aerospace applications have already been identified<sup>21</sup>, such as integral compressor rings and structural rods and several more are envisioned for the aircraft skin, internal structures, and cool engine parts<sup>22</sup> of the National Aerospace Plane (NASP).

The prime concern limiting the higher temperature use of Ti-based composites is environmental resistance, both from oxygen embrittlement and from a surface oxidation standpoint. Other concerns for SiC-reinforced titanium-based composites<sup>23,24,25</sup> are that the fiber reacts with the matrix during processing (resulting in brittle zones around the fibers), as well as the large CTE mismatch between the fiber and matrix. Concerning the use of Al<sub>2</sub>O<sub>3</sub> fibers, they are chemically incompatible with Ti alloys and therefore, are not considered as potential reinforcing fibers. A new type of Ti-based composite (Ti-TiC system) currently being investigated at McGill University, shows new and interesting properties and is the subject of this thesis.

Although Ti-based composites still have many obstacles to overcome in order to become competitive in the commercial aerospace market, an extensive effort is underway into improving their properties through new alloying, external coatings, fiber coatings and these composite materials are likely to result in near-term payoffs.

## 2.7 Ti-TiC CHEMISTRY AND CRYSTALLOGRAPHY

### 2.7.1 The Ti-TiC phase diagram

Two phase diagrams are shown in Figure 2.1 (a)<sup>26</sup> 2.1 (b)<sup>27</sup>. In fact, the Ti-C phase consists of one cubic compound having the general formula TiC. Because of the great affinity of this system for oxygen and nitrogen and the marked influence these impurities have on the various physical and chemical properties, the

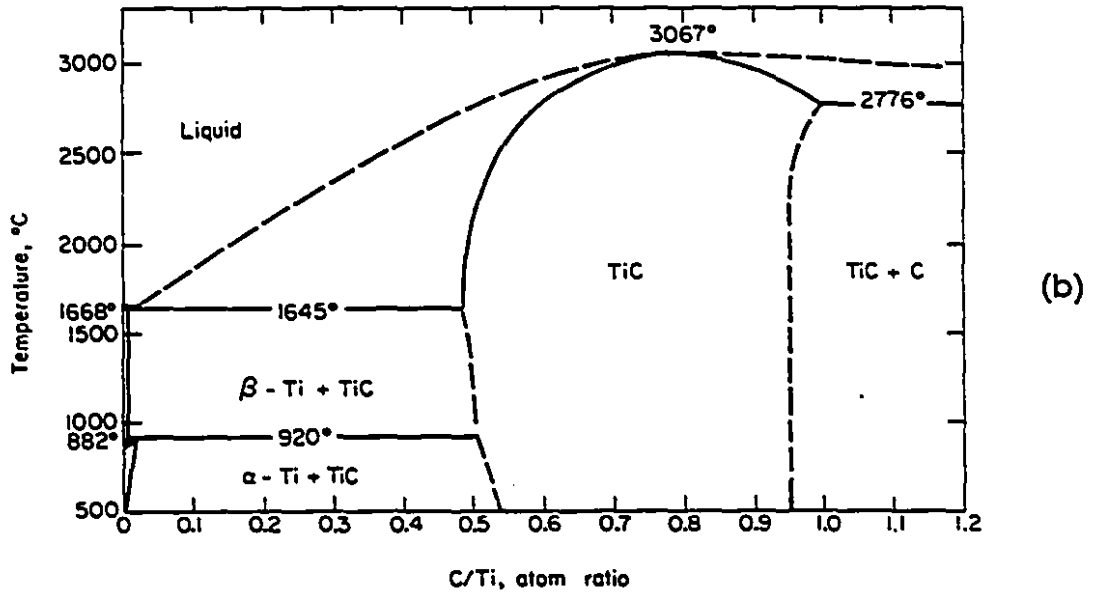
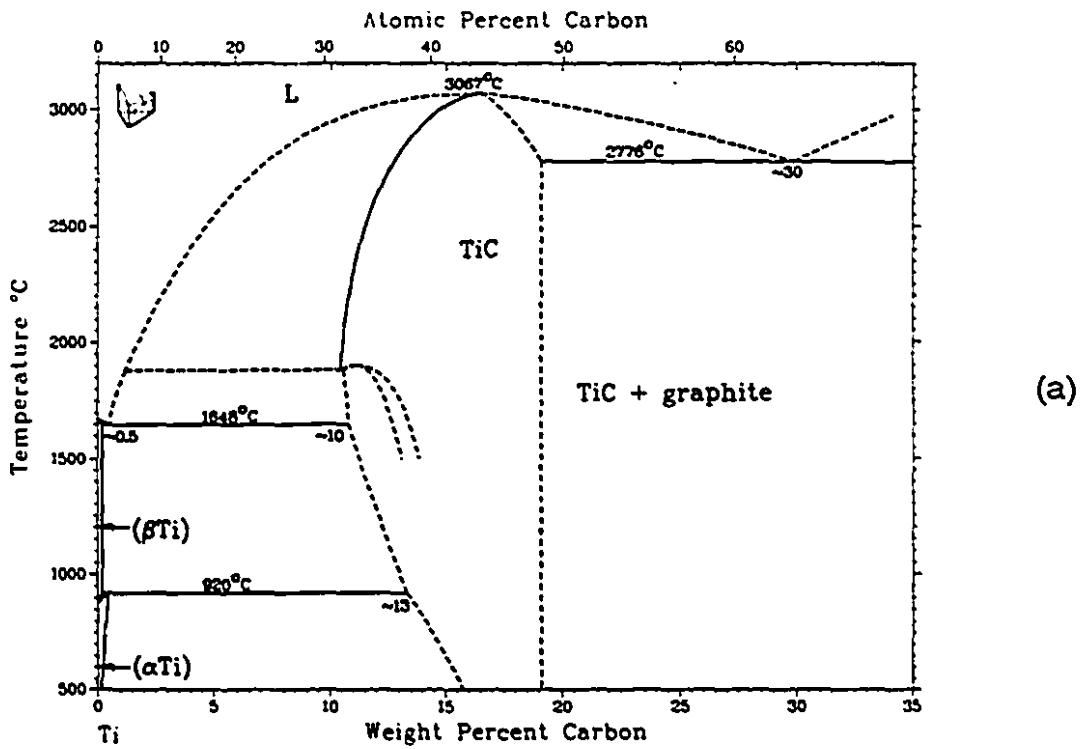


Figure 2.1 - Phase diagrams of the Ti-TiC system as a function of (a) weight percent C and (b) atomic ratio C/Ti

accuracy of most measurements is not perfect. The melting point of pure Ti metal is well established at  $1668^{\circ} \pm 8^{\circ}\text{C}$ , and the  $\alpha$ - $\beta$  transition at  $882.2^{\circ} \pm 0.5^{\circ}\text{C}$ . Both temperatures are raised by the dissolution of oxygen, thus accounting for the various higher values.

The addition of carbon lowers the melting point to a eutectic at  $1645^{\circ} \pm 5^{\circ}\text{C}$  and the  $\alpha$ - $\beta$  transition is raised to a peritectoid near  $920^{\circ}\text{C}$ <sup>28,29</sup>. TiC has an extraordinarily wide composition range and the usual notation for the non-stoichiometric TiC is  $\text{TiC}_x$  with  $x \leq 1$ . A non-stoichiometric ceramic is one that has a deficiency of one type of atoms. The structure is a TiC structure with vacancies to make up for the missing carbon atoms. Nonstoichiometric materials have different diffusion characteristics than their stoichiometric equivalent. TiC compound exists in a wide composition ranging from 11.14wt (33 at)%C to 20.05wt (50 at)%C.  $\text{Ti}_2\text{C}$  was estimated to be stable up to about  $1900^{\circ}\text{C}$ <sup>26</sup>. Lattice-parameter measurements<sup>30</sup> indicated a rather high solubility (about 2.0wt (7.5 at)%C) of C in  $\alpha$ -Ti. However, this was not confirmed by others<sup>36,37,31</sup>. The maximum solid solubility of C in  $\alpha$ -Ti reported<sup>36</sup> is 0.5wt (2.0 at)%C at the peritectoid temperature of  $920^{\circ}\text{C}$  (Figure 2.1 (a)). It is about 0.27wt (1.1 at)%C at  $800^{\circ}\text{C}$  and 0.12wt (0.45 at)%C at  $600^{\circ}\text{C}$ <sup>37</sup>. The solubility of C in  $\beta$ -Ti was found to be about 0.15wt (0.6 at)%C at  $920^{\circ}\text{C}$ , about 0.27wt (1.1 at)%C at  $1400^{\circ}\text{C}$ , and about 0.8wt (3.1 at)%C at  $1750^{\circ}\text{C}$ .

At the Ti-TiC eutectic temperature the composition lies between  $\text{TiC}_{0.47}$  and  $\text{TiC}_{0.49}$ <sup>37</sup>. Lower values were found to be caused by oxygen contamination. Norton and Lewis (1963) gives  $\text{TiC}_{0.95}$  as the upper-phase boundary at  $1950^{\circ}\text{C}$ . Between these composition limits the melting point of the phase rises from  $1645^{\circ}\text{C}$  to a maximum of  $3067^{\circ} \pm 15^{\circ}\text{C}$  near  $\text{TiC}_{0.80}$  and then drops to the TiC + C eutectic at  $2776^{\circ} \pm 6^{\circ}\text{C}$ <sup>32</sup>.

### 2.7.2 Structure of Ti and TiC

The lattice parameters of Ti and TiC are shown in Table 2.2<sup>32</sup>. Values are given for the quenched-in phase boundary composition at room temperature.

Table 2.2 - Structure and lattice parameter of Ti and TiC

Phases in equilibrium	Composition of first phase	Structure type	Lattice parameter (Å)	Investigator
$\alpha$ -Ti	Pure	HCP (A3)	a = 2.95111 c = 4.68433	Wood (1962)
$\beta$ -Ti	Pure at 25°C (from quenched alloys)	BCC (A2)	a = 3.287	Donohue (1963)
$\alpha$ -Ti + TiC	$\alpha$ -TiC <sub>0.016</sub>	HCP (A3)	a = 2.9550 c = 4.7025	Cadoff and Nielsen (1953)
TiC + $\alpha$ -Ti	TiC <sub>0.47</sub> (quenched from 1650°C)	FCC (B1)	a = 4.285	Rudy <i>et al.</i> (1965a)
TiC	TiC <sub>0.86</sub> (maximum)	FCC (B1)	a = 4.3305	Norton and Lewis (1963)
TiC + C	TiC <sub>1.0</sub>	FCC (B1)	a = 4.3280	-

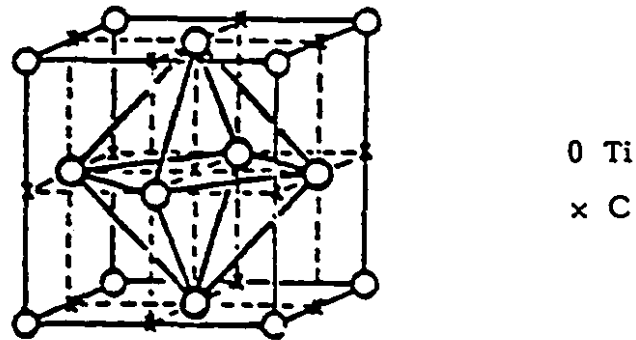


Figure 2.2 - B1 structure of TiC

$\alpha$ -Ti is Hexagonal Close Packed under the  $\alpha$ - $\beta$  transition temperature of 882°C, and  $\beta$ -Ti is Body Centred Cubic above this temperature.

Most transition metal carbides and nitrides, including TiC, TiN, NbC, VC, and VN have the B1 structure (face centred cubic). The B1 (NaCl) structure is built up by filling the octahedral sites in the fcc substructure formed by the metal atoms

with nonmetal atoms (Figure 2.2).

Its stacking sequence can be represented as AXBX'CX''/ AXBX'CX'', where A, B and C are the usual designations for the fcc-close-packed metal-atom layers, X represents a complete or partial filling of the first interstitial site layer, and X' and X'' differ from the X layer by a lateral shift<sup>33</sup>.

## 2.8 Ti AND TiC POWDER PRODUCTION

### 2.8.1 Production of Ti Powder

Titanium is the design choice for many aerospace as well as non-aerospace lightweight applications, because of an attractive combination of low density, good mechanical properties, and general corrosion resistance. However, Ti is expensive to produce, fabricate, and machine. Consequently, much effort has been expended to reduce the cost which has led to extensive research in P/M techniques. This part will detail the two basic methods currently used to produce Ti powders.

The production<sup>34</sup> involves the chlorination of natural and synthetically produced rutile TiO<sub>2</sub> in the presence of carbon :



The resultant titanium tetrachloride (TiCl<sub>4</sub>) is purified by distillation and chemical treatments and then reduced to metallic titanium termed "sponge" because of its appearance. Most of the world's production employs Mg metal as the reducing agent, base on a process developed by Kroll :



To ensure complete reaction and to provide coarse sponge particles for sintering, the final reactions are completed at temperatures as high as 1040°C. The bulk of the molten magnesium chloride (MgCl<sub>2</sub>) is then generally tapped off to free additional reactor capacity and to simplify recycling of MgCl<sub>2</sub>.

In 1992, Ti metal sponge metal was produced by three U.S. firms in Nevada,

Ohio and Oregon. An estimated 14,000 tons of metal sponge were consumed in 1992 of which about 75% was used in jet engines, airframes, space and missile applications. The remaining 25% was used in the chemical-processing industry, power generation, marine and ordinance, medical, and other non-aerospace applications. The volume of the sponge metal consumed was about \$115 million, assuming an average selling price of about \$3.75 per pound<sup>35</sup> compare to 53.7 cents/pound for Al).

Reported consumption of Ti sponge increased slightly from 1991. However, demand was much lower than the high levels (25,000 tons) reached in 1989 and 1990. Reductions in consumer inventories, declines in orders for military and commercial aerospace applications and the recession contributed to the second year of weak demand for Ti sponge.

### 2.8.2 Production of TiC powder

Early techniques for the preparation of TiC include its isolation from titanium-bearing cast-iron and the reduction of  $TiO_2$  by carbon. The latter method is used today for the industrial production of the carbide; and because of the technical importance of TiC, the reaction has been studied in some detail. The most common method of preparation is reduction and simultaneous carburization of their oxides. The starting material is pure Rutile ( $TiO_2$ ) (pigment). A mixture of 68.5%  $TiO_2$  and 31.5% C black is prepared by wet or dry milling. Carburization is carried out in very dry, nitrogen-free hydrogen, and in its own protective gas (CO within a sealed furnace system) or in vacuum, at temperatures above  $1800^\circ C$ <sup>36</sup>.

The oxide reduction starts at  $935^\circ C$  and between  $1,000^\circ C$  and  $1,500^\circ C$  it proceeds through the following stages :



This reaction is complete only when the free-C content of the product is below 0.8%<sup>37</sup>. High-quality powder has only 0.1 to 0.2% free C and a minimum of 80.0% Ti. The final product is, in fact, better represented by the formula  $TiC_xO_y$ . At

1200°C with a 10° per minute temperature rise, C-deficient TiC and/or Ti are produced. Higher temperatures and heating rates favour the formation of a more C-rich product. The presence of CO is said to favour the formation of the carbide, with a higher temperature needed if the CO pressure is too low. Meerson and Krein (1952) conclude that a carbide closest to the 1:1 ratio is obtained under 1-10 torr of CO at 1600°C-1700°C.

Other techniques include the reaction of  $\text{TiS}_2$  and C at 2000°C or the reaction of  $\text{TiH}_4$  and C in vacuum at 900°C. The carbide has also been prepared by heating a tungsten (W) wire in an atmosphere of  $\text{TiCl}_4$ ,  $\text{H}_2$ , and a hydrocarbon vapour or the same process but using a carbon filament. Finally other preparations involved the use of  $\text{CaC}_2$ ,  $\text{TiCl}_4$ , and  $\text{H}_2$  as starting materials.

Although a few percent oxygen may be satisfactory from a commercial standpoint, attempts to obtain a pure TiC material have been unsuccessful. The last trace of oxygen is extremely difficult to remove and results in a large disparity as far as the physical properties are concerned. Moreover, even if an almost pure carbide is obtained, subsequent heating can rapidly contaminate the sample unless a very good vacuum is used<sup>38</sup>.

## 2.9 Ti-TiC COMPOSITES

### 2.9.1 General background

High specific strength, specific modulus and elevated-temperature properties of titanium and its alloys have made them ideal candidate matrices for developing high-performance metal-matrix composites for use in aerospace applications.

Table 2.3 presents some physical and mechanical properties of the element Ti. Ti is the fourth most abundant metal on the earth's crust. Rutile ( $\text{TiO}_2$ ) and ilmenite ( $\text{FeTiO}_3$ ) are the primary ores. Ti is very reactive with carbon, oxygen and iron. It is a paramagnetic material and has a very low thermal conductivity compared to Al(2.37) or Cu(4.0). The Ti radius is almost twice that of carbon (0.77 Å). At temperatures higher than 600°C, Ti tends to form oxides ( $\text{TiO}_2$ ), halides

Table 2.3 - Some properties of elemented Ti

electrons	covalent radius	density $\alpha$ -phase	density $\beta$ -phase	melting Temp.	boiling Temp.
22	1.32 Å	4.51 g/cm <sup>3</sup>	4.35 g/cm <sup>3</sup>	1668°C	3260°C

M <sup>1</sup>	CTE <sup>2</sup>	E <sup>3</sup>	thermal conductivity	yield strength	tensile strength
47.9 g/mol	8.5.10 <sup>-6</sup>	100-110 GPa	0.22	482 MPa	724 MPa

(TiCl<sub>4</sub>, TiF<sub>6</sub>), carbides (TiC) and nitrides (TiN) interstitials. Ti is very oxidizable, and its corrosion resistance is much higher than that of stainless steel, since TiO<sub>2</sub> acts as a passivation film.

Ti is very sensitive to impurities in solid solutions, which are bad for toughness and ductility because of being "alpha-genes". Ti tends to form the non stoichiometric compound TiH<sub>x</sub> (x<2) by absorption of H<sub>2</sub>.

Its density is between that of steel and Al and explains its wide use in Aerospace and cryogenic industries. Also, this element has a good fatigue strength and a good impact strength (even at low temperatures).

Early work on Ti-matrix composites has shown that extensive interfacial reactions can occur between typical reinforcements (e.g. B or SiC fibers) and the Ti matrix, which has a detrimental effect on the overall composite properties. While attempts have been made to alloy Ti with different elements to obtain a compatible matrix composition<sup>39</sup>, alternative reinforcing phases have also been suggested<sup>40</sup>. Among these, TiC is particularly attractive because it is completely compatible with

---

<sup>1</sup> molar mass

<sup>2</sup> Coefficient of Thermal Expansion

<sup>3</sup> Young's modulus

Ti and its alloys and is stable both during the processing of the composites and in service. In addition, high quality TiC is readily available. Moreover, cold and hot isostatic pressing processes have recently been developed which provide a viable method for the production of TiC particulate-reinforced Ti-6Al-4V composites<sup>41</sup>. The following table (Table 2.4) will present the main physical and mechanical properties of this powder.

Table 2.4 - Some properties of the TiC element

density	melting Temp.	MoR <sup>1</sup>	CTE <sup>2</sup>
4.93 g/cm <sup>3</sup>	3100°C	275-450 MPa	7.8.10 <sup>-6</sup>
E	tensile strength	compressive strength	Knoop hardness
350-420 GPa	240-275 MPa	2800 MPa	1800-2600 <sup>3</sup>

TiC is an intrinsically hard and strong material due to the nature of its covalent bonding. Because of this, it has always been considered for composites designed for tribological applications, such as in *cermets* and, more recently, for light weight and high temperature applications. Therefore, the author will outline what has been discovered so far about the Ti-TiC systems and Ti6Al4V-TiC systems and in terms of sintering behaviour, density, microhardness properties, and C diffusion.

### 2.9.2 Current research on Ti-TiC PMMCs

Since the work of this thesis involves processing Ti and TiC powders at elevated temperatures, it is only fitting that their mechanical and chemical properties are reviewed here. It should be noted that very few investigators have

---

<sup>1</sup> Modulus of Rupture

<sup>2</sup> Coefficient of Thermal Expansion

<sup>3</sup> Kennametal, B.C.

considered this combination, since most choose to look at the more popular Ti-6Al-4V/TiC and Ti-SiC systems. However, sintered Ti-TiC systems have been recently studied to essentially improve the wear resistance of Ti<sup>42,43</sup>.

Many TiC contents have been investigated (from 5 to 50wt%) but the Ti + 10wt%TiC has been more extensively discussed. They are usually sintered in the temperature range 850-1500°C.

It was found that, due to diffusion of C from the TiC into the surrounding Ti matrix, the interaction between the TiC particles and Ti matrix occurs rapidly during sintering. This phenomenon results in particle growth, agglomeration and a decrease in microhardness which in turn was seen to improve the sinterability of the Ti<sup>62</sup>(Figure 2.3 and 2.4). For example relative densities of 96% (4.38 g/cm<sup>3</sup>) were

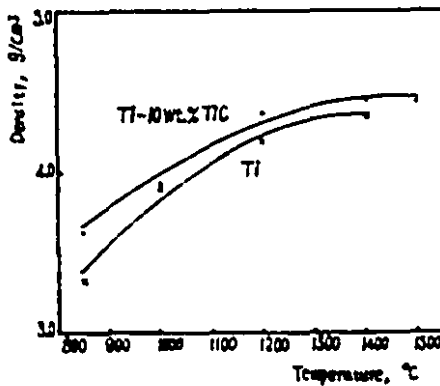


Figure 2.3 - Density of Ti/10%TiC and pure Ti vs temperature

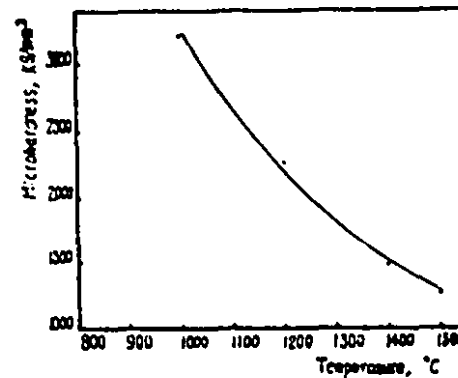


Figure 2.4 - Microhardness of TiC particles Ti/10%TiC PMMC vs temperature

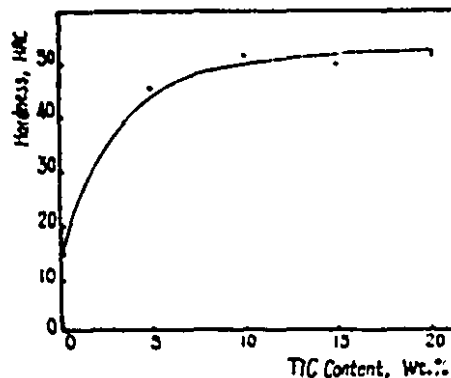


Figure 2.5 - Macrohardness of the Ti-TiC PMMCs vs TiC content

obtained for Ti/TiC10wt%, while only 93% relative density was achieved for pure Ti. For the same specimens, the macrohardness (Figure 2.5) was seen to increase by the addition of TiC particles. The elastic modulus of the Ti/TiC 10wt% also increased from 100 to 135 GPa.

## 2.10 Ti6Al4V-TiC COMPOSITES

Most of the work has been done on 10 and 20vol%TiC particulate-reinforced powder metallurgy of Ti-6Al-4V alloy composite<sup>44,45</sup> (CermetTi-10 and CermetTi-20 respectively). The materials were vacuum sintered at around 1200°C for 1.5 hours. The sintered compacts approached nearly 100% density with the TiC particle size ranging from 5 to 30  $\mu\text{m}$  in diameter after sintering.

The microstructure of Ti6Al4V-10vol%TiC showed excellent bonding between the TiC and the matrix with the formation of only a small reaction zone which appear to be restricted to the volume of TiC particles, themselves.

The main reaction which has been assessed so far results in the generation of non-stoichiometric annuli of TiC surrounding the unchanged stoichiometric TiC cores. The annulus was made visible by the fact that a wall of dislocations was formed which separated the non-stoichiometric TiC from the central stoichiometric core. Authors<sup>64</sup> found 33at.% C for the non-stoichiometric TiC with a standard TiC normalised at 50at.%. In view of the fact that the TiC particles were C-deficient in their outermost layers, it was expected that there would be some evidence of diffusion of C into the alloy or diffusion of Ti into the TiC. However, no evidence for C enrichment of the matrix was detected.

Furthermore, since virtually no dislocations were present in the as-received TiC, it was concluded that the dislocations walls probably consisted of those which relieve the coherency stresses between stoichiometric and non-stoichiometric TiC, as well as other dislocations which remained from the processing.

## 2.11 FUNDAMENTALS OF CONSOLIDATION AND SINTERING

### 2.11.1 Introduction

Consolidation of metal powders generally entails compacting, followed by sintering. However, metal powders sometimes are sintered without compacting, which is called "loose powder sintering"<sup>46</sup>. This process is suitable for bronze filters and porous electrodes, as well as for model experiments.

During sintering, the powder particles bond to a coherent body by atomic transport events at elevated sintering temperatures, in the presence of a suitably controlled atmosphere. The sintering temperature is below the melting point of the single metal powder or the solidus temperature of the homogeneous alloy powder. The use of prealloyed powders, in which each powder particle has the same composition as the final part produced by compacting and sintering, is one method of P/M alloy production (such prealloyed powders typically are produced by atomization). Powder metallurgy alloys also can be produced by blending two or more constituents powders, as the case for Ti-TiC, in proportions required to achieve the desired overall alloy composition. Constituent powders of the mixture may be composed of pure elements (elemental powders) or alloys containing two or more elements (master alloy powders).

Homogenization occurs through interdiffusion of the chemical elements among the constituent powders of different composition and is therefore a solid-state diffusion process<sup>47</sup>. This circumvents some of the disadvantages of prealloyed powder processing. High densities and high green strength can be achieved in the as-compacted condition. Furthermore, adjustments to alloy composition can be made readily by varying the proportions of constituent powders in the mixture, thus eliminating the need for additional powders of different composition.

The simplest form of pressure-assisted sintering is that which occurs by uniaxial hot pressing. The following discusses the changes that take place when metal powder compacts in the as-pressed condition (green compacts), are sintered. These changes

are described phenomenologically and from the point of view of the driving forces and the material transport mechanisms.

### 2.11.2. Driving forces and material transport in sintering

When compacts shrink, changes in interior geometry occur. One of the important occurrences in the early stages of sintering is the increase in the contact area between particles. This may occur without significant changes in the overall density of the compact. Another change is the rounding and spheroidization of the pore structure, which is best observed by metallography. Of course, changes in mechanical properties are a direct consequence of these geometrical changes.

During compaction, powder particles are subjected to strain hardening that increases with pressure. Sintering causes annealing, during which strain hardening is relieved, primarily through recrystallization.

The principal driving forces are capillary forces due to the surface and interfacial tensions, also called specific surface and specific interfacial free energies, of the free surfaces and the interfaces between grains. These forces cause stresses that are related to the curvature of the surfaces and interfaces. These stresses tend to decrease the surface and the interfacial areas and are the principal driving forces in sintering.

The simplest case would be a monocrystalline system, for which the relationship between surface tension ( $\gamma$ ) and equivalent to pressure gradient ( $\Delta P/P_0$ ) is given by Thomson-Freundlich equation (equation (9) Appendix 1):

$$\frac{\Delta P}{P_0} = \frac{\gamma \Omega}{kT} \left( \frac{1}{R_1} + \frac{1}{R_2} \right) \quad 2.8$$

where  $\Omega$  is the atomic volume,  $k$  is Boltzmann's constant,  $T$  is the absolute temperature, and  $R_1$  and  $R_2$  are the principal radii of curvature of the surfaces. Under convex surfaces for which the curvature is negative, the stress is tensile ( $\sigma < 0$ ). For concave surfaces with positive curvature, the stress is compressive. The stress defined by equation 2.8 causes a gradient in chemical potential between

surfaces with different radii of curvature (equation (1) in Appendix 1). The curvature gradient inherent to the initial stage of sintering drives mass flow to the neck. As the neck grows, the curvature gradient is relaxed and the process slows down. The driving force provided by the curvature can be interpreted differently according to the sintering stage. For instance, in the intermediate stage the curvature around the cylindrical pores gives the driving force. But in the final stage, the curvature around the spherical pores gives shrinkage.

In this discussion of the driving forces that cause sintering - or, more specifically, material transport during sintering - compacts are assumed to be sintered without the application of external pressure. If external pressure is applied, the capillary forces are of secondary importance compared to external forces, particularly in metallic systems.

The following paragraph explains the different sintering mechanisms. A sintering mechanism describes the path of atomic motion which produces the mass flow. For metal powders, these mechanisms are usually diffusion processes with surface, grain boundary or lattice paths.

#### Transport mechanisms

There are two classes of transport mechanism : *surface transport* based on a "tangent sphere model" and *bulk transport* based on a "secant sphere model". One has to realize that these models become less and less valid with advancement of sintering. *Surface transport*, as shown in Figure 2.6<sup>48</sup> involves neck growth without densification, i.e. the density remains constant. Surface diffusion and evaporation-condensation (E-C) are the two most important contributors during surface transport controlled sintering<sup>48</sup> and, to a lesser extent, lattice volume diffusion (VD).

In contrast to *surface transport*, in *bulk transport* controlled sintering, the mass originates at the particle interior with deposition at the neck region<sup>67</sup>. Volume diffusion (VD) and grain boundary diffusion (GB) are characteristic of bulk transport mechanisms, while plastic flow (PF), though existing, is of minor importance and

more often considered as a transient process.

One of the early mechanisms postulated is evaporation/condensation. Atoms evaporate from flat surfaces that have a higher vapour pressure and are transported

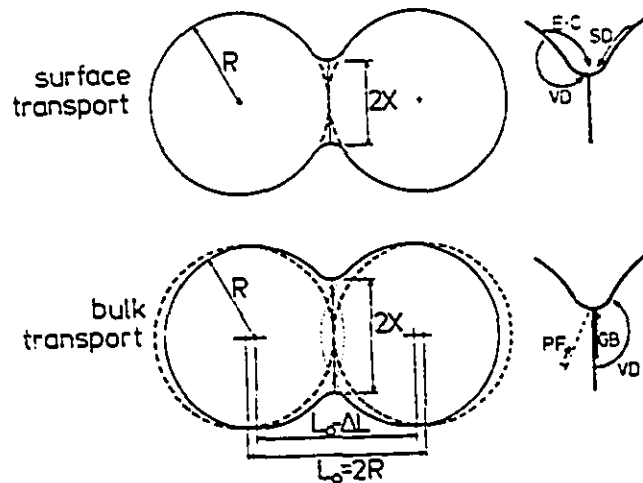


**Figure 2.6 - The two classes of sintering mechanisms as applied to sphere-sphere sintering**

through the gas phase to highly curved convex surfaces that have a lower vapour pressure, where they condense. Because most metals do not have high vapour pressure at temperatures near their melting points, evaporation and condensation contribute nominally to material transport in metallic systems.

Diffusional flow is the most important mechanism of material transport. It is based on the concept that a certain concentration of vacancies exists in the crystal lattice of a metal. This concentration is a function of temperature and may reach values on the order of one vacancy for every 10,000 occupied lattice positions at temperatures near the melting point of the metal. Vacancy concentration also is a function of the chemical potential or stress to which the surface of the metal is subjected. Consequently, a gradient of vacancies exists between a highly curved convex surface, which has a higher vacancy concentration, and an adjacent flat

surface, which has a lower vacancy concentration.

Studies of diffusional flow have concentrated on the first or initial stage of sintering, where the kinetics are dominated by the sharp curvature gradients located at the interparticle neck. At an early stage, the pore structure is open and fully interconnected. During this stage, the small necks between particles become larger. This causes rounding of the pores and some decrease in total pore volume (Figure 2.7<sup>48</sup>).

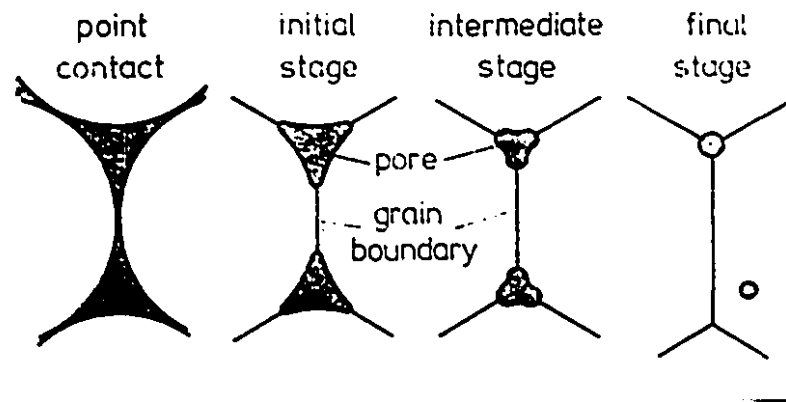


**Figure 2.7 - Interparticle bond development during sintering (pore spheroidization)**

There are two types of diffusional flow possible under the influence of vacancy concentration differences between flat and highly curved surfaces. They are volume (lattice) diffusion, indicated schematically by path VD, and surface diffusion, indicated by path SD in *surface transport mechanism* (Figure 2.6). These two types of diffusional flow cause rounding and spheroidization of irregular pores in a compact. However, they do not explain shrinkage, which would be represented by a decrease in the distance between the centres of the two spherical particles.

To explain shrinkage, flow of atoms from the grain boundary must be considered. This is indicated by path GB, which represents grain boundary diffusion, and path VD, which represents volume diffusion from the interior of the grain boundary to the neck for the *bulk transport mechanism* (Figure 2.6). When atoms flow from the grain boundary to the neck, vacancies flow in the opposite direction

and are thus eliminated at the grain boundaries. This causes the centres of the two particles to approach each other, and shrinkage occurs.

The rates of the diffusion (volume diffusion, surface diffusion, and grain-boundary diffusion) vary greatly, and the geometries that govern transport also vary and are quite complex even for simple model systems, such as sintering of spheres. Rates of material transport during the initial stage of sintering can be calculated for model systems such as the two-sphere model discussed above.

The model for neck growth assuming monosized spheres initially in point contact is represented by a generalized equation<sup>49,50</sup> :

$$\frac{X^p}{R^q} = K_i(T) \cdot t \quad 2.9$$

where  $X$  is the neck radius,  $R$  is the particle radius,  $T$  is the isothermal sintering time, and  $K_i$  is a combination of material and geometric constants. The exponents  $p$  and  $q$  depend upon the mechanism involved. Appendix 2 gives an overview of the different possible laws. Equation 2.9 is generally valid for neck size ratio less than 0.3, i.e.  $X/R < 0.3$ <sup>67</sup>. Above this ratio, there is no more neck growth but simply diffusion between boundaries.

Furthermore, a general shrinkage law can be derived from equation 2.9 :

$$\frac{\Delta L}{L_0} = \left( \frac{K(T)}{2^p \cdot R^{p-q}} \right)^{\frac{2}{p}} \cdot t^{\frac{2}{p}} \quad 2.10$$

where  $\Delta L/L_0$  represents the approach of the centres of the particles (Figure 2.6).

During the intermediate stage of sintering, the original particles are no longer distinguishable, because the pore channels between particles are pinched off and become closed. At this point attention shifts from the interparticle neck growth to the grain-pore structure. The pores form a more or less interconnected continuous network throughout the compact and the pore structure is much smoother. Grain boundaries between the original particles migrate due to grain growth. The driving force is the interfacial energy (both the surface and grain

boundary energy). The predominant development of compact properties occurs in the intermediate stage<sup>48</sup>.

In the third or final stage, they become isolated. Models for these last two stages are complex and are not generally accepted and therefore will not be discussed. Nevertheless, it is well known that the isolation of the pores at grain interiors results in a drastic decrease in the densification rate. Therefore, in the final stage, the kinetics are very slow. The driving force only consists of the elimination of the pore-solid interfacial area.

Clear distinctions do not exist between the sintering stages, but it has been recognized that the relative density of the compact does not exceed 92% at the end of the intermediate stage, i.e. still fully interconnected pores.

### 2.11.3 Homogenization during sintering

Density differences between two different types of particles often cause mixing difficulties. Such problems are minimized by varying the size of the particles used. Sintering causes solid-state diffusion (lattice diffusion) of the solute atoms into the solvent matrix and diffusion of solvent atoms into the solute-rich particles. Homogenization, as a function of time at temperature, may be described in terms of concentration/distance profiles that exhibit discontinuities in the as-compacted condition and that approach the average compact composition as the concentration gradients are eliminated via interdiffusion. Generally, the compact behaves as a collection of many small diffusion couples that are allowed to undergo interdiffusion to the point where atomic fluxes become negligible and homogenization is achieved.

Characteristics of the powder particles exert a significant effect on homogenization kinetics. The sizes of the particles in the mixture establish the distance over which interdiffusion must occur to achieve homogeneity. For multi-phase binary systems, reasonable simplifications have to be made (assumption of single and/or binary phase behaviour) to analyze the homogenization process.

The duration of sintering required to achieve a desired degree of homogeneity is critically dependent on temperature, because diffusion coefficients ( $D$ ) are exponentially dependent on temperature :

where  $D_0$  is the pre-exponential factor;  $Q$  is the activation energy;  $R$  is the

$$D = D_0 e^{-\frac{Q}{RT}}$$

2.11

universal gas constant; and  $T$  is the absolute temperature. Blending and mechanical working also influence homogenization kinetics.

## 2.12 COMMERCIAL PROCESSING, CONSOLIDATION AND SINTERING

The composite fabrication method is an important consideration because it is the fundamental linkage between properties and cost. Also, microstructural features which arise during processing have a significant influence on performance. A major hurdle is the achievement of proper bonding between the two phases in order to attain good load transfer between the two materials. As it has been discussed previously, not all combinations of reinforcement and matrix are inherently compatible, and many cannot be processed into a composite without modification of the interface (e.g. excessive interfacial reactivity which leads to a brittle layer around the reinforcement).

Fabrication methods can be divided into primary and secondary processing methods<sup>51</sup>. Primary methods are used to create the MMC from its constituents, whereas secondary processes are similar to those for monolithic metals, including rolling, extrusion, spinning, forging, creep-forming and machining, even though the latter poses some difficulties because the reinforcements are often very hard.

A variety of processing techniques have evolved over the last two decades in an effort to optimize the structure and properties of PMMCs. The processing methods can be grouped according to the temperature of the metallic matrix during processing and therefore can be classified into three categories<sup>14</sup> :

- \* liquid phase processes
- \* two-phase (solid-liquid) processes
- \* solid state processes

The following section will discuss solid state processes, since it was the process used during this study at McGill University.

The fabrication of PMMCs from blended elemental powders involves a number

of steps prior to final consolidation. Two of the techniques, powder metallurgy and high energy rate processes, are described in this chapter.

### 2.12.1 Composite powder metallurgical techniques

Powder Metallurgy processing is attractive for several reasons. First of all its net shape capability offers the potential for cost savings; secondly, P/M employs lower temperature vis-à-vis casting and should therefore offer better control of interface kinetics; finally the use of special matrix alloy compositions and microstructural refinements are potentially possible via rapidly solidified powder processes.

Solid phase processes invariably involve the blending of rapidly solidified (e.g. atomized) powders with particulates, platelets or whiskers, using a number of steps. These include sieving of powders, blending with the reinforcement phase(s), hot pressing to approximately 75% density, degassing and final consolidation by extrusion, forging, rolling, or some other hot working method.

Consolidation of the PMMC preform is achieved by hot extrusion in the ALCOA process (Fig.2.8<sup>14</sup>), whereas in the CERACON process, final densification is achieved by hot pressing in a pressure transmitting medium (PTM)(Fig.2.9<sup>14</sup>). In this latter process, (1) half of the PTM (621°C) is poured into a preheated die and the preform is placed into the die. (2) The die is then filled completely with the remainder of the heated PTM. (3) A pressure of 1.24 GPa (180 ksi) is applied to consolidate the preform. (4) After pressing, the part is removed and the hot PTM is recycled to the PTM heater.

Powder metallurgy fabrication of composites is a family of techniques with the flexibility to produce unique combinations of matrix alloys and reinforcement materials. The P/M methods have been successfully applied to a large number of metal/ceramic combinations.

In terms of microstructural requirement, the P/M approach is superior in view of the rapid solidification experienced by the powders. This allows the development of novel matrix materials outside the compositional limits dictated by equilibrium thermodynamics<sup>52,53</sup> in conventional solidification processes.

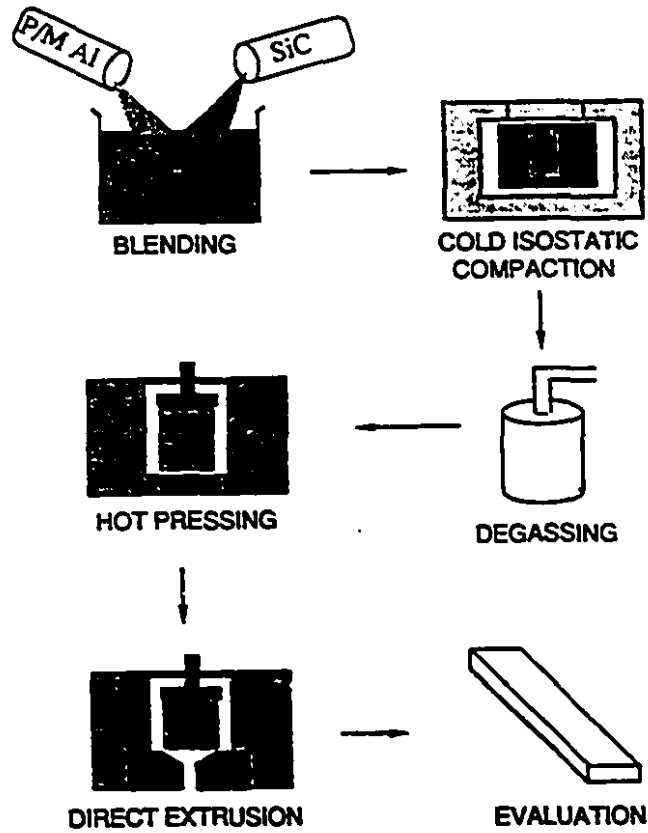


Figure 2.8 - The ALCOA process

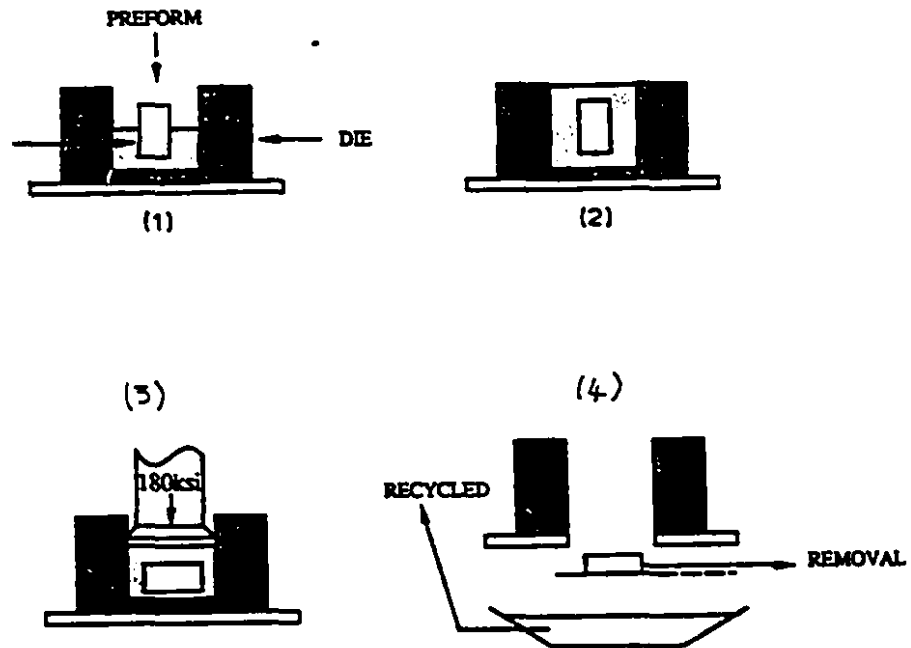


Figure 2.9 - The CERACON process

### 2.12.2 High-energy-high-rate processes

These processes<sup>54,55</sup> have been successfully utilized to consolidate rapidly quenched powders containing a fine distribution of ceramic particulates. This approach involves the consolidation of a metal-ceramic mixture through the application of high energy over a short period of time. Both mechanical and electrical high energy sources have been used to consolidate PMMCs. For example, Marcus et al.<sup>74</sup> were able to consolidate Al-SiC PMMCs by heating a customized powder blend through a fast electrical discharge from a homopolar generator. An high-energy-high-rate of 1MW pulse permits the rapid heating of a conducting powder in a cold wall die. The short time at high temperature offers the opportunity to control phase transformation and the degree of microstructural coarsening not readily possible using standard powder processing methods. This process has been employed satisfactorily for the manufacturing of (Ti<sub>3</sub>Al + Nb)-SiC composites.

Although the results are encouraging, extensive work remains to be completed in order to assess the potential application.

### 2.13 Ti POWDER METALLURGY

Both the high cost of Ti and the high cost of machining these alloys have motivated the development of powder metallurgy (P/M) Ti technology, even if large scale commercial acceptance of Ti P/M has not yet been accepted. Some of the advantages are<sup>56</sup> :

- capability of making very complex shapes
- cost reduction
- isotropic mechanical properties

Ti P/M can be divided into conventional fine particle metallurgy (elemental approach) and coarse particle metallurgy (prealloyed approach). Since blended elemental powders only were used to fabricate sintered Ti/TiC composites in this thesis, only fine particle metallurgy will be discussed.

One of the lowest cost powders is produced from sponge which is also needed

in the arc-melting of Ti alloy ingots. Ti sponge fines can be made with almost the same impurity level as cast and wrought products, with the exception of some Cl contamination. The Cl content can be reduced to 0.05% by admixing low Cl content electrolytic Ti powder which contains as little as 0.02%Cl<sup>57</sup>. For instance, Ti alloys such as Ti-6Al-4V are made by blending elemental Ti powder with a master alloy.

The compaction techniques are either uniaxial cold compaction and/or cold isostatic compaction, as will be detailed in Chapter 4.

Sintering is carried out usually in vacuum at temperatures above the  $\beta$ -transus (1100°C-1300°C). The sintered compacts reach densities up to 99% of theoretical density. Further consolidation can be performed through hot isostatic compaction (HIP) techniques where near 100% relative densities have commonly been reached.

One of the main advantages of the elemental approach is the low cost of the starting powder and the considerable savings in energy usually needed to convert sponge to billet by the arc-melting process.

# Chapter 3

## Objectives

This work is aimed at fulfilling the following objectives :

- to explore the possibility of producing a new family of composites for lightweight applications
- to combine the high elastic modulus, hardness and wear resistance of TiC with the high ductility, machinability, specific strength, heat and corrosion resistance of Ti
- to study the effect of temperature, time and TiC content on the sintering behaviour
- to investigate the effect of sintering time and temperature on the reaction between the TiC reinforcement and Ti matrix
- to define and apply the optimum processing parameters to the fabrication of Ti-TiC particulate metal matrix composites.

# Chapter 4

## Experimental procedure

### 4.1 STARTING MATERIALS

The starting Ti metal powder, -325 mesh size (particles less than  $44\mu\text{m}$ ), was provided by *Aremco Products Inc.*, in Ossining, New-York, U.S.A. Its density is  $4.51\text{ g/cm}^3$  ( $\alpha\text{-Ti}$ ). The chemical composition and SEM micrograph of this powder are shown in Table 4.1 and Figure 4.1 respectively.

Table 4.1 - Chemical composition of Ti powder

purity	Cl	O <sub>2</sub>	Fe	Ni
99.7%	0.15%	0.023%	0.02%	0.01%
V	Cr	N <sub>2</sub>	H <sub>2</sub>	Si
0.01%	0.01%	0.005%	0.003%	0.002%

The Ti particles have a smooth surface and seem to be partially sintered. This is due to the Kroll fabrication process (cf. 2.8.1) which *Aremco* uses to form Ti sponge. Subsequently, the sponge is crushed, sieved, and leached in different orders and as many times as required, depending on the final powder.

The starting TiC powder, -325 mesh size was received from *Kennametal* (Macro division) in Port Coquitlam, British Columbia. TiC has a density of 4.93



Figure 4.1 - SEM micrograph of as-received Ti powder ( $\times 2000$ )  $\text{g/cm}^3$ . SEM micrograph of this powder are shown in Figure 4.2 along with the chemical composition (Table 4.2).

Table 4.2 - Chemical composition of TiC powder

Total Carbon	Free Carbon	Fe	N <sub>2</sub>	O <sub>2</sub>
19.77%	0.11%	0.10%	0.26%	0.21%

The TiC particles have a more irregular shape and are angular and faceted. Moreover, tiny particles can be seen on the picture. These fragments stem from the milling process used to reduce the particle size after the carbothermic fabrication of TiC (cf. 2.8.2).



Figure 4.2 - SEM micrographs of TiC powder ( $\times 1000$ )

## 4.2 POWDER PREPARATION MEASUREMENTS

### 4.2.1 Particle size characteristics

The as-received powders were sieved and the particle size analyzed by sedimentation. The sieved powders were attrition milled together using 2.5, 5, 10, 15, and 20 weight percent of TiC. Knowing the densities of both Ti and TiC the theoretical densities were calculated for each TiC content (Table 4.3).

Table 4.3 - The calculated density of the composites for each TiC content

%TiC	0	2.5	5	10	15	20	100
$\rho$ ( $\text{g}/\text{cm}^3$ )	4.510	4.5205	4.531	4.552	4.573	4.594	4.93

#### 4.2.1.1 Particle size distribution

Particle size and size distribution govern many properties of the final products made from powder, such as apparent density, compacting properties, sintering rate, dimensional change, and mechanical strength. Therefore, a special care must be taken concerning the choice of the particle size spectrum.

#### 4.2.1.2 Screening

A sieve analysis was conducted by using 38, 53, 75, and 106  $\mu\text{m}$  size openings screens. From this latter distribution, only the 400 mesh ( $< 38\mu\text{m}$ ) was utilized.

#### 4.2.1.3 Sedimentation

Sedimentation was used to determine the particles size of the Ti and TiC powders. This method is standardized in ASTM B 430. Appendix 3 gives the basic principles of operation along with the theory. Next paragraph will generally describe the sedimentation method.

The basic construction of the Sedigraph<sup>1</sup> is illustrated schematically in Figure 4.3. The radiation from an X-ray tube (1) with its associated power supply (2) is collimated by horizontal slits (3) to a beam 5 mm high and less than 1 mm wide. The small X-ray tube has a Tungsten target inclined at about 30° to a thin Beryllium window and is air cooled. In use, only the Tungsten L-lines are excited. The tube is operated at a power level of 13 Watts.

The X-ray beam passes through a sample cell (4) located midway between the collimating slits. The cell is of rectangular cross section, having internal dimensions (mm) of 1.27 wide, 3.50 high, and 0.35 thick. The windows are a 0.16 mm thick "Homalite" polymer.

The transmitted radiation is detected by means of a scintillation counter (5). The detected pulses are amplified, passed through a noise discriminator and then clipped to a constant voltage after which they pass to a diode pump circuit which produces a current proportional to the count rate and therefore to the X-ray

---

<sup>1</sup> Sedigraph 5000 D Particle Size Analyzer, Micrometrics Instruments Corporation, Georgia, U.S.A.

intensity. This current is converted to a voltage proportional to the logarithm of the change in current. The reading of the voltmeter recorder for the intensity of the X-ray beam is adjusted to 100% through the clear solution (i.e. pure liquid).

Once established, when the cell is filled with a suspension, a net output signal is produced that is directly proportional to the concentration of particles at the level of the cell that intercepts the X-ray beam. This signal is applied to the Y-axis of the X-Y recorder (7). The cell position is established as a function of time from the start of sedimentation by a programmed controller (6) that simultaneously positions the X-axis of the recorder to indicate directly the particle size corresponding, through Stokes' law (equation 4.1).

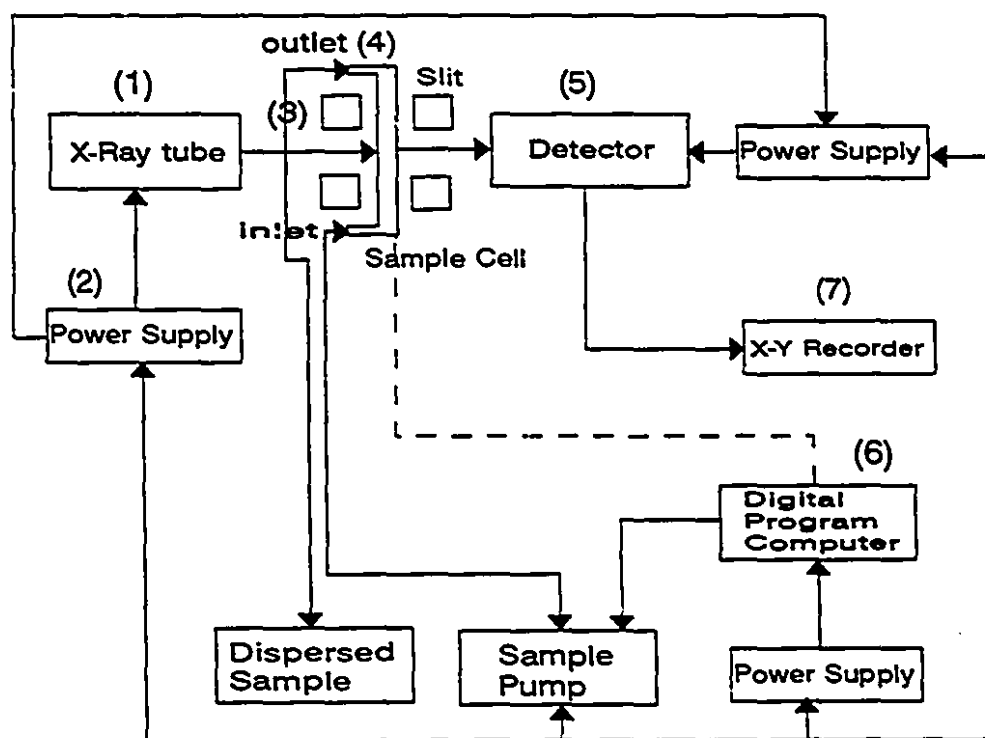


Figure 4.3 - Functional diagram of the Sedigraph

#### 4.2.2 Powder preparation

Premixing consisted on a manual agitation of the sieved powders in a glass container. The goal was to make sure that all the TiC powder was dispersed into

among the Ti powder in order to obtain a uniform mixture of the two components.

The different premixed compositions were wet attrition milled with isopropyl alcohol in a 4L teflon container at a speed of 200 RPM for 15 minutes. The ratio of solid to liquid was 1 to 5 by weight. Wet milling was chosen to eliminate packed particle problems which would lead to inadequate milling.

Alumina ( $\text{Al}_2\text{O}_3$ ) (99.7% pure) milling beads, having a diameter of 3.7 mm, were used in the proportion of five times the weight of powder used. Figure 4.4<sup>58</sup> shows a schematic of an attrition milling. It is cylindrical and contains grinding media

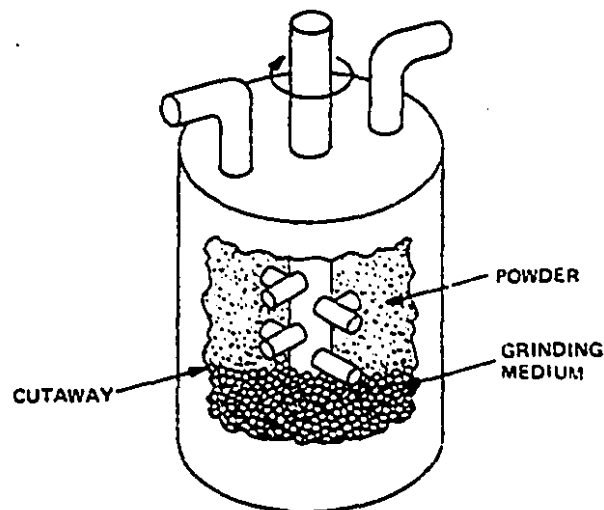


**Figure 4.4 - Schematic of an attrition mill**

agitated by stirring arms mounted to an axial shaft. After attrition milling, the slip was separated from the media by passing it through a 212  $\mu\text{m}$  sieve. The composite powder was then dried in a microwave oven, with extreme precautions because it is a flammable product. It was then stored in a conventional oven at 130°C for at least 24 hours in order to remove any trace of alcohol.

Figure 4.5 in previous page is a flow diagram of the processing route used for preparing the powder prior to green compact fabrication.

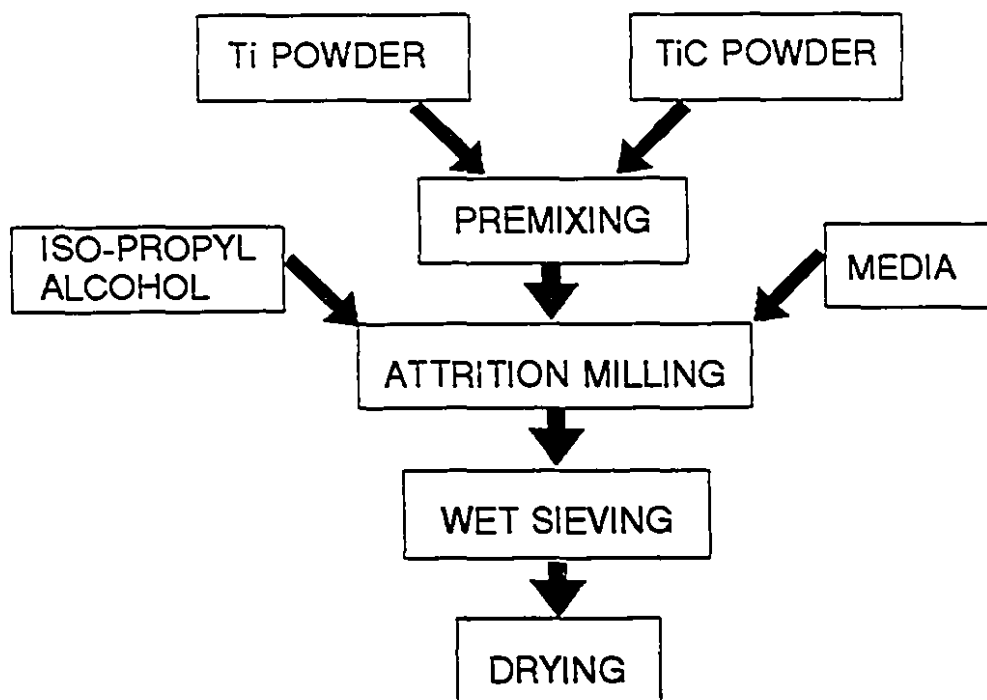


Figure 4.5 - Processing route for attrition milling powder

### 4.3 GREEN COMPACT FABRICATION

#### 4.3.1 Die-pressing

The Ti/TiC green samples were compacted with a rigid steel die<sup>1</sup> using a pressure of 207 MPa (30,000 psi). Such a high pressure was used to maintain the integrity of the pellet during handling prior to isostatic compaction or sintering. At lower pressures, the compacts tended to be too fragile and to crumble. The minimal handling strength needed at this stage is called the green strength.

Finally, cylindrical specimens were mechanically formed by uniaxially pressing the powder as a pellet ( $D = 12.2 \text{ mm}$  ( $\sigma=0.3$ );  $h = 5.7 \text{ mm}$  ( $\sigma=0.7$ )). The press consisted of a special hard-metal die with a single-action punch. The powder was pressed against the lower cylinder by the downward motion of the upper punch. This

<sup>1</sup> CARVEL laboratory press, Wisconsin, U.S.A.

cold pressing method provided better support for the fragile compact during ejection. A binder was undesirable because of the high reactivity of Ti and Ti alloys in general. Figure 4.6 shows a flow diagram for the fabrication of samples.

#### 4.3.2 Isostatic compaction

High-quality compacts require uniform density throughout. This was ideally accomplished by compaction using an isostatic press<sup>1</sup>. In this method, a hydraulic pressure is applied simultaneously and uniformly from all sides toward the centre of the compact and minimizes frictional losses against the die walls. The pressure used was 207 MPa (30,000

psi). The green samples were inserted into a rubber mould and air was removed with a vacuum pump. The mould was then sealed and placed into a steel cylindrical vessel filled with an emulsion of water and oil. The vessel was closed, the system was pressurized thereby compressing the compact in the mould. After the pressure was released, the piece was removed from the rubber mould.

#### 4.4 SINTERING

Once the powder was compacted and dried (one night), the density and

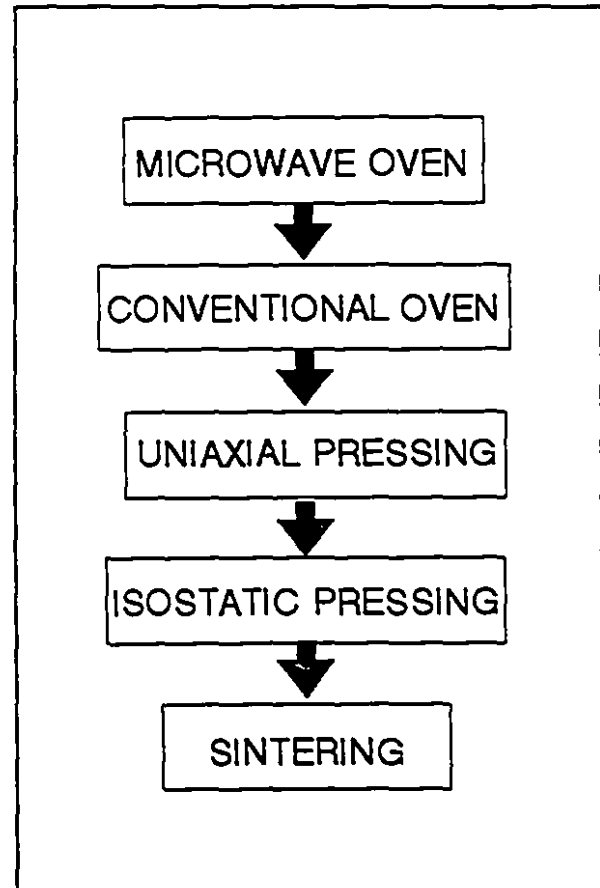


Figure 4.6 - Processing route for fabricating pressed pellets

<sup>1</sup> Isostatic Press model IP3-22-60-110, Autoclave Engineers, Ohio, U.S.A.

dimensions of the green body were measured. The green density was calculated from dry weight and dimensions.

The green samples were densified by sintering in a water cooled, vacuum, graphite element furnace, shown in Figure 4.7. No external pressure was applied during densification. The furnace was equipped with a rotary pump of sufficient capacity to accommodate outgassing during heatup and maintenance of high vacuum (4-5 Pa) at peak temperatures. The thermocouple<sup>1</sup> was

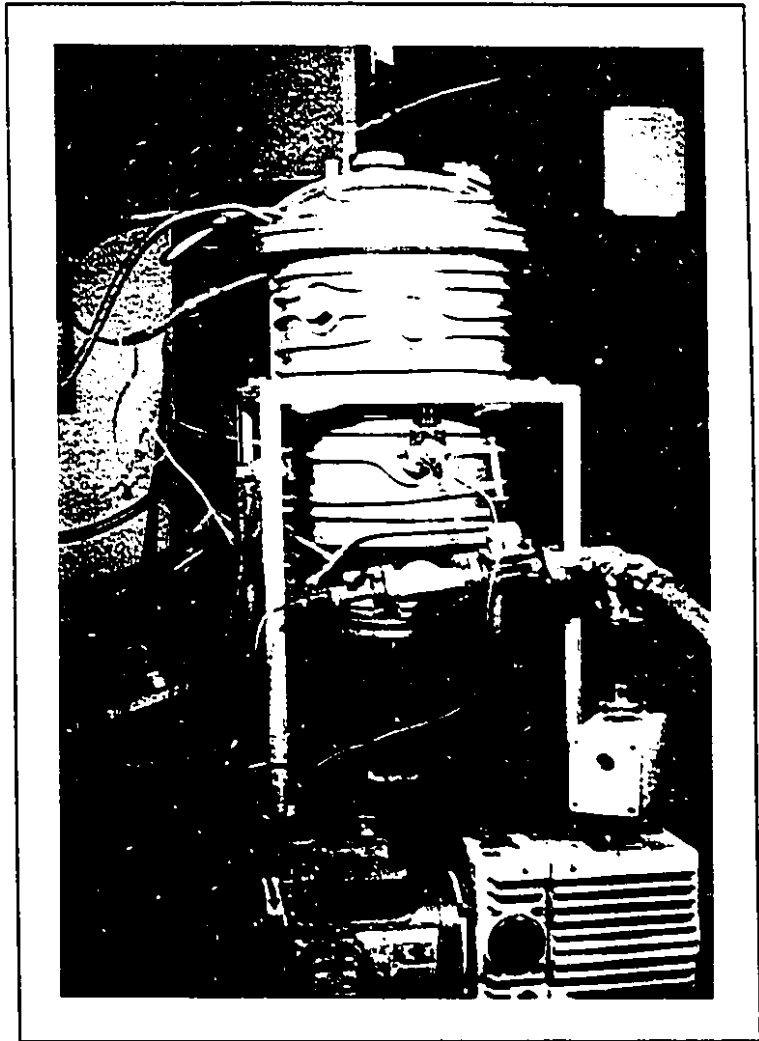


Figure 4.7 - Water-cooled graphite element furnace  
located at the centre of the furnace. It was connected to a digital controller which gave the inside furnace temperature with a  $\pm 2^{\circ}\text{C}$  precision.

The Ti/TiC samples were placed on a small graphite cylinder above the thermocouple. The controlled<sup>2</sup> time / temperature cycle referred to a heating rate of  $20^{\circ}\text{C}$  per minute and a cooling rate of  $50^{\circ}\text{C}$  per minute at the beginning (i.e. the

---

<sup>1</sup> Type C thermocouple (W 5%Re vs W 26%Re)

<sup>2</sup> Omega Model CN-2010 controller, Omega Engineering Inc.

first 10 minutes) which at the end of the cycle dropped down to 5°C per minute upon cooling (Figure 4.8).

Due to its reactivity, Titanium adheres to most support materials after sintering. The preferred setting<sup>1</sup> used was a piece of boron nitride, which has no reactivity with Ti and is able to maintain its strength at high temperature. Also, this support avoided any contamination due to carbon diffusion from the graphite cylinder.

Again due to the highly reactive nature of the composite, vacuum was used for all the experiments. Thus, parts were protected from reactive gases, and the furnace may be backfilled with an inert gas (argon) in order to improve the vacuum and to flush out oxygen. Sintering was carried out at temperature ranging from 1300-1600°C for 0.5-4 hours.

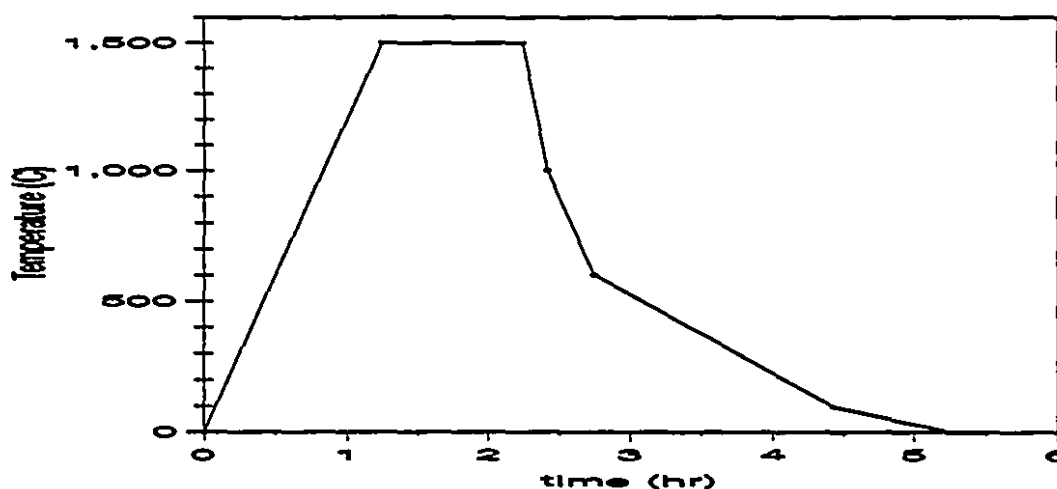


Figure 4.8 - A typical time/temperature furnace cycle

At the end of an experiment, the furnace was backfilled with high purity argon (99.998%)<sup>2</sup> When atmospheric pressure was reached, the furnace lid popped

<sup>1</sup> Setting refers to the way the part being sintered is supported in the furnace.

<sup>2</sup> Prepurified Argon UN-1006 ( $N_2 \leq 15$  ppm,  $O_2 \leq 5$  ppm,  $H_2O \leq 3$  ppm) Medigas Inc., St Laurent, Quebec

up and was manually removed. The extent of densification was measured by calculating the density of the samples after sintering using Archimedes' principle as laid out in ASTM C373-72<sup>59</sup>.

## 4.5 MATERIAL CHARACTERIZATION

### 4.5.1 Measurement of density

Typical methods of measuring density depend on Archimedes' principle, in which hydrostatic forces in liquids exert buoyancy forces proportional to the part volume. The difference in weight between an object weighed in air and its weight when suspended in water is equal to the object volume assuming the density of water is  $1 \text{ g/cm}^3$ .

#### Procedure

The procedure was the following<sup>64</sup> :

- 1/ the specimens were dried by heating in an oven at  $130^\circ\text{C}$  for 24 hours followed by cooling in a desiccator. Then, the dry mass  $D_m$  was determined for each of them to the nearest 0.001 g using a microbalance.
- 2/ the specimens were boiled in distilled water for 5 hours, taking care that the specimens were covered with water at all times. Each specimen, placed in the middle of its own container, had no contact with the sides. The container was filled up with glassy beads prior to place the sample. After boiling, the samples were allowed to soak for an additional 24 hours.
- 3/ after impregnation of the test specimens, the mass  $S$  of each sample while suspended in water was determined. The weighing was performed by placing the sample in a basket suspended from one arm of the balance.
- 4/ finally the saturated mass  $M$  of the wet sample ( $M > S$ ) was determined by removing all excess water from the surface with a *Kimwipe* cloth. This blotting operation was performed by rolling the sample lightly on the wet cloth and pressing it gently to remove the surface water. Excessive blotting will introduce error by withdrawing water from the open pores of the specimen. The weighing must be done

immediately after blotting.

#### Calculation

Approximating the density of water as unity (0.997 g/cm<sup>3</sup>):

$$V_B = M - S \quad 4.1$$

where  $V_B$  is the bulk volume (cm<sup>3</sup>),  $M$  is the weight in air (g), and  $S$  is the weight of object suspended in water less the weight of the suspending wire (g) in water which may be tared. The bulk density ( $\rho_B$ ) is then

$$\rho_B = \frac{D_m}{V} \quad 4.2$$

From equation 4.5 the relative density (RD in %) is then

$$RD = \frac{\rho_B}{\rho_{th}} \times 100 \quad 4.3$$

with  $\rho_{th}$  being the theoretical density depending on the ceramic content (Table 4.3).

#### 4.5.2 Porosimetry measurements

##### 4.5.2.1 Mercury porosimeter

A mercury porosimeter<sup>1</sup> had been used for measuring both particle size and particle size distribution of the pores of isostatic pressed green samples of pure Ti. *Mercury porosimetry* measures the volume of mercury intruded into the powder sample as a function of the pressure applied to the mercury.

Penetration of porous solids by mercury under pressure was used to characterize the pore volume and pore size distribution of interconnected pores ranging from 500 to 0.006 microns in diameter. The porous material to be analyzed was placed into a mercury porosimeter, in which the volume of mercury absorbed by the pores was measured as a function of the pressure applied to the mercury.

##### 4.5.2.2 Theory

---

<sup>1</sup> Mercury/Non-Mercury Porosimeter, Porous Materials Inc.

The basic equation used in mercury porosimetry was derived by Washburn<sup>60</sup> in 1921 from Young and Laplace's equation for the rise or depression of liquids in capillaries :

$$P = \frac{-4\gamma\cos\theta}{D} \quad 4.4$$

where  $P$  is the pressure (Pa) required to force the mercury through a pore of diameter  $D$  (m);  $\theta$  is the contact angle between the mercury and the porous material; and  $\gamma$  is the surface tension (N/m) of the mercury. The above equation applies to cylindrically shaped pores (thus, may require corrections for irregularly shaped pores). Mercury is used as the intrusion liquid because it does not wet most materials<sup>61</sup> (contact angle  $180^\circ > \theta > 90^\circ$ ), a fundamental requirement of the method.

#### 4.5.2.3 Principles of operation

To develop a pore size distribution, a weighed sample of powder or porous solid material was placed in the sample space of the penetrometer (a glass tube with graduated capillary stem). The penetrometer assembly was then placed in the mercury filling device. After evacuation, the penetrometer was automatically filled with mercury so that the sample was completely covered. The volume of the coarse pores (17 to 100 microns) was measured by volume changes in the mercury in the capillary stem as the pressure on the mercury was increased from the evacuated state to atmospheric pressure. The penetrometer was then transferred to the hydrobaric pressure chamber. The volume of smaller pores was determined by the change in volume in the penetrometer stem as the pressure on the mercury in the sample increased from atmospheric to the pressure limit of the instrument. The pressure range for the commercial porosimeter used was 205 MPa. Such a pressure corresponds to a pore size of 0.006 microns.

#### 4.5.3 Preparation for microscopic examination

Metallographic preparation of a porous material is significantly different

from preparation required for wrought materials, and several precautions are warranted. The Ti/TiC sintered compacts were mounted using a cold-setting epoxy resin and sectioned perpendicular to the flat surface using a diamond cut-off wheel<sup>1</sup>. The mounted samples were polished using an automatic polisher<sup>2</sup> equipped with a load controller<sup>3</sup>. The polishing procedure consisted of wet grinding the samples using 240, 400, and 600 grit diamond discs followed by 15, 6, and 1  $\mu\text{m}$  diamond pastes on nylon polishing cloths. After each polishing step, each sample was ultrasonically cleaned in isopropyl alcohol to avoid contaminating the next, finer stage.

Special care had to be taken when polishing the Ti-TiC composites. Since TiC is much harder than Ti, pullout problems had to be overcome concerning the ceramic particulates. Following this, numerous scratches in the Ti matrix were often observed. The best polishing method was low pressure, low speed (100-200 RPM) and longer grinding times (around 3 min.) than diamond polishing (< 1 min.). All the polishing was done manually since automatic polishing always gave poor results.

#### 4.5.4 X-Ray Diffraction analysis (XRD)

The as-received powder was identified by XRD. Each powder was spread on a special holder and analyzed with an X-Ray diffractometer<sup>4</sup> using filtered  $\text{CuK}\alpha$  radiation, a 40 kV accelerating voltage and a 20 mA beam current, with a scanning speed of  $0.02 \text{ deg. sec}^{-1}$ . A  $5^\circ$  to  $100^\circ$  range was selected for the angle  $2\theta$ . The phases were later verified using Electron Dispersion Spectroscopy (EDS) and X-Ray Mapping (cf. 4.5.6), on the SEM.

#### 4.5.5 SEM analysis

Different techniques were available while using the Scanning Electron

---

<sup>1</sup> LECO CM-15

<sup>2</sup> LECO VP-150 VARI/POL

<sup>3</sup> LECO AP-50

<sup>4</sup> Philips X-Ray diffractometer APD 1700

Microscope<sup>1</sup> to analyze the samples. First of all, secondary and backscattered imaging were employed. Secondly, compositional analysis was performed using the SEM in conjunction with a microcomputer-based energy dispersive X-Ray spectroscopy (EDS) unit. The X-ray signal from the sample passes through a thin Be window into a cooled lithium (Li)-drifted silicon detector. Absorption of each individual X-ray photon leads to the ejection of a photoelectron which gives up most of its energy to the formation of electron-hole pairs<sup>62</sup>. They in turn are swept away by the applied bias to form a charge pulse which is then converted to a voltage by preamplifier and finally passed to a multichannel analyzer (MCA), where the pulses are sorted by voltage.

The X-Ray detector<sup>2</sup> was inclined at 60° to the column axis, thus increasing collection efficiency. It was coupled with a beryllium (Be) window (7.6 μm thick) and an ultra thin Aluminum window (0.1 μm thick) allowing detection of very light elements (such as carbon in the case of Ti/TiC composites). Finally, qualitative phase analysis was possible through X-Ray mapping<sup>3</sup>.

To facilitate the analysis of the samples, they were mounted, sectioned, and diamond polished down to 0.1 μm. As the Ti/TiC composite was sufficiently conductive, no metallic coating was necessary but a copper tape was applied between the sample and the holder as a conductive bridge prior to SEM observation. Just before insertion of the sample, dust was removed with a gas spray.

#### 4.5.6 X-Ray mapping

X-Ray mapping was performed using the TN-8500 Advanced Imaging System, run by the OS-9<sup>TM</sup> operating system, and a TN-5500 X-Ray Analysis System, linked together through a console to provide integrated EDS and imaging functions. The main processing steps include image acquisition, X-Ray set-up (which defines the

---

<sup>1</sup> JEOL JSM-840 A

<sup>2</sup> Tracor Northern TN-96-606E31513

<sup>3</sup> Tracor Northern TN-8500

elements and regions of interest being scanned), and finally the parameter set-up which specifies the resolution of the map whereby choosing a pixel dwell time among 32, 64, 128, and 512.

Once all of the above procedures had been performed, the program will plot maps of each element plus the original video image over the same selected area.

#### 4.5.7 Image analysis

Image analysis consisted of sample selection and preparation (cf. 4.5.3), image preprocessing, measurement, and data analysis. Each step had to be properly controlled to obtain accurate and reproducible results.

The image analyzer<sup>1</sup> used had a scanner to display the image coming from the SEM on a television screen, an electronic processor for image detection, and a data hard copy device. The image analyzer was coupled with the SEM through the IPA 57 program. The particle-size was measured using ASTM E 112<sup>63</sup> standard.

The main steps include, first, the image acquisition where a backscattered image of the sample is transferred to the analyzer, digitized and stored. The digitized image is constructed by grey-level pixel ranging from 0 to 255. Then, a binary image is built with only a two state-pixel "on" and "off" corresponding to "white" and "black" by increasing or decreasing the grey-level spectrum. It should be noted at this stage that the image acquisition consisted on ten different image locations taken relatively far from the edge, as a drastic increase of the porosity along with a lower image quality was observed on the edges of the samples. This will be further discuss in Chapter 5.

The third step consists of the measurement whereby the selected binary image is processed so that geometric quantities such as area, perimeter, shape factor, average diameter, length, width, and aspect ratio are computed.

Finally, the results can be further analyzed and discussed in terms of pore size and pore size distribution, percentage of pores throughout the composite, size

---

<sup>1</sup> Tracor Northern TN-8500

of TiC particles, or percentage of TiC phase.

#### 4.5.8 Microprobe analysis

Electron Probe Microanalysis<sup>1</sup> (EPMA) enabled the combination of structural and compositional analysis in one operation. It is generally used for qualitative and quantitative elemental analysis of solids for elements with atomic number (Z) greater than 11 (Na).

Consequently, the EPMA was unable to detect carbon (Z = 6). Therefore, all the carbon measurements recorded in Chapter 5 have been generated by difference between the standard and the titanium (Z = 22) present in the matrix of the Ti-TiC samples. An uncertainty of  $\pm 2\%$  in weight percent was assessed. The standard used was a pure (> 99.99%) TiO<sub>2</sub> material. Measurements of C were done by difference with Ti content since only two elements were present.

EPMA is based on the wavelength dispersive spectroscopy (WDS), that is on the measurement of characteristics X-Rays emitted from a microscopic part of a solid specimen bombarded by a beam of accelerated electrons. The primary electrons are focused into a beam of 1  $\mu\text{m}$  in diameter so that a limited microvolume can be chosen from the surface of the specimen. The primary electrons are decelerated and scattered. They lose energy and suffer directional changes through collision with the specimen atoms, which limits the maximum depth of penetration to about 1  $\mu\text{m}$ . A small portion of the X-ray signal generated from the specimen passes out of the electron optical chamber and impinges on an analysing crystal. If Bragg's law is satisfied,

$$n\lambda = 2d\sin\theta \quad 4.8$$

(where n is an integer,  $\lambda$  is the characteristic X-ray wavelength, d is the interplanar spacing of the crystal, and  $\theta$  is the angle of incidence of the X-ray on the crystal), the characteristic elemental X-rays are diffracted and detected by a proportional

---

<sup>1</sup> Cameca, Camebax

counter. Sample preparation was the same as for SEM (cf. 4.5.3).

#### 4.5.9 Vickers microhardness and Rockwell hardness testing

The machine used was a Vickers microhardness tester<sup>1</sup>. Care is exercised in preparing the sample surface and a preliminary thorough polishing was required before any microhardness testing. The hardness value was determined by measuring the size of the resulting indentation using a microscope coupled to a microcomputer which converted results to Vickers hardness numbers ( $\text{kg/mm}^{-2}$ ) in accordance with ASTM E 384<sup>64</sup>. The tester featured an automatic test cycle (load, application, time of application, and removal of the indenter). The required area was first located with the microscope. The indenter automatically moved above the sample and the indentations were made with a load of 25–50g. The indenter is then returned to its original location, so that the dimensions can be determined with the microscope. At least six readings were taken and averaged.

The Rockwell test<sup>2</sup> consisted of the penetration of a C "brale"<sup>3</sup> type indenter onto the material using a 150 kg load. Prior to testing, a calibration was performed using two Rockwell standard blocks ( $25.6 \pm 0.1$  HRC and  $62.5 \pm 0.1$  HRC). A simple meter allowed the reading of the HRC value. The distance from the centre and from the edge of one indentation to another was at least three indentation diameters.

The results obtained by using all the above characterization techniques will be presented and discussed in the next chapter.

---

<sup>1</sup> Hardness tester LECO Model M-400-G2

<sup>2</sup> Rockwell hardness tester Wilson Model 8-OUR

<sup>3</sup> The word "Brale" is a registered trade mark and is stamped in the nib of each diamond penetrator standardized in Wilson testing laboratory.

# Chapter 5

## Results and discussion

As outlined in Chapter 2, there is very little literature on Ti-TiC MMCs, their sintering behaviour and microstructure over a wide range of TiC content. Most of the work was performed on either another type of reinforcement or with other matrices.

For this reason, the first objective of this work was to identify the microstructures formed after sintering at 1300-1600°C for different sintering times. The first part will analyze particle size distribution and give results on the isostatic pressing and porosimetry of the mixed powders. The second part will discuss the sintering behaviour. The microhardness and general hardness will then be investigated. A correlation between the microstructure with the sintering results in terms of density, pore and particle size will be presented. The last part will then discuss carbon diffusion involved in the sintering of these composites.

### 5.1 POWDER ANALYSIS AND PREPARATION

Analysis and preparation of the starting powders consisted of XRD, sedimentation, sieving, and premixing. XRD confirmed the starting powders to be pure  $\alpha$ -Ti and TiC.

The particle size distribution of particles less than 40  $\mu\text{m}$  was performed by the sedimentation technique and is shown in Figure 5.1 for both Ti and TiC starting powders.

Particle size data was collected for both screening and sedimentation (cf. 4.2.1), and is presented in Figure 5.2. The raw data from screening is compiled in Table 5.1 (a) and (b).

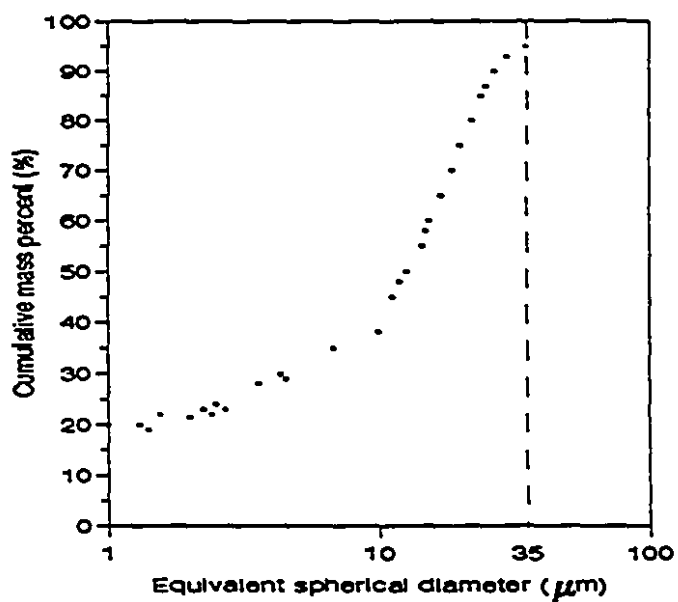
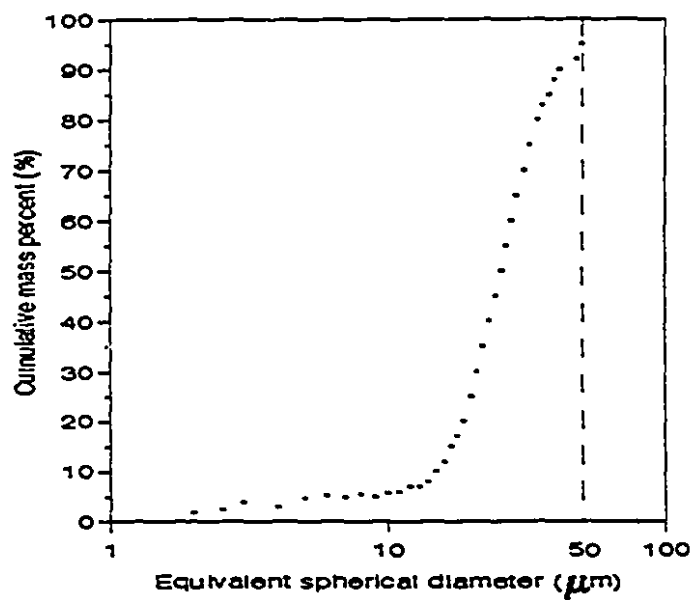


Figure 5.1 - Sedigraph of (a) Ti and (b) TiC

The total weight of the powder examined for each material was about 150 grams (i.e. 33.26 cm<sup>3</sup> of Ti and 30.42 cm<sup>3</sup> of TiC).

Combining Sedigraph and sieving data, the distribution of Ti and TiC powders is given in terms of a frequency plot or histogram as shown in Figure 5.2. The histogram is generated by plotting the incremental percentages versus the screen opening size. It gives the cumulative weight percent versus particle size by making the increment widths equal. The mode size was found to be between 25 to 38  $\mu\text{m}$  for Ti and between 15 to 25  $\mu\text{m}$  for TiC. The Ti size distribution exhibits a Gaussian type of distribution, which is very common in metal powders. On the other hand, it is clear that TiC powder presents a particle size distribution shifted to the left (small particles) compared to that of Ti powder, i.e. a log-normal distribution. It was expected that the TiC powder would reveal smaller particles since this material is more brittle and therefore fragments easily during the milling process (Figure 4.2).

A plot of the cumulative particle size distribution (Figure 5.3) shows a smooth curve from which one can extrapolate the average or mean value (50% particle size). Figure 5.3 gives a screening analysis with respect to the weight of powder. The mean size corresponds to the 50% value. Table 5.2 presents the mean values, as well as the particles sizes at the 90% and 10% limit for both powders.

Table 5.2 - Particle size for different cumulative percent

Cumulative Percent limit	Ti Particle Size	TiC Particle Size
90%	$\leq 37 \mu\text{m}$	$\leq 27 \mu\text{m}$
50%	$\leq 20 \mu\text{m}$	$\leq 12 \mu\text{m}$
10%	$\leq 11 \mu\text{m}$	$\leq 1 \mu\text{m}$

Table 5.1 (a) - Ti particle size distribution data

Opening ( $\mu\text{m}$ )	Weight (g)	Interval (%)	Cumulative (%)
> 106	1.86	1.24	100
> 75	4.47	2.98	98.76
> 53	6.12	4.08	95.78
> 38	37.83	25.22	91.7
> 25	45.51	30.34	66.48
> 15	43.33	28.89	36.14
> 10	5.43	3.62	7.25
> 5	5.415	3.61	3.63
< 5	0.03	0.02	0.02

Table 5.1 (b) - TiC particle size distribution data

Opening ( $\mu\text{m}$ )	Weight (g)	Interval (%)	Cumulative (%)
> 106	0.045	0.03	100
> 75	0.09	0.06	99.97
> 53	0.24	0.16	99.91
> 38	17.55	11.7	99.75
> 25	32.62	21.75	88.05
> 15	40.95	27.3	66.3
> 10	25.74	17.16	39
> 5	23.4	15.6	21.84
< 5	9.36	6.24	6.24

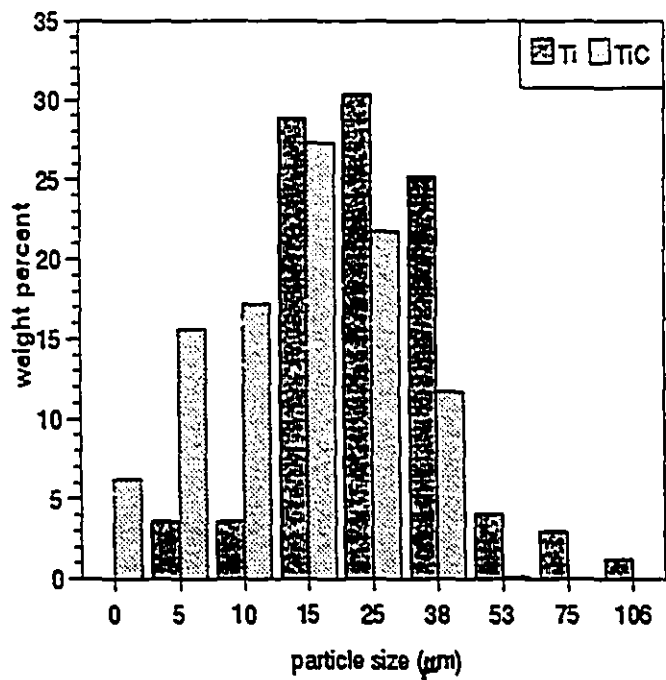


Figure 5.2 - Histogram plot of the particle size

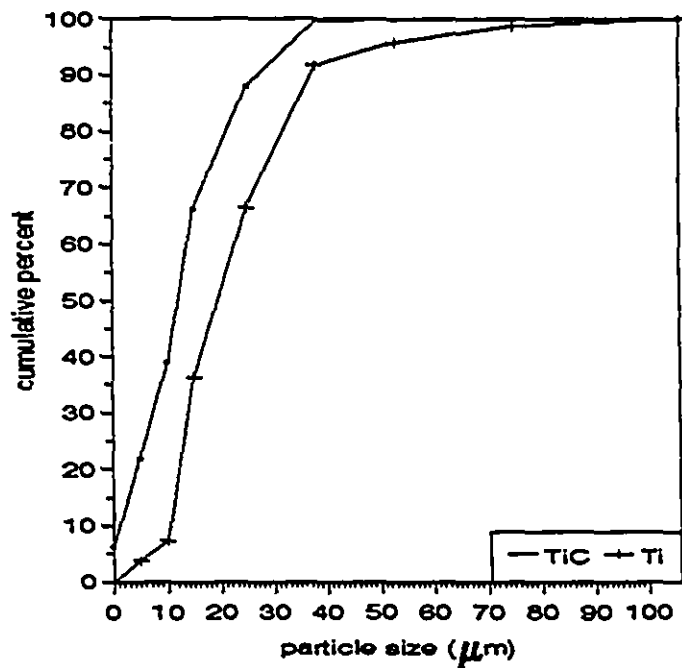


Figure 5.3 - Cumulative particle size distribution plot

From the particle size distribution, particles less than 38  $\mu\text{m}$  in diameter were chosen, since good sintering requires a high specific surface area, i.e. small particles, leading to a high driving force. Nevertheless, good green consolidation is also required, i.e. large particles with a wide range and so a compromise has to be made. This is why it is important to maintain a wide particle size range and not discard the very fine particles (e.g.  $< 5 \mu\text{m}$ ). Hence, an approximately 1–40  $\mu\text{m}$  particle size range was selected.

Referring to Figure 5.3, both powders have a homogeneous particle size distribution, which is desirable for uniform densification and is favourable for promoting good sintering.

#### Isostatic pressing

The same pressure of 207 MPa (30,000 psi) used for uniaxial pressing was utilised for isostatic compaction. By analysing the microstructure of the green samples after isostatic compaction, Figure 5.4 (a) indicates a uniform distribution without apparent particle agglomeration. This confirms the benefit of attrition milling starting powders.

A higher magnification micrograph (Figure 5.4 (b)) of a pure Ti green compact shows that the compaction pressure reached a critical level where the Ti particles are seen to have yielded and slightly deformed at their points of contact. Excessive plastic deformation at the green compaction stage could negatively influence the sintering behaviour and final properties.

Rearrangement occurs generally at very low pressure (less than 0.05 MPa). At higher pressure, plastic deformation is a major form of densification for metal powders, where extensive strain hardening begins to occur at 100 MPa. At higher compaction pressures (e.g. 310 MPa or 45,000 psi), massive deformation occurs. This could introduce an undesirable degree of cold work and anticipated fragmentation, especially in composite materials.

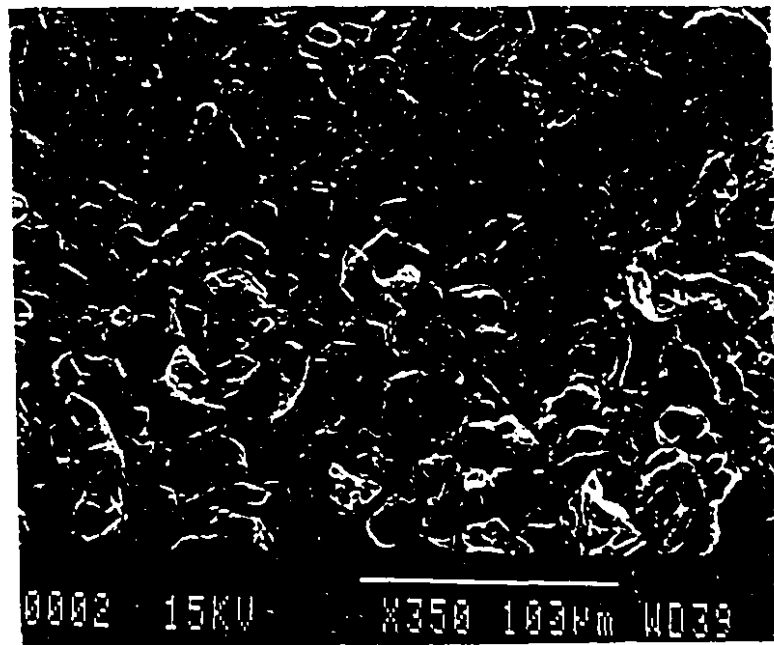


Figure 5.4 (a) - Pure Ti isopressed compact ( $\times 350$ )

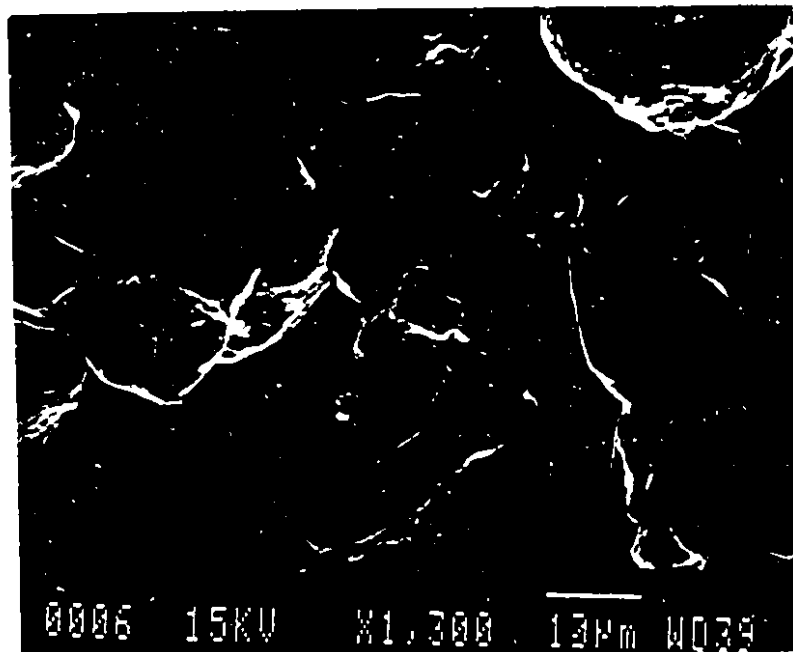


Figure 5.4 (b) - Pure Ti isopressed compact ( $\times 1,300$ )

### Porosimetry

Mercury intrusion porosimetry was employed to obtain the pore size distribution of green compact samples. By providing the sample weight and bulk density, the porosimeter gives the total percentage of open porosity as well as the green density (cf. 4.5.2). Examples of plots of pore volume versus size are shown in Figure 5.5 (a) for pure titanium and for Ti- 20wt%TiC, both isostatically pressed at 207 MPa.

Both curves exhibit the same type of trimodal pore size distribution for the pure titanium and the reinforced titanium. Both curves have a first interval where 30% of the pores are  $< 1 \mu\text{m}$  in diameter, a second interval around 60% of the pore diameter range, from 1 to  $5 \mu\text{m}$ . Finally, approximately 10% of the remaining pores exceed  $5 \mu\text{m}$  with only 5% above  $50 \mu\text{m}$ .

Note that the pore size distribution of the composite is shifted to the right, meaning that the composite contains larger pores than pure Ti. The fact that a non-homogeneous powder compact (20%TiC) gives rise to the formation of larger pores is expected, as well as an overall higher porosity of that compact (Figure 5.5 (b)). The median pore diameters (based on volume) are 2.5 and  $3.1 \mu\text{m}$  for the pure Ti and the composite, respectively.

The difference in porosity is more significant than in pore size (Figure 5.5 (b)). The porosity was found to be 26.7% for Ti and 36.8% for Ti-20wt%TiC, which gave a green density of 73.3% and 63.2% of theoretical density, i.e.  $3.30 \text{ g/cm}^3$  and  $2.90 \text{ g/cm}^3$  according to Table 4.3. The pores in the range 1-10  $\mu\text{m}$  contribute the most to the porosity of the green compacts. These densities are in good agreement with the green density measurements listed in Table 5.3. Note that adding TiC particulates did not improve the green density, as shown in Figure 5.5 (b). This is because the Ti and TiC particle size distributions are very similar, as illustrated in Figure 5.2 and 5.3. It simply means that the TiC are not small enough to fill up the interstices of Ti green compacts.

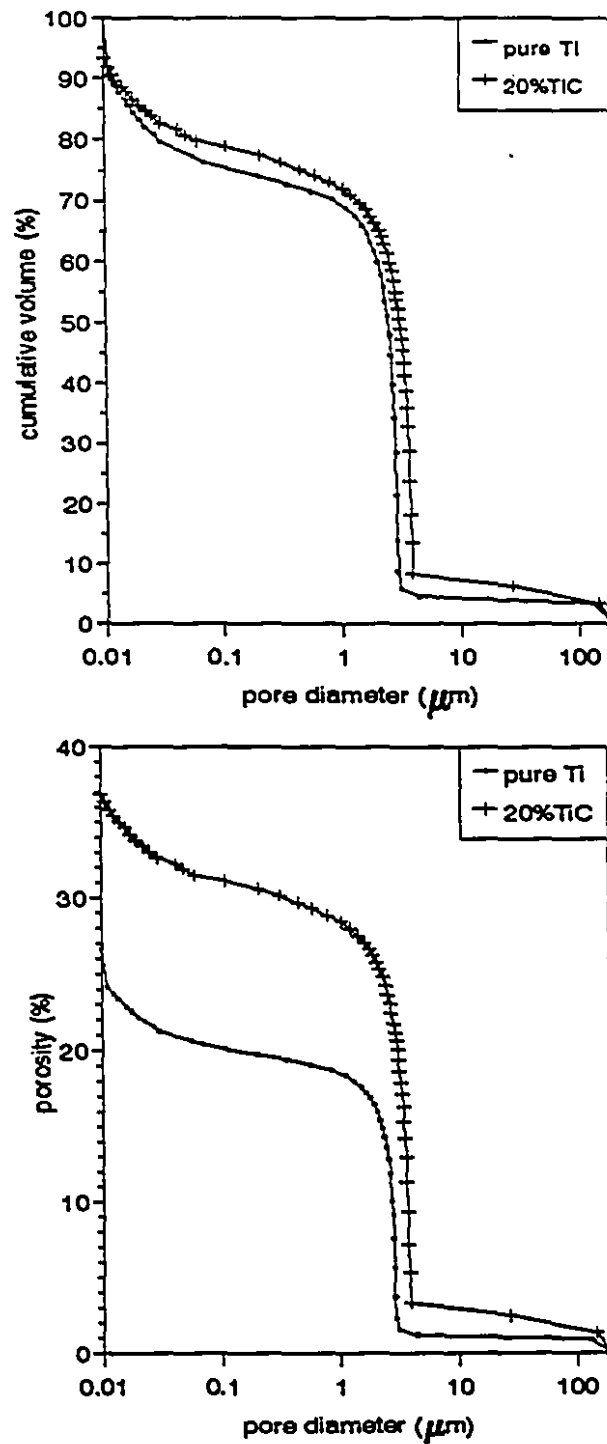


Figure 5.5 - (a) Cumulative volume and (b) porosity vs pore size of a pure Ti and a 20wt%TiC green compacts isopressed at 207 MPa

Table 5.3 - Densities and relative green densities for each TiC content

%TiC	Measured density (g/cm <sup>3</sup> )	Relative density (%)
0	3.12	69.18
2.5	3.10	68.51
5	3.08	68.0
10	3.10	68.10
15	3.26	71.28
20	3.14	68.35

## 5.2 SINTERING

This part of the study illustrates the influence of both sintering time and temperature as well as the effects of different TiC contents on the sinterability. The second part will attempt to correlate the sintering with the microstructure. Particle size of TiC along with the pore size distribution on the sinterability have also been investigated.

### Effect of milling

An initial study was carried out on pure Ti samples divided in two batches, as received and attrition milled. This experiment was to establish the effect of the attrition milling upon sinterability. No addition of TiC was made since no reaction with carbon was desirable. The following figure shows an example of the relative density of pure Ti samples for a sintering temperature of 1440°C as a function of time (Figure 5.6). These curves indicate an increase of the density of the milled Ti samples. Indeed, the average relative density gain, considering all the times and temperatures (Appendix 4), is nearly 5%, which is quite significant when considering that the relative densities are approaching their theoretical values.

This phenomenon is attributed to the removal of the  $\text{TiO}_2$  oxide layer by abrasion in the alcohol slurry during the milling process. The oxide is removed by particle/particle friction and also by media/particle contact. From the above discussion, it is seen that the oxide layer tends to inhibit sintering. Indeed, the sintering processes through diffusion of atoms. Thus, a lower thickness in the  $\text{TiO}_2$  layer will facilitate diffusion through the oxide layer and therefore promote better sintering.

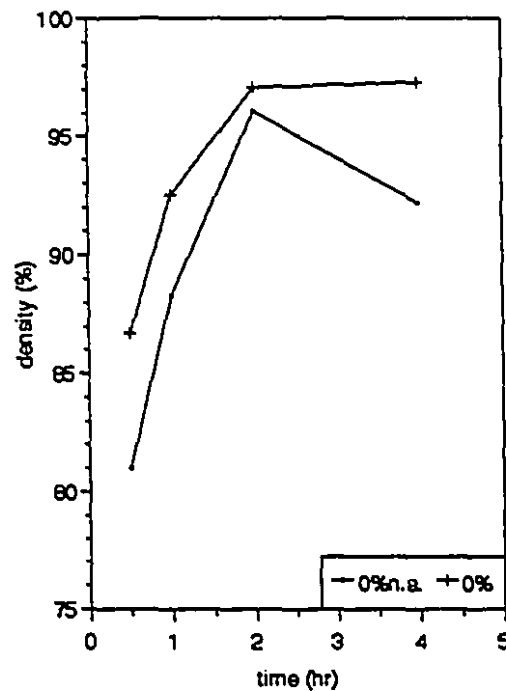


Figure 5.6 - Relative density of pure titanium attrition milled and non attrition milled at  $1440^\circ\text{C}$

#### Sintering behaviour

The milled and compacted specimens were sintered at  $1300\text{--}1600^\circ\text{C}$  for 0.5–4 hours. The Archimedean densities of different sintered Ti-TiC composites are shown in Figures 5.7 as a function of the sintering temperature for four different TiC content. The remaining TiC content graphs are given in Appendix 4 along with the corresponding raw data tables.

The density of these alloys increases with increasing temperature up to an optimum and then decreases with increasing temperature. This same trend is observed for every TiC content.

The shortest sintering times exhibit the poorest densities, at least up to 1440°C. Indeed, the densification process is more sensitive to time variations at low temperatures. Several authors<sup>65,66</sup> (cf.2.9.2) found an increase in density with increasing temperature throughout their range of sintering temperatures. However, their maximum temperature was much lower (around 1400°C), and indeed, they found only a small increase between 1200 and 1400°C (Figure 2.3). From this set of data, an optimum sintering temperature of 1440-1480°C was established for pure Ti and all the five TiC contents.

Figure 5.8 displays the densities at various temperatures as a function of sintering time. This set of graphs displays an optimum time of 2 hours for intermediate temperatures, i.e. near the optimum temperature. This is also true for pure titanium (Figure 5.6). As might be expected for low temperatures (1300°C), time seems to be an important factor since the relative density keeps increasing with time and, indeed, the best density occurs after 4 hours of sintering. At 1300°C, the relative density increases from 80% to 95% on average from 0.5 hour to 4 hours of sintering.

For intermediate temperatures, time does not play as important a role as for low temperatures. All the densities fall within a smaller interval, i.e. from 93% to 98% for 1480°C. This was expected since sintering and densification is much more sensitive to temperature than time (equation 2.11). As a corollary, at high temperature (1600°C), the curve show quite poor sintering with desintering occurring for times greater than 0.5 hour.

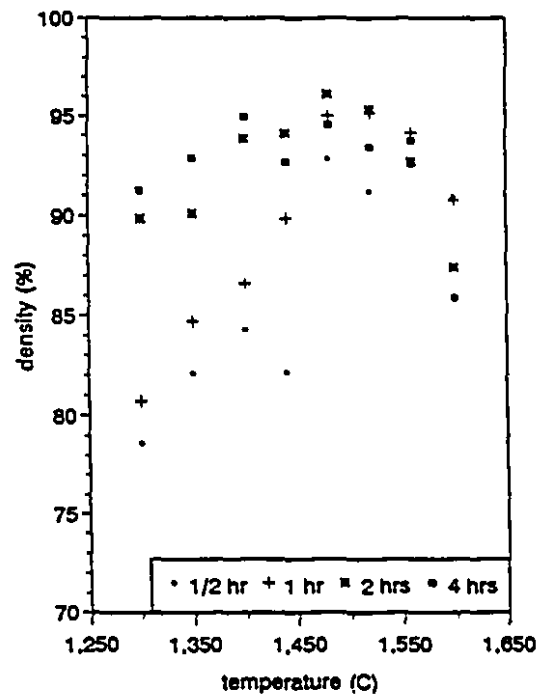
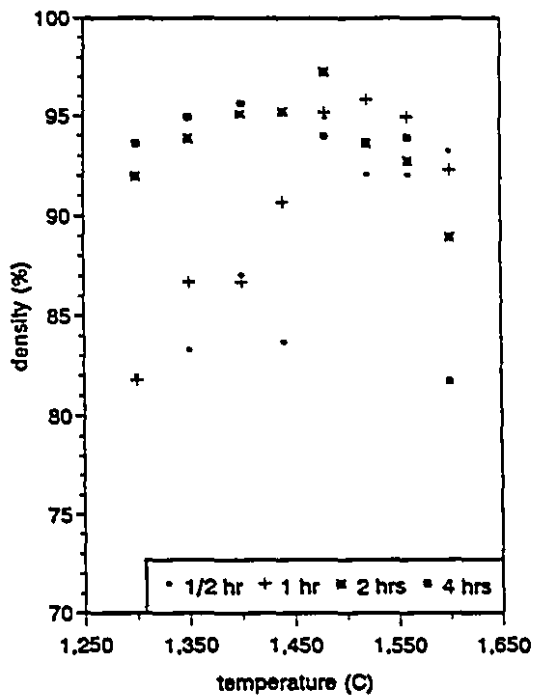
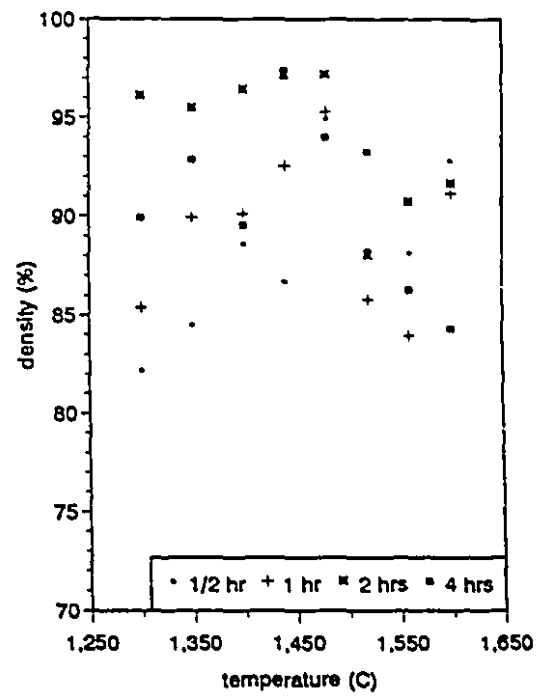
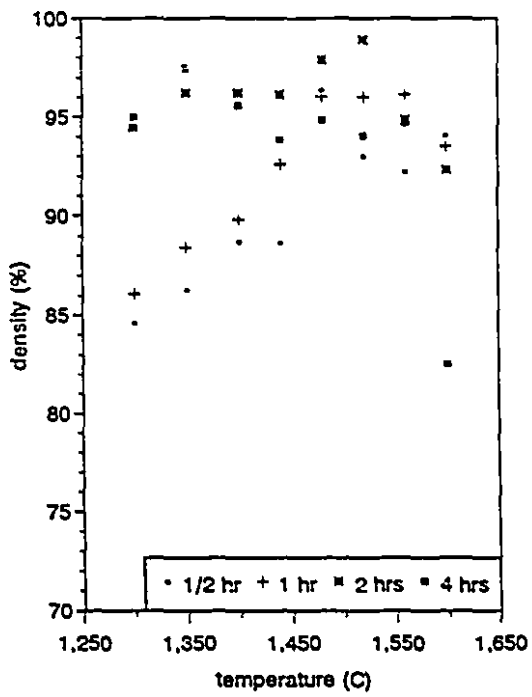


Figure 5.7 - Relative density vs temperature for (a) 0% (b) 5% (c) 10% and (d) 20%

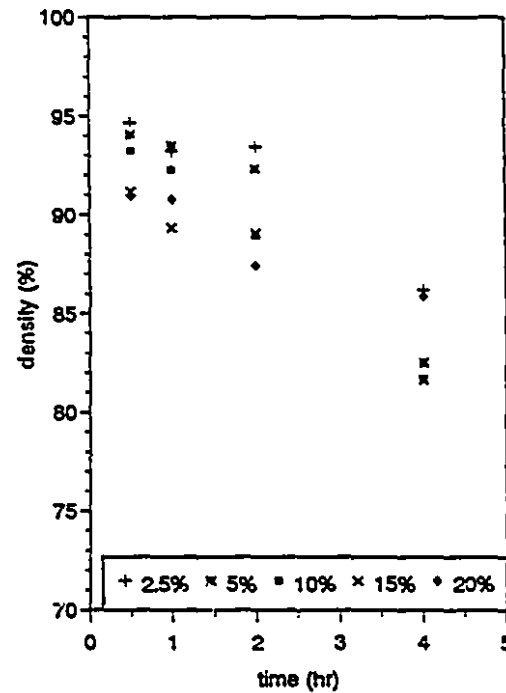
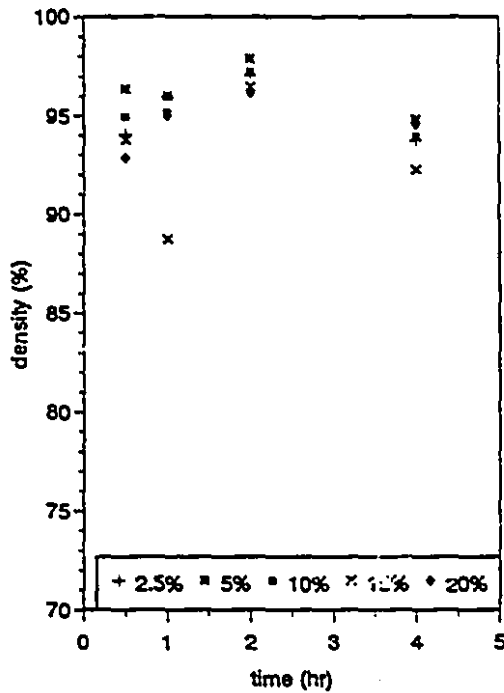
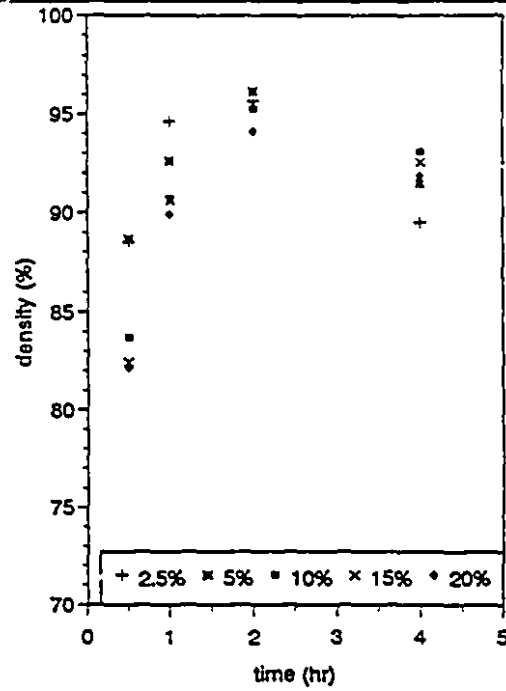
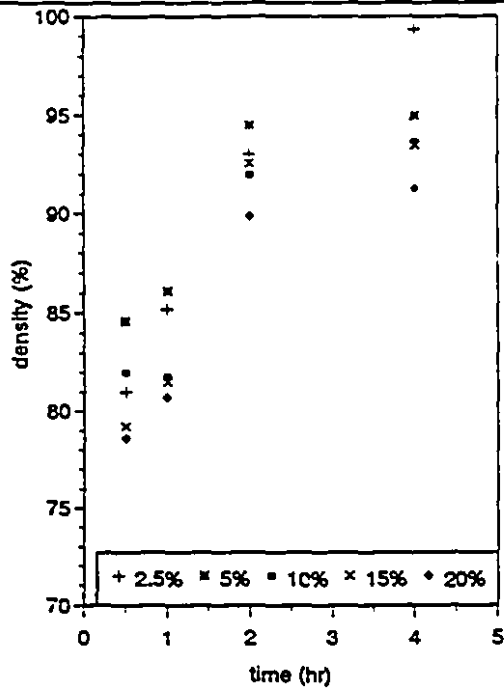
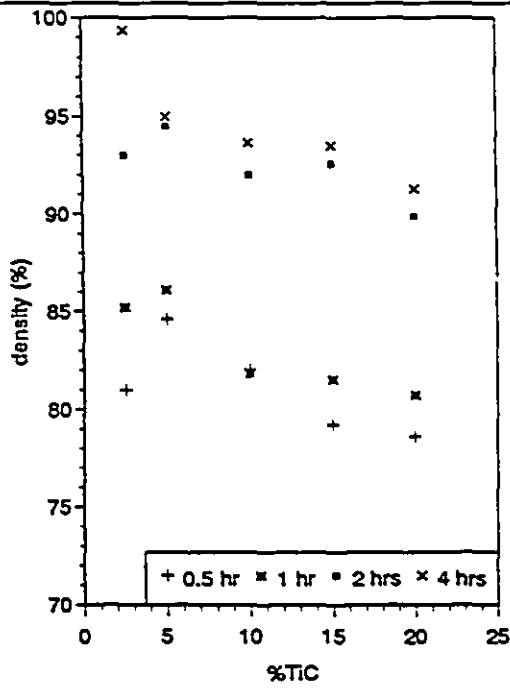
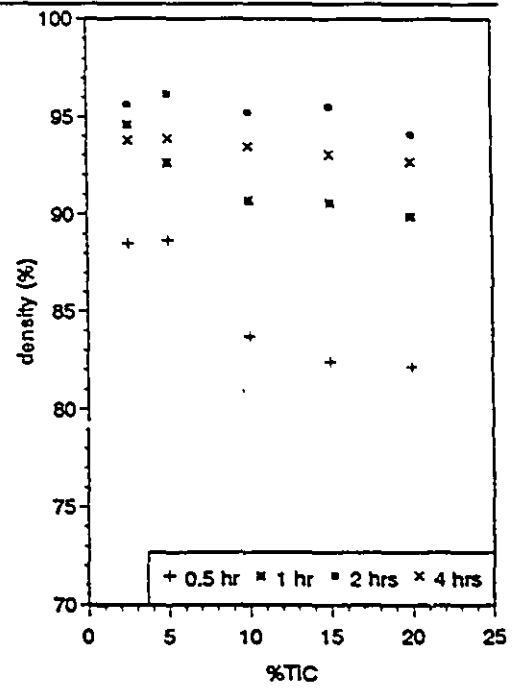


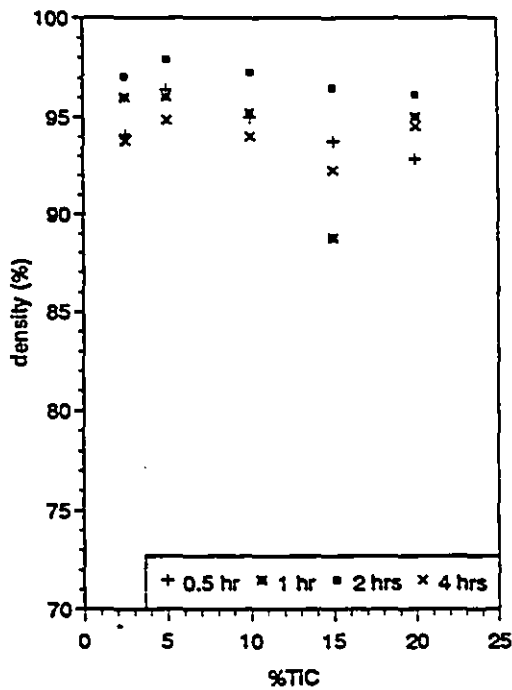
Figure 5.8 - Change in relative density with time at (a) 1300°C (b) 1440°C (c) 1480°C and (d) 1600°C



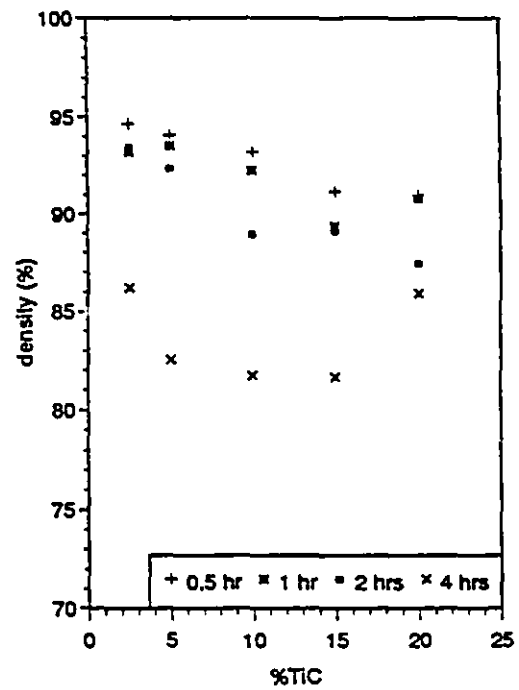
(a)



(b)



(c)



(d)

Figure 5.9 - Change in relative density with TiC content at (a) 1300°C (b) 1440°C (c) 1480°C and (d) 1600°C

Finally, the effects of different weight percentages of TiC on the sinterability of titanium are summarized in Figure 5.9. Evidence of an optimum TiC content is more difficult to define. Ti-TiC 2.5wt% and Ti-TiC 5wt% seem to show up a maximum density value. Moreover, there is a trend to decreasing densities towards higher TiC content. This can be related to the fact that a high TiC content tends to block sintering, since a ceramic needs a much higher temperature to sinter (the melting temperature of TiC is 3100°C).

Even though the best densities were obtained for 2.5 and 5wt% of TiC, it was found that the relative density of the pure Ti was often the same as that of Ti composites (Appendix 4). For instance, the relative densities at a sintering time of 2 hours are 95.5% and 96.2% (1350°C), 96.5% and 96.2% (1400°C), 97.1% and 96.1% (1440°C), 97.2% and 97.9% (1480°C), for pure milled Ti and 5% TiC respectively.

At 1300°C, the pure Ti is even better than the composite counterparts with a relative density of 96.1% (2 hours) compare to 94.5% for the best relative density obtained for Ti-5%TiC. On the other hand, for higher temperatures (1520-1600°C), there is a significant improvement in the density by addition of TiC. For example, at 1520°C and 2 hours, pure Ti gives 88.08% and 5%TiC gives 98.92%. Note again the increase in relative density at 1300°C (Figure 5.9 (a)) as well as the poor density at 1600°C for 4 hours (Figure 5.9 (d)). Furthermore, the scattering in the relative density appears to be the smallest at 1480°C. This indicates that temperature is a more dominating factor than time during the sintering of these materials.

To summarize, the sintering results show that the highest densities were obtained with 2.5-5 wt%TiC at a temperature of 1440-1480°C for about 2 hours and that the powders must be milled prior to compaction and sintering in order to remove the protective oxide layer which tends to inhibit sintering.

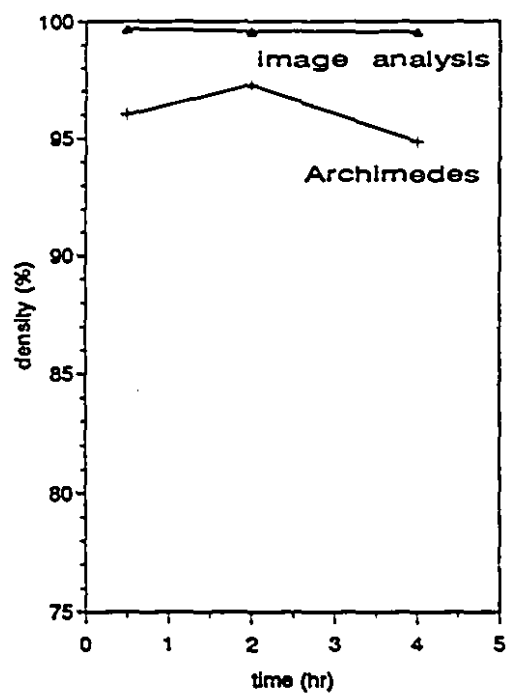
#### Image analysis

All the data of porosity/density measurement by image analysis of the relative

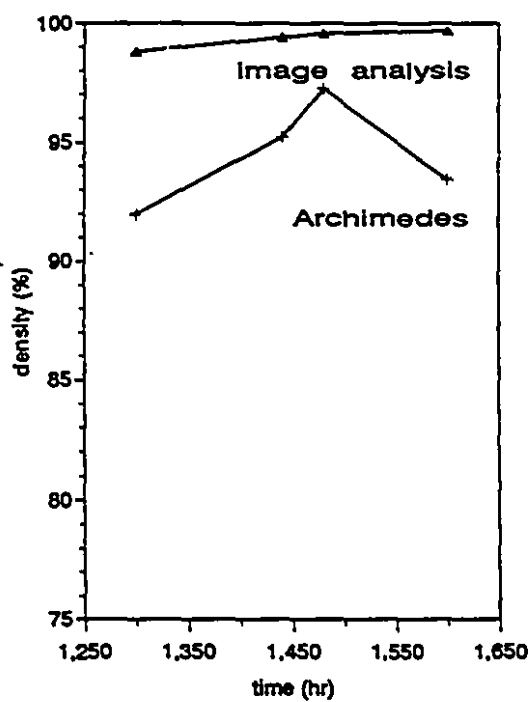
densities are displayed in Appendix 5. Image analysis was performed for three sintering times at four different temperatures. The results indicate the same trends as observed for bulk density measurements (Figure 5.7-5.9). However, the absolute values of relative densities were always higher than by the *Archimedean* method. Figure 5.10 presents the resulting curves of relative densities of Ti-10wt%TiC composites for which the data are presented in Table 5.4. Indeed, Figure 5.10 allows the reader to make an easy comparison of the *image analysis* densities (top curve) with the *Archimedean* densities (lower curve).

An average difference between both densities of 4.4% ( $\sigma = \pm 2.2\%$ ) was determined from Table 5.4. The difference is rather significant when approaching high densities and can be explained by the fact that Archimedes' method overestimates the amount of porosity. This is a surface effect since measurement include the sintered surface and leads to an unexpectedly high bulk porosity. This surface effect may clearly be seen on Figure 5.11 (a) on a 1300°C/4 hours Ti-5%TiC unpolished sintered sample. Figure 5.11 (b) shows the well sintered structure in the centre of the sample whereas Figure 5.11 (c) shows that the surface structure contains extensive porosity.

Figure 5.11 (d) and 5.11 (e) show the reaction layer for two different polished samples : 1300°C/4 hours and 1480°C/2 hours respectively, both containing 5%TiC. From these micrographs, a reaction layer of 30-100  $\mu\text{m}$  was observed. Assuming some oxygen in the atmosphere, both the oxidation of Ti and TiC are possible but that of C should occur more readily. The C can either come from the TiC, itself, or can be present in the microstructure as free C, since the as-received TiC powder contains 0.11%C (Table 4.2). Then the C might react with  $\text{O}_2$  to give CO. Also, due to reaction between graphite and oxygen, the furnace element can produce CO which might react with the surface layer. Thus, this surface reaction zone produces gases which would lead to an increase in the porosity. Therefore, it results in an increase in the measured volume which causes a corresponding decrease in the Archimedean bulk density (equation 4.5). Consequently, the relative densities measured by image analysis are more representative of the true relative densities of the samples.



(a)



(b)

Figure 5.10 - Comparison between the *Archimedean* densities and the *Image analysis* densities (a) at 1440°C and (b) for 2 hours

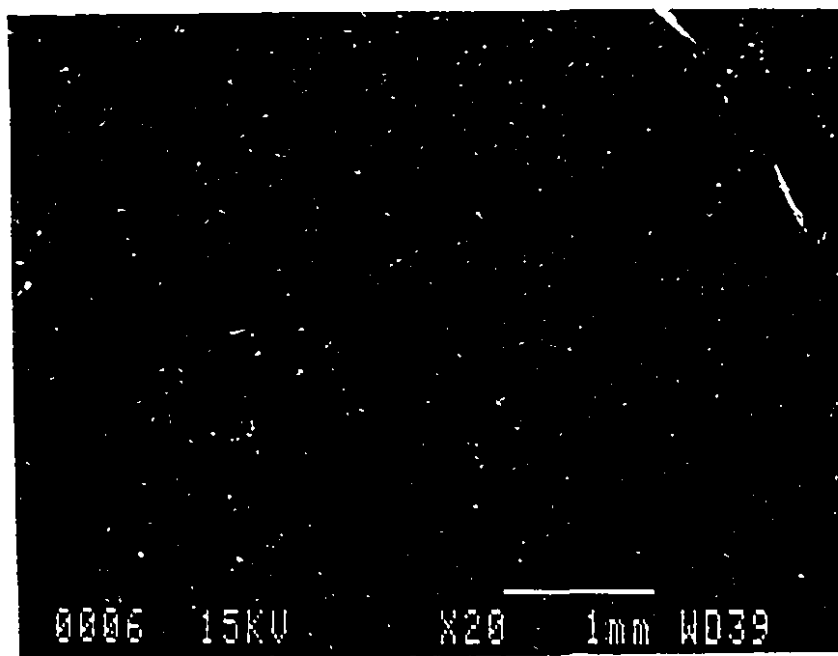


Figure 5.11 (a) - Unpolished Ti-5wt%TiC sintered at 1300°C/4 hrs ( $\times 20$ )

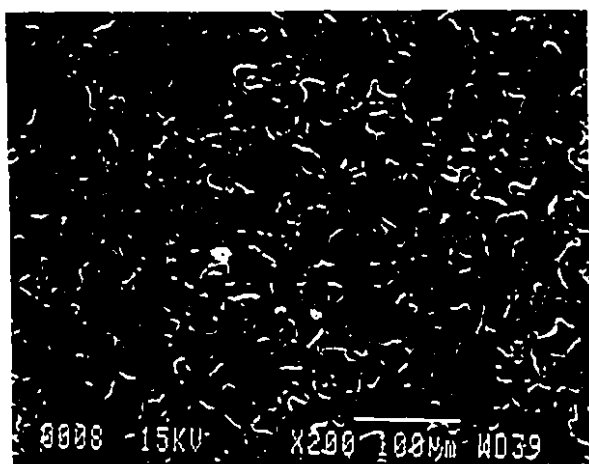


Figure 5.11 (b) - Well sintered particles in at the center of the sample ( $\times 200$ )

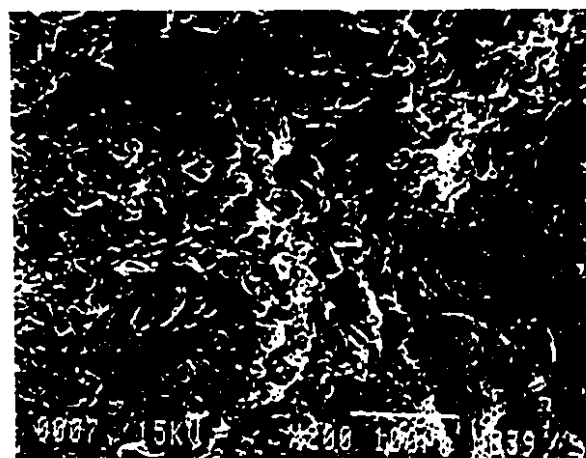


Figure 5.11 (c) - Poorly sintered structure the edge of the sample ( $\times 200$ )

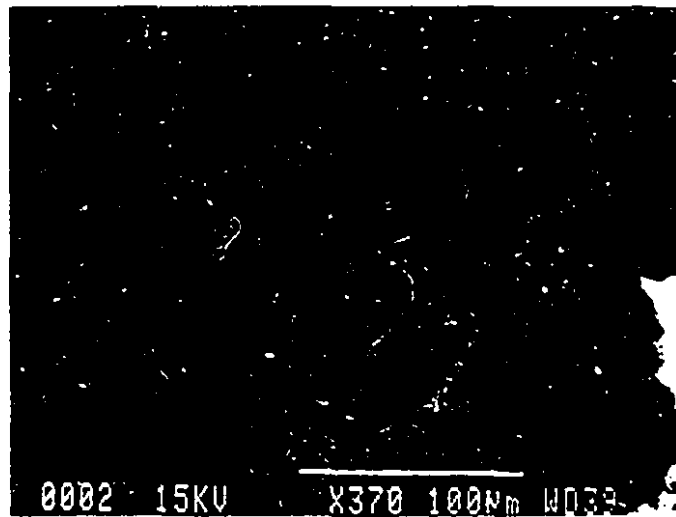


Figure 11 (d) - Ti-5wt%TiC sintered at 1300°C/4 hrs ( $\times 370$ ) showing a higher porosity of  $\sim 100 \mu\text{m}$  at the surface

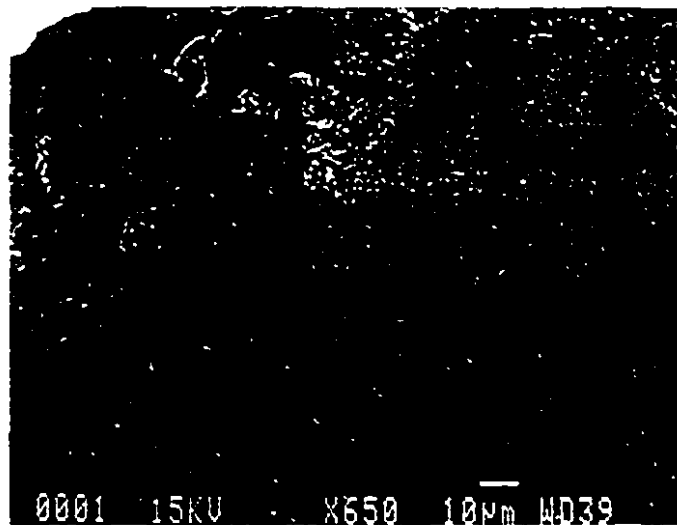


Figure 5.11 (e) - Ti-5wt%TiC sintered at 1480°C/2 hrs ( $\times 650$ ) showing a higher porosity of  $\sim 30 \mu\text{m}$  at the surface

Table 5.4 - Image analysis results for Ti-5wt%TiC composites

T (°C)	Relative density (image analysis)	Relative density (Archimedes) (%)	density difference (%)	porosity (%) <sup>1</sup>
1300				
1/2 hr	87.2	84.6	2.6	12.8
2 hrs	99.8	94.5	5.3	0.2
4 hrs	98.8	92.0	6.8	1.2
1440				
1/2 hr	90.0	88.6	1.4	10.0
2 hrs	99.4	96.1	3.3	0.6
4 hrs	99.7	93.8	5.9	0.3
1480				
1/2 hr	99.7	96.4	3.3	0.3
2 hrs	99.9	97.9	2.0	0.1
4 hrs	99.5	94.8	4.7	0.5
1600				
1/2 hr	99.9	94.1	5.8	0.1
2 hrs	99.6	92.3	7.3	0.4
4 hrs	-	82.5	-	-

### Microhardness

The sintered specimens were finally used to study the change in the microhardness of the TiC particles with increasing sintering temperature and soaking times. The microhardness was measured for each TiC content (from 2.5 to 20wt%), as well as for their respective Ti matrix (see Appendix 6), but only the graphs for 5 and 10%TiC are displayed in this section.

Figure 5.12 shows a decrease in the microhardness of the TiC particles with increasing temperatures and sintering time. Accordingly, opposite trends may be observed for the titanium matrix in Figure 5.13. Note that the decrease is greater from 1300°C to 1440°C than from 1440°C to 1600°C for sintering times of 0.5 hour and 2 hours for both

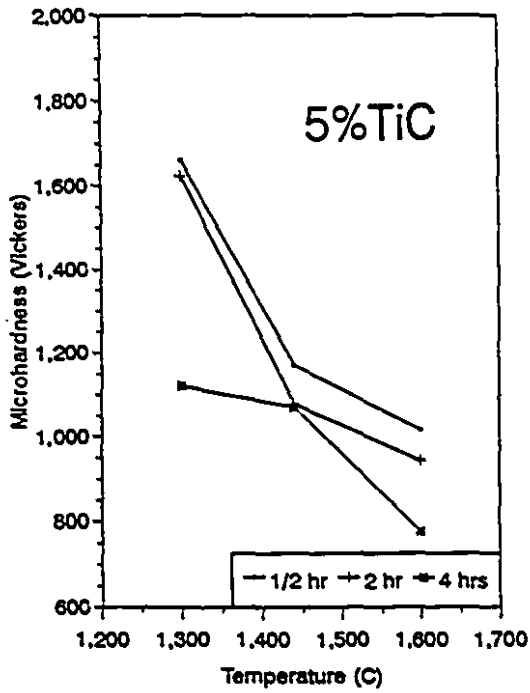
<sup>1</sup> Porosity calculated from image densities

TiC contents (Figure 5.12 (a) & (b)). The largest decrease with time is observed for 1300°C (Figures 5.12 (c) & (d)). It means that C diffusion is very rapid, and occurs at the early stage of sintering.

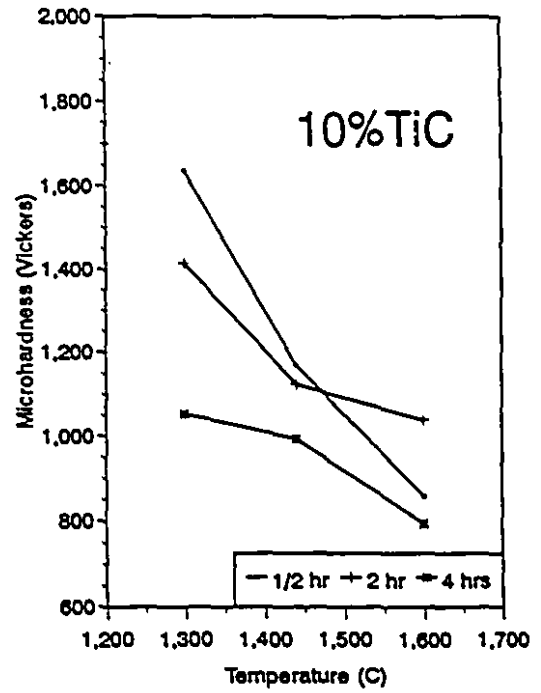
We observe that the optimum conditions for sintering correspond to a decrease in the hardness of the TiC particles. The microhardness of TiC particles at the sintering temperature of 1440°C for 2 hours decreases to 1078 HV and 1124 HV for 5%TiC and 10%TiC, respectively, compared with the as-received hardness of 1800-2600 HV before sintering (Table 2.4).

The loss of carbon explains the decrease in microhardness. The largest decrease with time is observed for 1300°C in Figure 5.12 (c) and (d). The latter can be related to Figure 5.8 where at 1300°C, density increases significantly with increasing sintering time. A potential benefit might be that the loss of C, by diffusion, favours good bonding by strengthening the ceramic/metal interface. Furthermore, the sintering temperature seems more effective than the sintering time in reducing the hardness of the TiC particles, as might be expected.

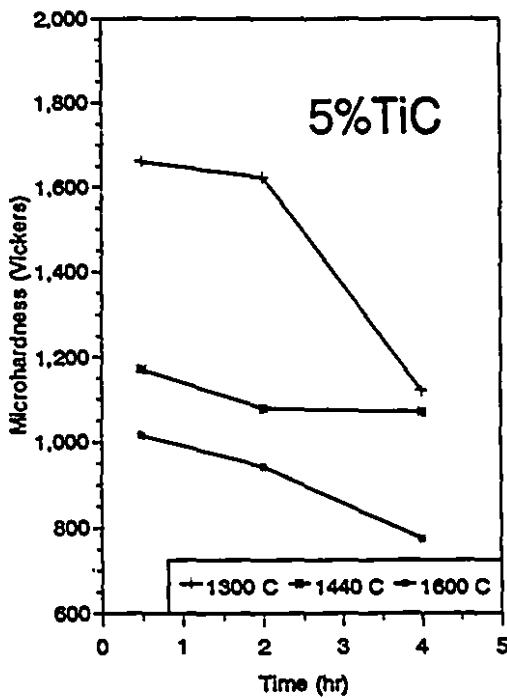
It should be mentioned that 1661 HV and 1636 HV, the TiC hardness values at 1300°C/0.5 hour, are relatively high compare to the value of 1800 to 2600 HV for the TiC starting material (Table 2.4). Figure 5.14 shows a plot of the TiC microhardness versus TiC content at 1300°C, 1440°C and 1600°C for 0.5 hour and 2 hours sintering times. No obvious trend might be extrapolated for both sintering times, though the lowest time and temperature condition exhibits an increase in microhardness with increasing TiC content. The latter may be correlated to the fact that a higher TiC content would give less diffusion of C per particle, since there is a maximum in the solubility of C in  $\alpha$ -Ti according to the phase diagram (cf. 2.7.1).



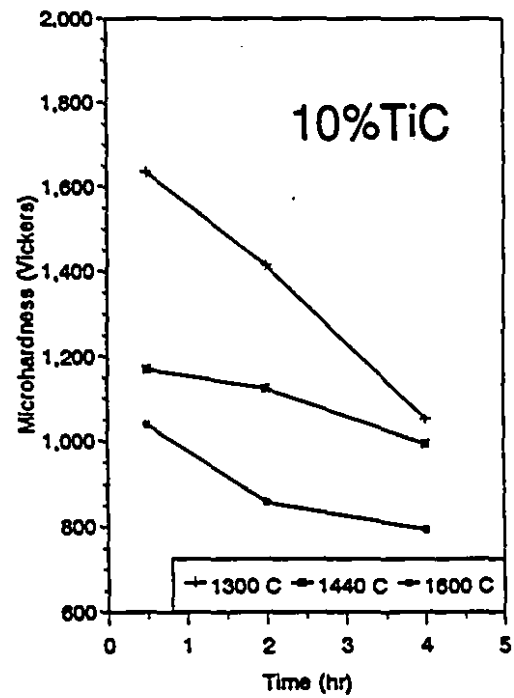
(a)



(b)



(c)



(d)

Figure 5.12 - Microhardness of TiC particles vs temperature for (a) 5%TiC and (b) 10%TiC and time for (c) 5%TiC and (d) 10%TiC

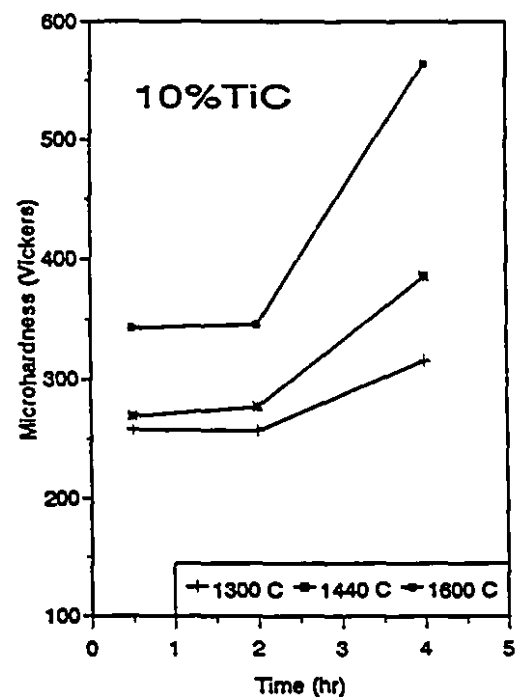
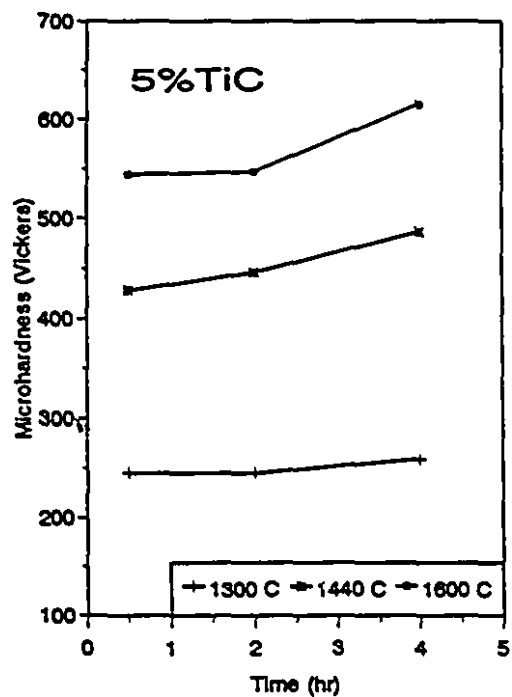
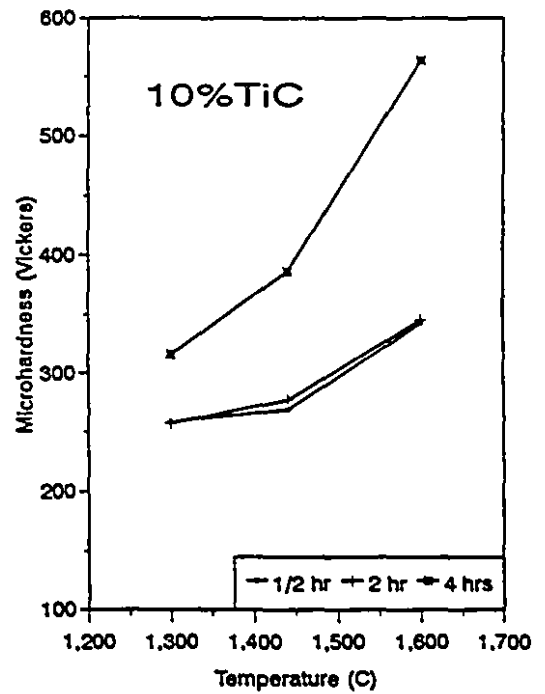
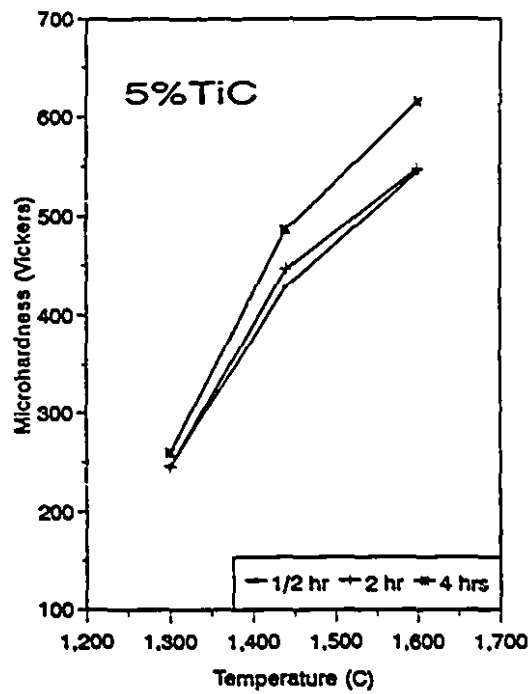
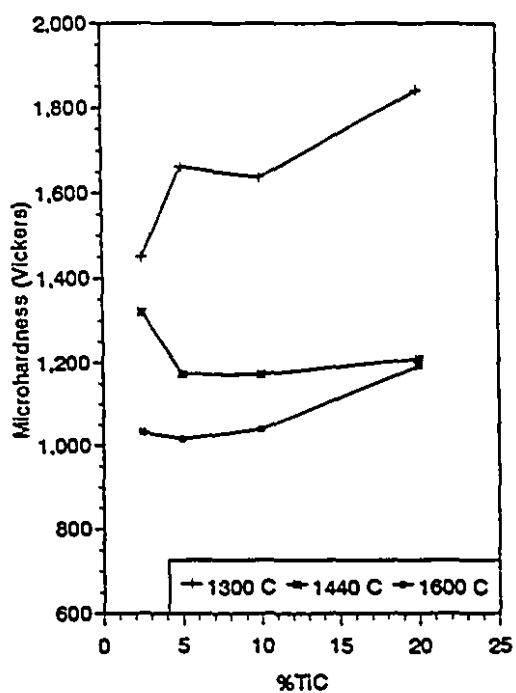
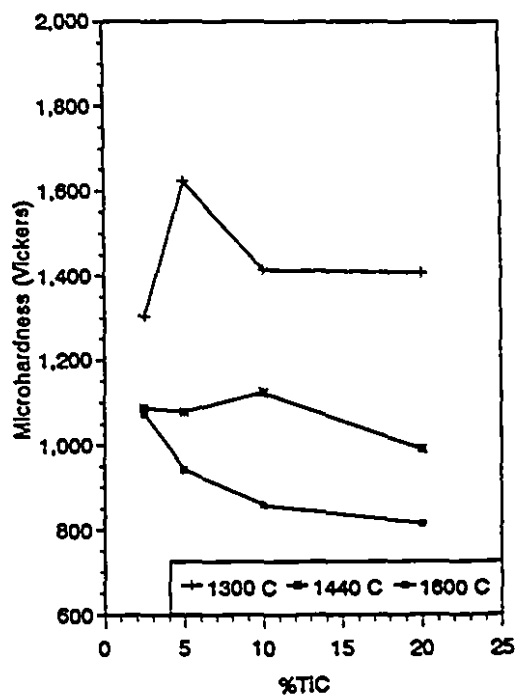


Figure 5.13 - Microhardness of Ti matrix vs temperature for (a) 5%TiC and (b) 10%TiC and time for (c) 5%TiC and (d) 10%TiC



(a)



(b)

Figure 5.14 - Microhardness vs TiC content for (a) 0.5 hour and (b) 2 hours

### Hardness measurement

The hardness of the Ti/TiC samples for each TiC content sintered at 1300°C, 1440°C and 1600°C for a sintering time of 2 hours, were measured by Rockwell testing (cf. 4.5.9).

The hardness results are summarized in Figure 5.15. It should be noted that the hardness of pure titanium (HRC 18) is increased significantly to almost 50 HRC for a sintering temperature of 1440°C by the addition of as little as 2.5% of TiC particles (Figure 5.15 (a)). The values obtained are in good agreement with the graph shown on Figure 2.5. Surprisingly, no increase of the hardness with increasing TiC content is observed. This can be related to Figure 5.9 where a 2.5-5wt%TiC content was observed to give the highest densities. The reduction in carbon concentration in TiC particles during sintering which decreases the microhardness would tend to decrease also the overall hardness. But this phenomenon competes with the fact that the diffusion of carbon, more important at higher TiC content, provides a strong bond between the TiC particles and Ti matrix which has a positive effect on mechanical properties and increases the hardness.

Figure 5.15 (b) shows a maximum in the hardness for sintering at 1480°C for each TiC content. Note again the low hardness value observed for pure titanium. Thus, the high overall hardness coincides with the fully dense materials, i.e. the optimum temperature, time and ceramic content. Consequently, one can conclude that a good hardness is associated with a strong interfacial bond between the particle and the matrix.

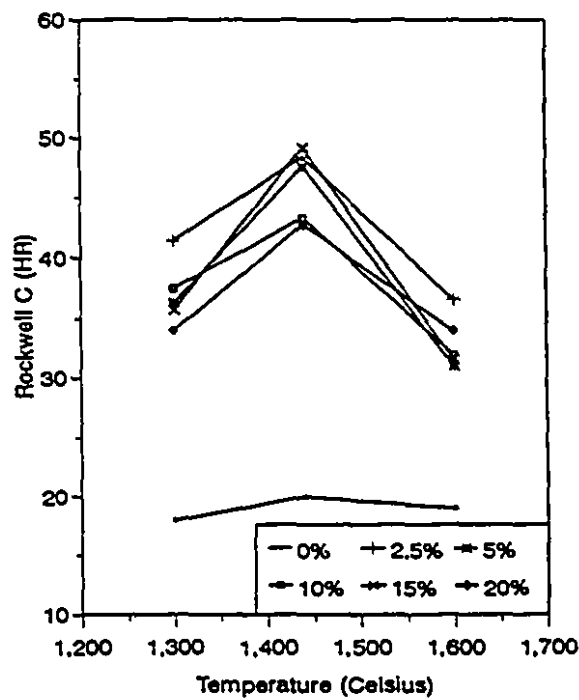
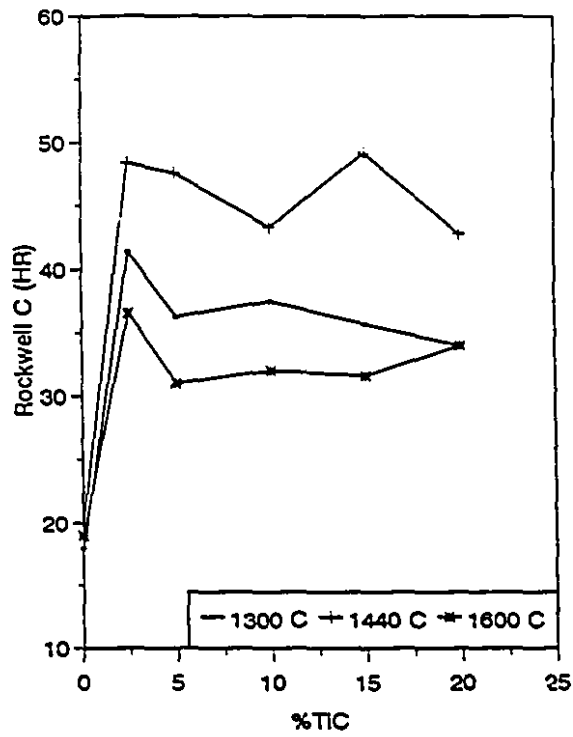


Figure 5.15 - (a) Hardness vs TiC content (t=2 hrs)  
 (b) Hardness vs sintering temperature (t=2 hrs)

### 5.3 MICROSTRUCTURE

A selection of micrographs of Ti-10wt%TiC sintered and polished samples are presented in Figure 5.16 for 0.5 and 4 hours of sintering at 1300°C, 1440°C, and 1600°C along with their relative densities in parentheses.

In spite of the attrition milling, some agglomeration may be seen in some of them. It is attributed to the fact that some particles were trapped and packed in regions of the mill where they did not receive adequate milling. This is confirmed when looking at the 1300°C/0.5 hour sample, where agglomeration is quite clear on Figure 5.16 (a). A higher magnification of the TiC agglomerate is shown on Figure 5.17. However, after 4 hours at 1300°C of sintering, a dense microstructure is obtained as shown on Figure 5.16 (b), but TiC agglomerates of a similar size are still quite evident. This agglomeration is surely associated with a high TiC content since this phenomenon was not observed at low TiC content as shown in Figure 5.18 for 2.5%TiC and the same sintering conditions. Indeed, note the smaller particle size.

At 4 hours and 1440°C (Figure 5.16 (d)) exhibits less agglomeration than 1300°C. It is further confirmed by image analysis which gives a mean TiC particles size of 14.4  $\mu\text{m}$  for 1440°C compare to 22.9  $\mu\text{m}$  for 1300°C (Table 5.5). Since particle growth is exponentially dependent on temperature as it is a diffusion process (equation 2.11), it would follow from the figures given above that no particle growth is observed for these sintering conditions.

However, from 1440°C/0.5 hour (Figure 5.16 (c)) to 1440°C/4 hours (Figure 5.16 (d)), there is a definite particle growth confirmed by a mean TiC particle size of 14.7  $\mu\text{m}$  and 24.4  $\mu\text{m}$ , respectively.

Low density results at 1300°C and short times are the consequence of an early stage of sintering as shown on Figure 5.19 where neck formation is observed. Equation 2.9 shows the dependence of neck growth with both temperature and time. It is worth mentioning that neck growth does not imply any decrease in the amount of porosity, as explained in Chapter 2.11 and results in very little densification (81.0%).

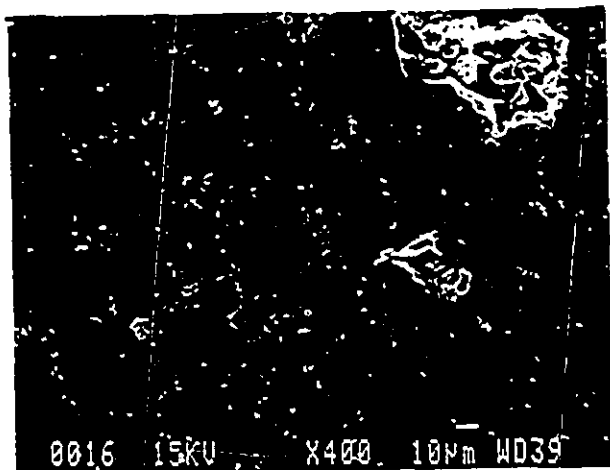


Figure 5.16 (a) - Ti-TiC 10wt% (82%)  
1300°C/ 0.5 hr ( $\times 400$ )

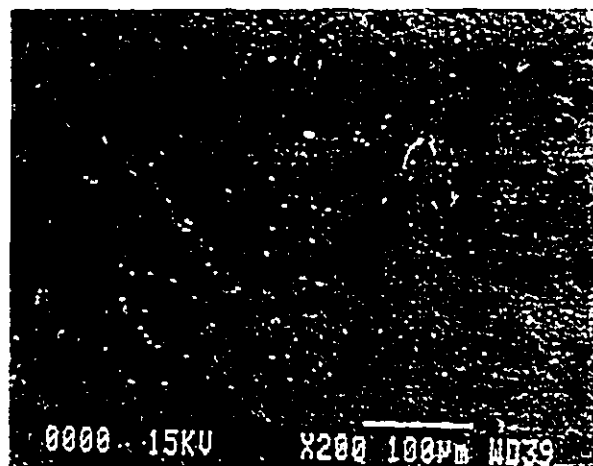


Figure 5.16 (b) - Ti-TiC 10wt% (93.6%)  
1300°C/ 4 hrs ( $\times 200$ )

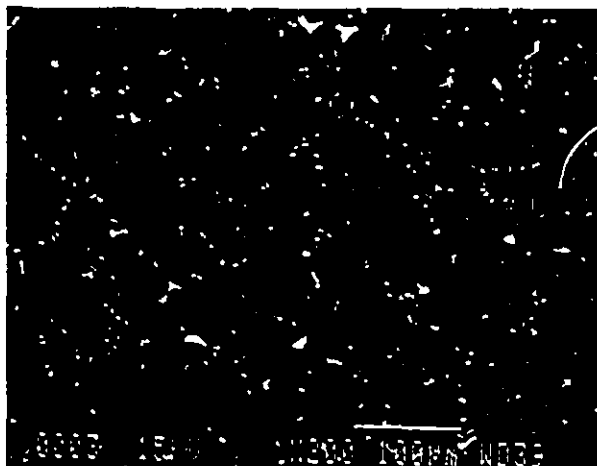


Figure 5.16 (c) - Ti-TiC 10wt% (83.7%)  
1440°C/ 0.5 hr ( $\times 200$ )



Figure 5.16 (d) - Ti-TiC 20wt% (93.5%)  
1440°C/ 4 hrs ( $\times 200$ )

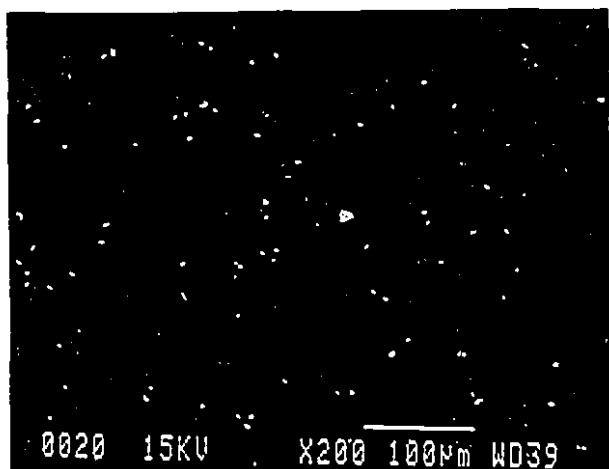


Figure 5.16 (e) - Ti-TiC 10wt% (93.2%)  
1600°C/ 0.5 hr (× 400)

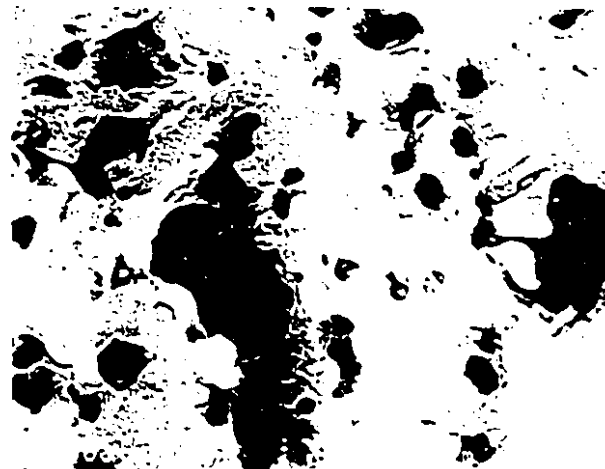


Figure 5.16 (f) - Ti-TiC 10wt% (81.7%)  
1600°C/ 4 hrs (× 200)



Figure 5.17 - Agglomerates of TiC in a Ti-10wt%TiC sintered at 1300°C/0.5 hr (× 2,000)

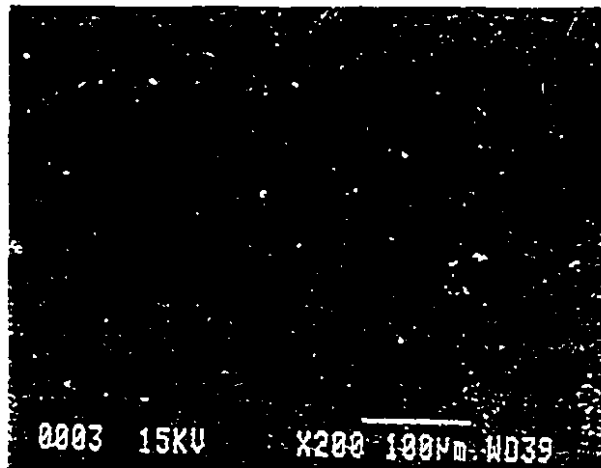


Figure 5.18 - Ti-2.5wt%TiC sintered for 1300°C/4 hrs (99.4%) (× 200)



Figure 5.19 - Ti-2.5wt%TiC sintered for 1300°C/0.5 hr (81%) (× 3,000)  
Neck formation between particles of Ti

At 1600°C/0.5 hour (Figure 5.16 (e)), a good microstructure can be seen with TiC agglomerates of similar size as that observed at 1300°C/0.5 hour (Figure 5.16 (a)). Then, a drastic change in the microstructure occurs for 1600°C/4 hours as observed on Figure 5.16 (f). A desintering process, already detected in terms of relative density in Figure 5.7 and 5.8 generated large pores of approximately 50-100  $\mu\text{m}$  giving a final porosity of 18.3%. This phenomenon may be related to a pore coarsening effect at a first stage, and to some chemical decomposition reactions at a second stage. Figure 5.16 (f) does not show any melted zone which is in agreement with the fact that 1600°C is below the Ti melting point of 1668°C (cf. 2.7.1). Thus, pore coarsening may be related to the so called Ostwald Ripening process<sup>67</sup>. At a final stage, spherical pores are expected after grain boundary breakaway. Then, the pore must diffuse vacancies to distant grain boundaries to continue shrinking, a slow process. Suppose two spherical pores of respective radius  $R_1$  and  $R_2$  with  $R_1 > R_2$  (Figure 5.20). Around each pore exists a different concentration due to an oversaturation of vacancies (because of a concave surface) which can be calculated from Thomson-Freundlich equation (equation (11) in Appendix 1) with  $R_1 = R_2 = R$  :

$$\Delta C = C_0 \frac{2\gamma\Omega}{kTR} \quad 5.1$$

This results in a vacancy gradient from the exterior of the smaller pore towards the largest pore because the concentrations are inversely proportional to their respective radii of curvature. This effect will reduce the radius of the smallest particle ( $R_2$ ). Consequently, the large pore will get coarser at the expense of the smaller which is relatively unstable. Thus, pore coarsening causes the mean pore size to increase while the number of pores will decrease. It is important to note that pore coarsening already starts at a rather early stage of sintering, i.e. 1300°C/0.5 hour, since a mean pore size diameter of 9.4  $\mu\text{m}$  was computed (Table 5.5) while the mean pore size was only about 3  $\mu\text{m}$  for the green compacts (Figure 5.5). Then, prolonged sintering causes desintering ensuing a decrease in density (cf. Figure 5.7 and 5.8) which must be due to a decomposition reaction process, favored by the combination of coalesced pores, at very high temperature and the very high reactivity of

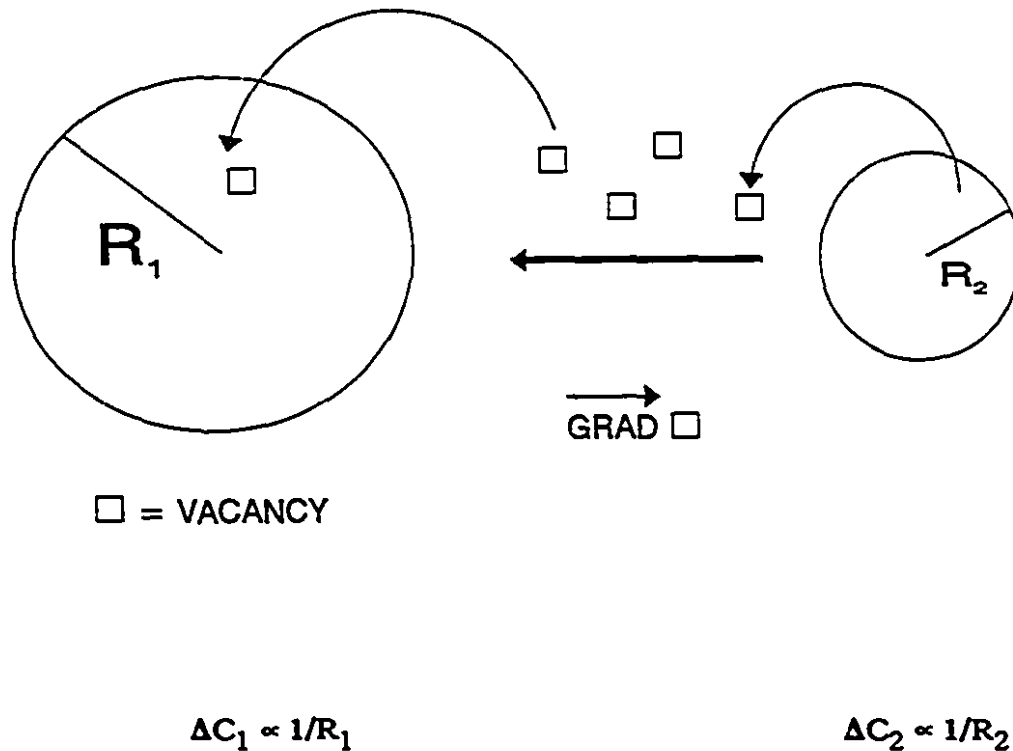


Figure 5.20 - The pore coarsening effect

Ti (cf. 2.9.1). For instance, the presence of some water would immediately give formation of non-stoichiometric  $TiH_x$  ( $x < 2$ ) by absorption of  $H_2$ . Furthermore, decomposition of TiC is also expected through reaction with  $O_2$  to release CO gas.

It can be concluded that, for temperatures near the melting point, superior sintering is achieved for a short sintering time (i.e. 0.5 hour). The microstructural observations are in good agreement with the density curves discussed in the previous section on sintering studies.

#### Porosity and particle size

With reference to the micrographs, one can observe that the pores are generally located in and around the particles. Figure 5.21 shows clearer evidence of the latter and it was found, by image analysis, that around 80% of the pores were entrapped within the

TiC particles.

The mean size of TiC particles in the sintered alloys as well as their pore size were measured using image analysis. The average size of TiC particles and pores are listed in Table 5.5. Histograms of both TiC particles and pores size are plotted on Figure 5.22 as a function of the sintering temperature for three different sintering times. Table 5.5 gives diameters of particles and pores for a 10wt%TiC specimen at 1300°C, 1440°C, 1480°C, and 1600°C for sintering times of 0.5 hour, 2 hours, and 4 hours. It also gives the densities calculated by image analysis along with the level of porosity.

For low temperatures, pore diameter decreases with increasing time. No change was

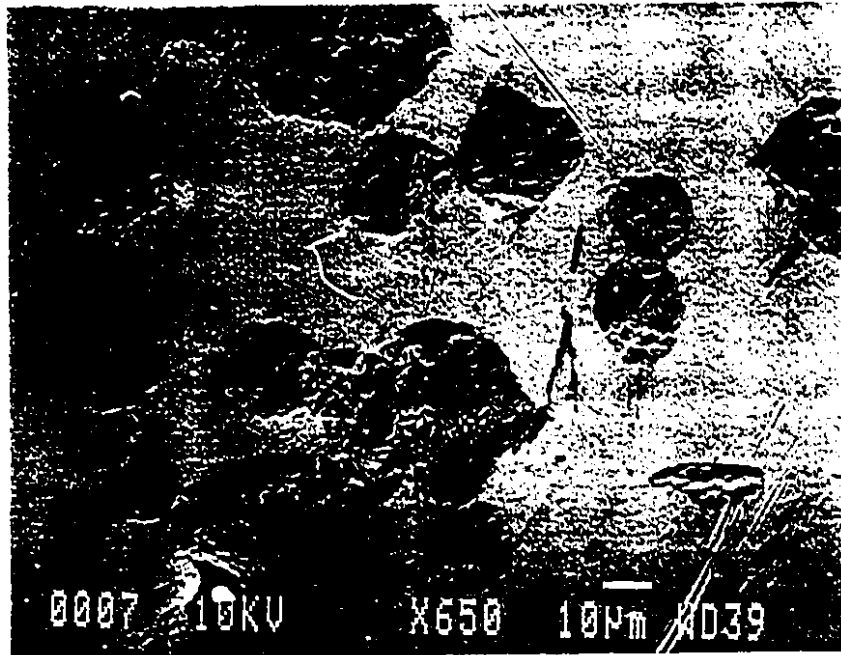


**Figure 5.21 - Ti-10wt%TiC sintered at 1600°C/0.5 hour ( $\times 650$ )**  
noticed at 1480°C. Finally, a dramatic increase was seen at 1600°C, especially for 4 hours. These remarks are in good agreement with the trends observed on Figure 5.7 and Figure

5.8, especially for sintering at 1600°C. The smallest pore size appeared to be at 1480°C, which corroborates the statement that this temperature would give the best densities.

No overall evident particle growth may be observed regarding the sintering temperature in Figure 5.22 (a). Discussing in detail the different trends related to particle size is not really meaningful since the scatter recorded for particle diameters is as high as the absolute values themselves. This large scatter may partly be due to agglomeration which alters, and somehow slightly overestimates the values, and might also be attributed to the relatively large particle size distribution of the original TiC. Effectively, the TiC starting powder ranges from 1 to 27  $\mu\text{m}$  with a mean value of 12  $\mu\text{m}$  (cf. 5.1). Nevertheless, some growth of the TiC particles can be observed with increasing temperature. At 1300°C

Table 5.5 - Particle size and pore sizes results for Ti-5wt%TiC composites

T (°C)	D (TiC) <sup>1</sup> ( $\mu\text{m}$ )	D pores ( $\mu\text{m}$ )
1300		
1/2 hr	13.3 ± 12.4	9.4 ± 9.9
2 hrs	15.9 ± 16.5	6.0 ± 3.4
4 hrs	22.9 ± 22.8	1.7 ± 1.8
1440		
1/2 hr	14.7 ± 15.4	12.3 ± 10.1
2 hrs	21.7 ± 19.8	6.0 ± 3.7
4 hrs	24.4 ± 20.3	5.5 ± 5.1
1480		
1/2 hr	17.8 ± 14.4	too small
2 hrs	24.8 ± 17.4	too small
4 hrs	20.9 ± 21.8	too small
1600		
1/2 hr	22.5 ± 20.1	6.3 ± 3.8
2 hrs	20.1 ± 16.0	3.6 ± 1.7
4 hrs	non measurable	23.2 ± 30.7

<sup>1</sup> 5wt%TiC

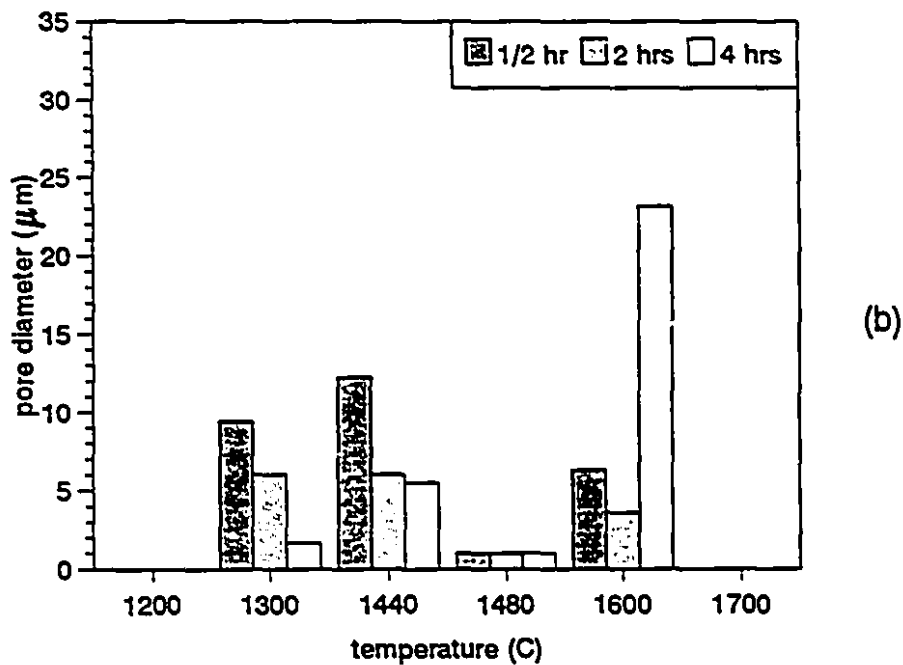
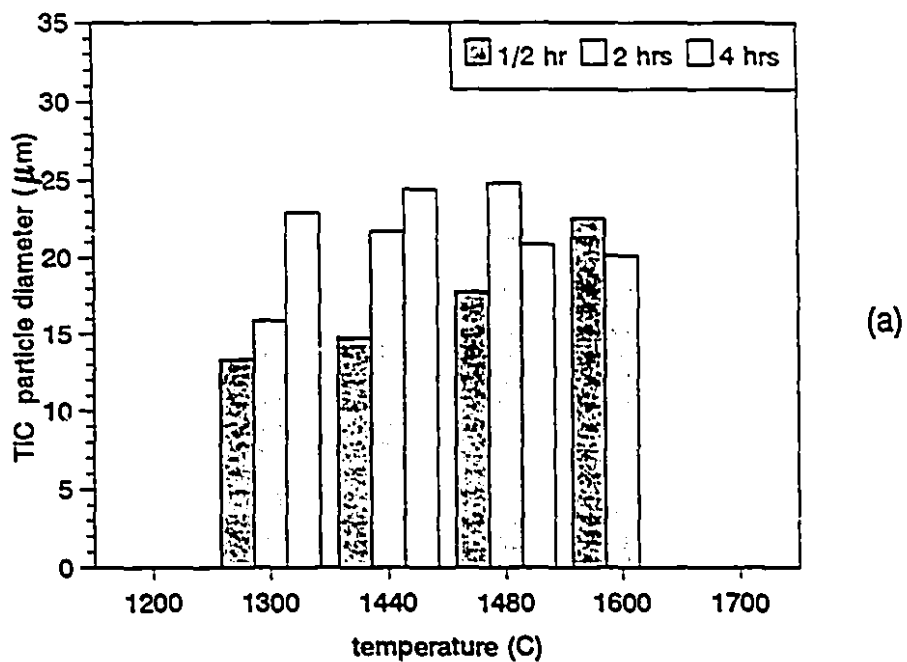


Figure 5.22 - (a) TiC particle size vs temperature  
(b) Pore diameter vs temperature

and 1440°C, TiC particles have a mean diameter of 13.3  $\mu\text{m}$  and 14.7  $\mu\text{m}$  which increases with increasing sintering time up to 22.9  $\mu\text{m}$  and 24.4  $\mu\text{m}$  for 4 hours, respectively. Note that the increase in particle size is quite clear for 0.5 hour sintering and 2 hours sintering with increasing temperature.

Sintering at 1480°C shows up a maximum particle diameter for a time of 2 hours. However at 1600°C, not significant trend is evident and, unfortunately, measurement for 4 hours was not possible considering the high level of porosity (Figure 5.16 (f)).

It can thus be stated that a concomitant TiC particle growth and aggregation occurs during the sintering of these composites for the range of temperature and time studied. Xia and Deng noted a significant TiC particle growth in Ti-10wt%TiC alloy with an average size of 4.5  $\mu\text{m}$  at 1000°C up to 16.3  $\mu\text{m}$  at 1500°C. However, they used much finer starting powders (average size of 9.7  $\mu\text{m}$  for Ti and 2.7  $\mu\text{m}$  for TiC) and a much wider temperature range of 850-1500°C.

#### 5.4 MICROPROBE ANALYSIS AND CARBON DIFFUSION

The analysis of the results show that the TiC particles enlarge and aggregate compare to the original values and that the microhardness of these particles decreases with sintering temperature and time. Moreover, the results showed an improvement in the sinterability of the composite by addition of TiC. The sintered density of the Ti-TiC composites was seen to improve compare with that of the pure Ti under the same conditions and that this amelioration was related to the role of carbon.

In order to investigate the phenomena related to the sinterability of the Ti-TiC, electron microprobe analysis (cf. 4.5.8) of C and Ti in the matrix as well as in the carbide particles was performed on 5wt%TiC samples. For this study, the three following sintering conditions of 1300°C for 4 hours, 1440°C for 2 hours, and 1600°C for 0.5 hour were selected. The data are presented in Table 5.6 along with a micrograph showing the three typical point sources for the EPMA analysis in Figure 5.23. Calculation of  $x$  is given by :

$$x = \frac{\%C}{100 - \%C} \quad 5.2$$

where %C is the atomic percent of carbon. An average 12wt% or 35at% of C was found after sintering for the three samples. According to the phase diagram shown in Figure 5.24, these values are still within the TiC composition range for the sintering temperatures considered.

Diffusion of carbon out of the TiC and/or Ti diffusion into TiC is confirmed by the relatively large loss of C for all the samples analyzed. This loss was calculated to be approximately 7.6% by weight compare to the original 19.66wt%C (cf. Table 4.2). In addition, no C enriched TiC was detected on the edge of the particle. The absence of a TiC annulus inside the particle was further confirmed by X-ray mapping. Figure 5.25 and 5.26 show an example at 1440°C for 4 hours. Panchal and Vela<sup>61</sup> observed such an annulus

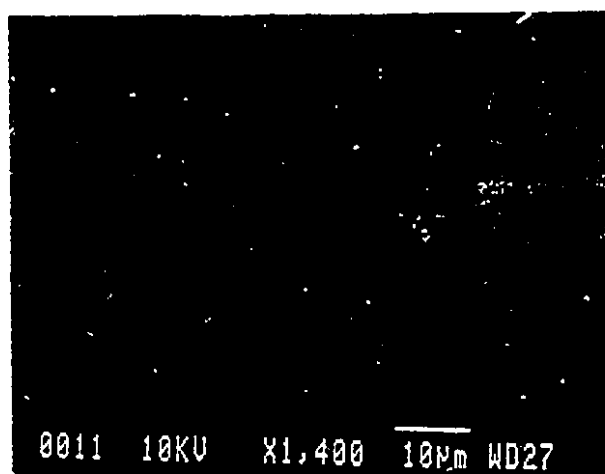


Figure 5.23 - 5wt% TiC/1440°C/4 hours showing the position of microprobe analysis in Table 5.6

Table 5.6 - EPMA analysis of Ti content

Sintering Conditions	Locations in Figures	Ti Weight %	C		
			Weight %	Atomic %	x
1300°C 5% TiC 4 hrs	A	87.3	12.7 ± 2.0	36.7	0.58 ±
	B	97.6	2.4 ± 2.0	8.9	0.01
	C	97.8	2.2 ± 2.0	8.2	
1440°C 5% TiC 2 hrs	A	88.1	11.9 ± 2.0	35.0	0.54 ±
	B	98.1	1.9 ± 2.0	7.2	0.01
	C	98.3	1.7 ± 2.0	6.5	
1600°C 5% TiC 0.5 hr	A	88.4	11.6 ± 2.0	34.4	0.52 ±
	B	95.7	4.3 ± 2.0	15.2	0.01
	C	97.4	2.6 ± 2.0	9.6	

but at an earlier stage of sintering (i.e. 1200°C for 1.5 hours). Note that the contrast in colour pixels between the particle and the matrix, for the carbon X-ray mapping, is not strong in spite of the large difference in C content (12wt% in TiC and almost zero in the matrix). This is due to the fact that C element is a very low atomic number ( $Z = 6$ ) and is at the very limit of detection and therefore the number of counts to background ratio is quite small thereby producing a poorer contrast in the SEM/X-ray image.

From this discussion, one can assume that the interdiffusion of C and Ti plays a crucial role in Ti-TiC metal matrix composites. This can be explained by the fact that C diffuses in the Ti matrix nearly five orders of magnitude faster than Ti with an activation energy of only 58.6 kJ/mole compare to 151 kJ/mole for Ti<sup>84-85</sup>. Therefore, carbon diffusion out of the TiC particulates into the Ti matrix is the most important mechanism. Carbon diffusion during sintering is also responsible for the small TiC particle growth observed. Carbon diffusion out of TiC may also explain the slightly higher at.%C observed at 1600°C in the matrix around the particle (location B) than further away at location C (Table 5.6).

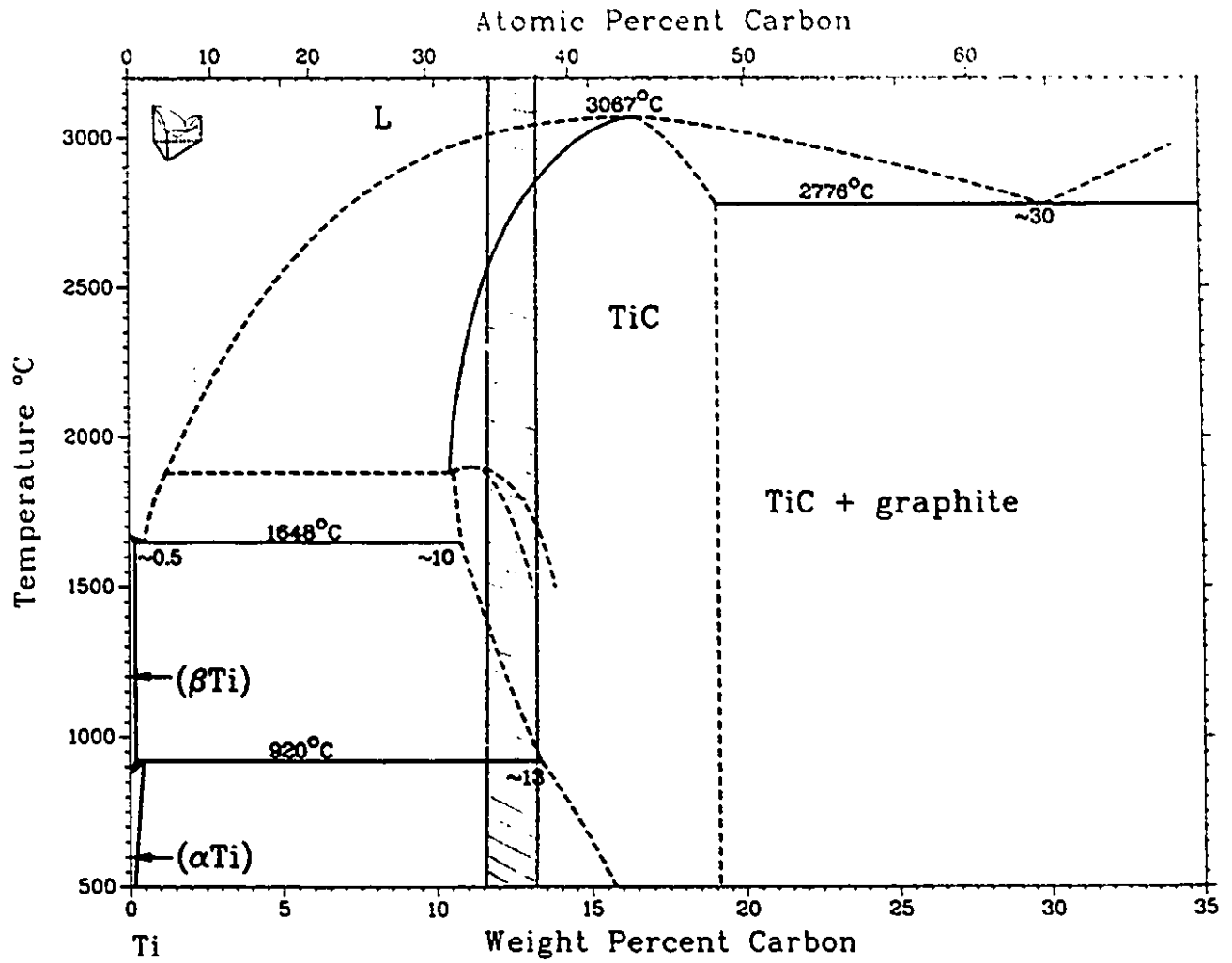
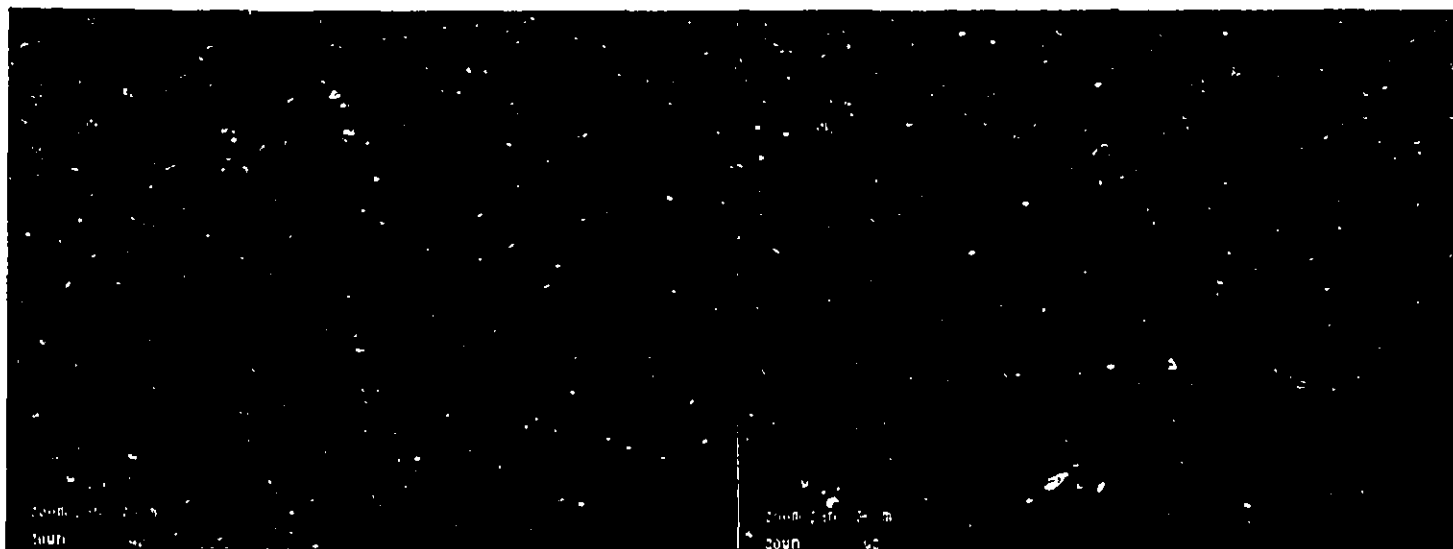
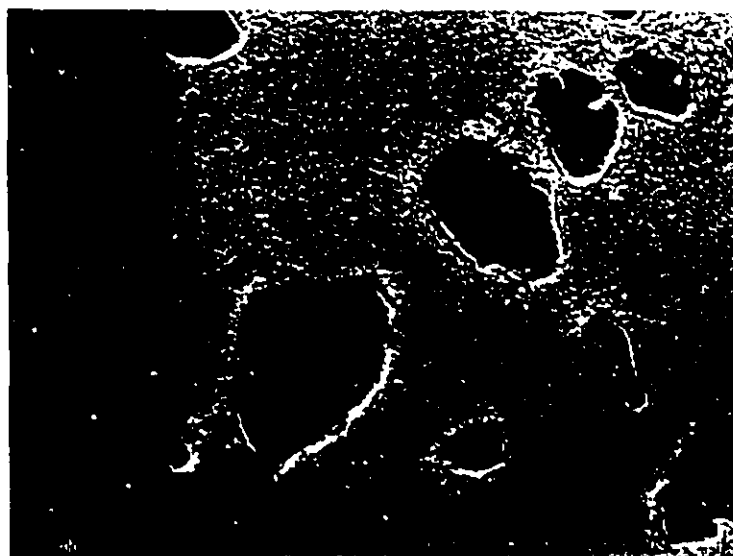


Figure 5.24 - Ti-TiC phase diagram



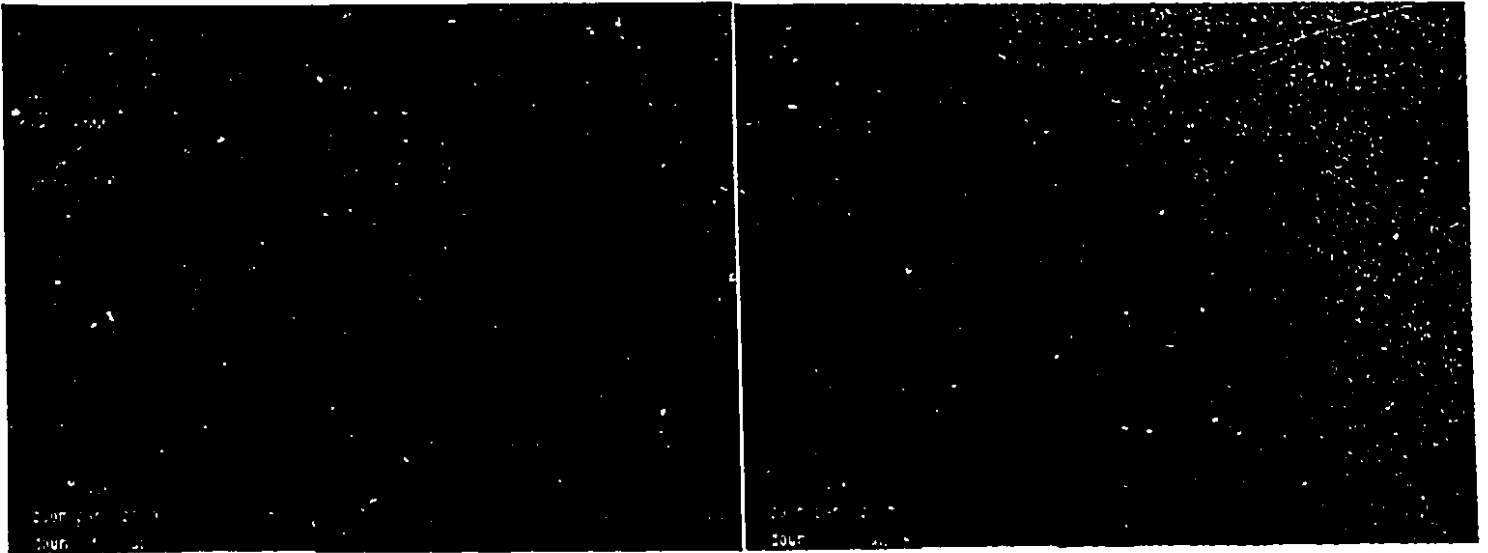
CARBON

TITANIUM



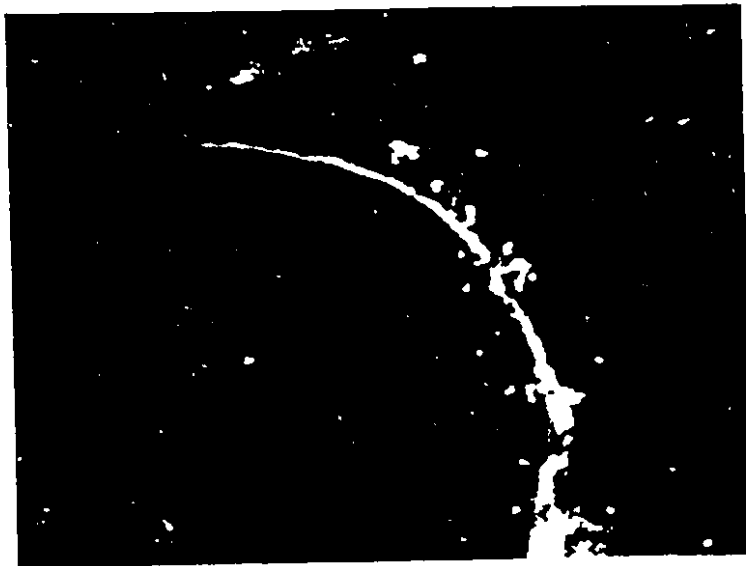
ORIGINAL MICROGRAPH

Figure 5.25 - SEM X-ray mapping of Ti-5wt%TiC, 1440 °C, 2 hours, 10kV ( $\times 600$ )



CARBON

TITANIUM



ORIGINAL MICROGRAPH

Figure 5.26 - SEM X-ray mapping of Ti-5wt%TiC, 1440 °C, 2 hours, 10kV ( $\times 3,000$ )

Tokar *et al.*<sup>67</sup> suggests that metal and carbon atoms may diffuse along the grain boundaries of TiC with an activation energy of 260 kJ/mole. However, this latter value is more than four times that of C diffusion in Ti matrix.

Moreover, combining the microprobe and X-ray mapping results, it is concluded that diffusion of C out of the carbide particles is very rapid and does not form a shell of substoichiometric carbide ( $\text{TiC}_x$ ) around the original carbide particles, for the range of sintering time and temperature considered. Panchal and Vela<sup>65</sup> noticed the disappearance of the shell with an increase of the sintering temperature from 1200°C to 1380°C for a sintering time of 1.5 hours. Their results are in good agreement with the fact that no substoichiometric TiC annulus was found even at the lowest temperature studied here (1300°C).

Furthermore, the porosimetry study as well as the green density results (Table 5.3) show that the addition of the ceramic particulates did not improve the green density because of the very similar particle size distribution recorded for both Ti and TiC (Figure 5.5). The sinterability improvement observed is not due to a higher green density in the starting compacts. Hence, another phenomenon occurs and aids the composite to sinter better and, consequently, get a higher final density of a few percent, significant when approaching densities over 90%.

Consequently, it is assumed that the sinterability of the Ti-TiC composite is improved by the carbon diffusion in TiC in the Ti matrix. This was confirmed by the loss of C studied with the electron microprobe which further proved that this loss led to the conversion of the stoichiometric TiC into non-stoichiometric  $\text{TiC}_x$  ( $x < 1$ ).

After sintering, a diffusion profile like the one displayed on Figure 5.27 can be drawn from EPMA results (Table 5.6). The TiC particles react with the Ti in the matrix to form substoichiometric TiC by "feeding" the matrix with C. This results in the formation of  $\text{TiC}_x$  ( $x < 1$ ) more and more deficient in carbon, which consequently leads to a decrease in microhardness. The next section will try to correlate microhardness with C loss.

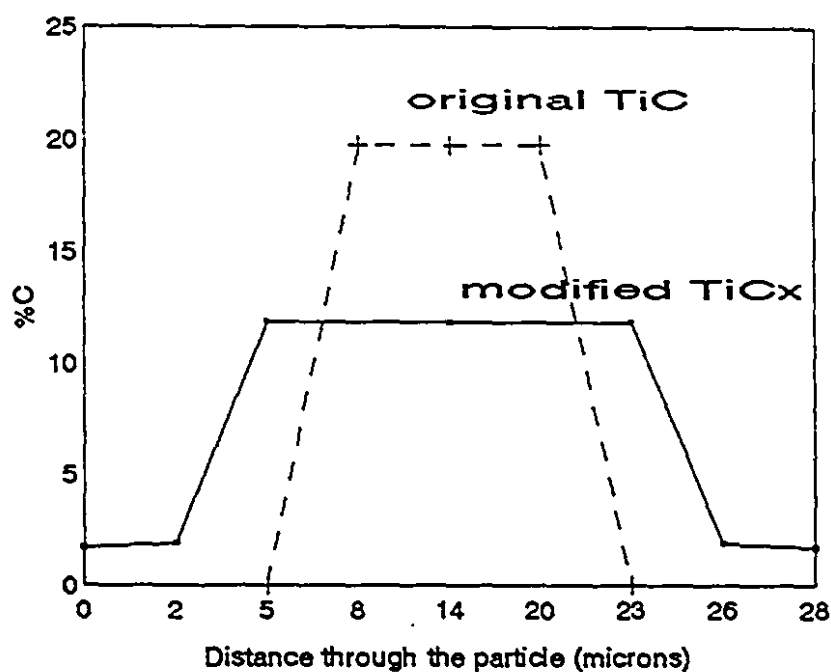


Figure 5.27 - Carbon diffusion profile

#### Correlation of microhardness with carbon loss

According to the formula established by Vilk<sup>68</sup>, the microhardness (HM) is linearly proportional to the stoichiometry ( $x$ ) of the TiC particles and follows the equation :

$$HM = ax - b \quad 5.3$$

where  $x$  is the atomic ratio of C/Ti and HM is the microhardness of TiC <sub>$x$</sub>  in kg/mm<sup>2</sup>.

A hardness of 200-400 HV was found for the pure Ti matrix and the manufacturer's value for the pure TiC is 1800-2600 HV (Table 2.4). Therefore, we end up with the following empirical equation :

$$x = \frac{HM + 300}{2500}$$

5.4

Figure 5.28 is a plot of the microhardness versus the C/Ti ratio calculated using equation 5.3 and the C/Ti ratio calculated from the microprobe results (Table 5.6). These data are compiled in Table 5.7.

Table 5.7 - Atomic ratio C/Ti from EPMA and calculated from equation 5.4

T (°C) \ t	Microprobe	Vilk
1300/4 hrs	0.58 ± 0.01	0.57 ± 0.05
1440/2 hrs	0.54 ± 0.01	0.55 ± 0.01
1600/0.5 hr	0.53 ± 0.01	0.53 ± 0.02

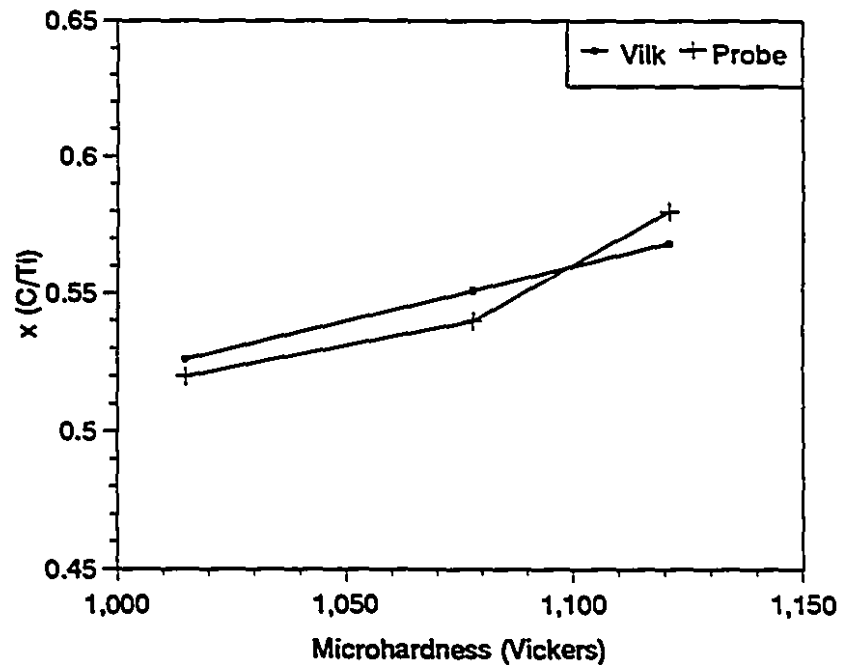


Figure 5.28 - Microhardness vs C/Ti ratio

The calculated results are consistent with those determined by electron microprobe analysis. Consequently, it confirms that carbon (C) diffuses from the TiC into the Ti matrix which leads to the loss of C from the TiC and, in turn, to a decline of its microhardness. Note that these C/Ti atomic ratio are well within the TiC composition range according to the phase diagram of Figure 2.1 (b).

On the other hand, the overall hardness of the composite is significantly increased by the addition of hard particles of TiC which are strongly bonded to the fully dense Ti matrix. Therefore, though the microhardness of the TiC particles is decreased significantly during sintering, these composites have almost three times higher hardness than commercially pure Ti.

Referring back to Table 5.6, 11.6wt% to 12.7wt% of C is in agreement with the Ti-TiC phase diagram (Figure 5.24). Therefore, the composition of the TiC has been shifted to the left. This value lies between the values given for the  $\text{TiC}_x$  solvus of 10-13 shown on Figure 5.24. In terms of solubility, if a loss of 7.6%C is considered for a 5%TiC sample, then it gives a 0.38%C dissolved in the Ti matrix. According to most Ti-C diagrams, a maximum solubility of 0.5% has been reported (cf. 2.7.1). Therefore the amount of C which has diffused into the matrix is in agreement with the maximum C solid solubility found in the literature.

According to the phase diagram, at thermodynamic equilibrium, if the Ti matrix were saturated in C by the addition of free carbon, there would be no driving force for C diffusion out of the TiC. Therefore a stoichiometric TiC ( $x=1$ ) could be retained along with its high hardness. On the other hand, diffusion of C provides good bonding and seemed to aid the densification of the material. A weaker interface between Ti and TiC might be expected to cause a deterioration in the mechanical properties. The addition of carbon might enable a tailoring of the interface and, indeed, the mechanical properties of Ti-TiC MMCs. Such an approach is worthy of further exploration.

In summary, the addition of less than 10wt%TiC with some free carbon was seen to enhance the sinterability of Ti, making it possible to attain densities as high as 99%+ of theoretical density. Results show that the best conditions for the optimum density are attained for 2.5 to 5wt%TiC at a temperature of 1440°C-1480°C for 2 hours, with a corresponding hardness of nearly 50 HRC. Finally, a decrease in the microhardness of TiC with increasing temperature and time has been observed.

There is good bonding between the matrix and TiC with no obvious reaction zone extending into the matrix. The generation of non-stoichiometric TiC, analysed by microprobe and X-ray imaging, is evidence that there has been a considerable diffusion of C between the TiC particles and the matrix. C is the faster diffusing species and, as a result, C was seen to diffuse extensively into the Ti matrix from the TiC. As a result, the C content was seen to decrease in the original carbide particles. A loss of 7-8wt% led to a substoichiometric  $TiC_x$  ( $0.53 < x < 0.58$ ) containing about 12wt% of C. These results are in agreement with the phase assemblage expected according to phase diagrams currently available.

From the above, it follows that the decrease in the C concentration leads to the decline of the hardness of the TiC particulates. This event was further confirmed by the fact that the microhardness is linearly proportional to the C/Ti atomic ratio ( $x$ ). These phenomena result from the rapid diffusion of C during sintering. The diffusion of C in the matrix seems to be the major driving force. Moreover, the gain in relative density for 2.5-5wt%TiC was not due to higher green densities in the starting compacts. Therefore, it is concluded that the sinterability of these composites is improved due to C diffusion.

# Chapter 6

## Conclusions and Recommendations

### 6.1 CONCLUSIONS

This Chapter will highlight the overall conclusions that may be drawn from the results of this thesis. It will show that the work performed fulfilled the objectives presented in Chapter 3. Finally, recommendations for future work will be outlined.

1. Attrition milling of the starting powder was found to significantly enhance the sintered density. This was explained by the removal of the  $\text{TiO}_2$  layer which somehow inhibits better sintering.
2. Good sintering was achieved along with good TiC particle dispersion throughout the Ti matrix although some agglomeration was observed.
3. A decomposition reaction was found to occur at a sintering temperature of  $1600^\circ\text{C}$  for a sintering time of 4 hours causing desintering which led to a significant decrease the density.
4. Results show that the best combination for density was obtained for 2.5 to 5wt%TiC at a temperature of  $1440\text{-}1480^\circ\text{C}$  for two hours.
5. The addition of less than 10wt%TiC enhances the sinterability making it possible to attain 99%+ of theoretical density.
6. The TiC particles enlarge and aggregate and the hardness of these particles

decreases when the sintering temperature and time are raised.

7. These phenomena result from the rapid diffusion of C during sintering and the sinterability of these composites is improved due to the C diffusion.

8. Furthermore, diffusion of C out of the carbide particles decreases the C content in the original carbide particles. This loss was found to be 7-8wt% which corresponds to a substoichiometric  $TiC_x$  ( $0.53 < 0.58$ ) of about 12wt% of C.

9. The decrease of the C concentration in the TiC leads to the decline of its hardness.

10. The overall hardness is significantly improved to 50 HRC compared to that of pure commercial Ti (18 HRC) for material sintered under optimum conditions of 1480°C for 2 hours.

## 6.2 RECOMMENDATIONS FOR FURTHER WORK

On this particular Ti-TiC metal matrix composite, extensive work remains to be done on the mechanical properties. Furthermore, due to a lack of general mechanical properties, fracture knowledge and valid fracture toughness results on PMMCs, further work is really necessary on tensile, fatigue, compression, shear, and fracture toughness tests. Some of these tests could include :

- a. Tensile testing at different strain rates.
- b. Toughness testing using either the Charpy test or the four-point bend test. It is believed that this material will possess good toughness.
- c. Elevated temperature testing to explore potential uses in high temperature environment, especially because this material is mostly aimed for use in aerospace structural components. This may include creep testing.
- d. Following some common testing used for aerospace applications, fatigue testing under cyclic loading would be fruitful to evaluate the performance of the material in service.

e. Even though some of these tests have already been done, further wear testing and corrosion resistance testing should be of interest for use of this material in abrasive and marine environment.

The carbon diffusion process may also be further explored by saturating the Ti matrix with C by the addition of free carbon. A comprehensive study of the grain growth of the TiC phase in Ti can be carried out in order to better understand the behaviour of the two materials as well as the coarsening process. Furthermore a TEM study would be of interest in detecting other phases such as  $Ti_2C$  platelets within TiC grains along grain boundaries and, therefore, study their effect on C diffusion especially in terms of activation energy.

The mechanical properties could be evaluated as a function of ceramic particle size, as well as size distribution. Regarding deformation and fracture mechanics in PMMCs, our knowledge is still limited. Although a full range of PMMC types have not yet been examined, the toughness tests already carried out indicate that existing test procedures for the plane strain fracture toughness of metallic materials are suitable for PMMCs with some modifications. To date, insufficient specimens have been tested to allow specific guidelines to be developed for all PMMCs. The most severe restriction to the use of existing standards is likely to be that owing to the effects of crack curvature. Further research is required to quantify the extent of curvature and its dependence on residual stresses, particularly the development of test techniques which would result in straighter crack fronts, either by mechanical stress relief or changes in testpiece design. Other problems are accurate measurements of modulus which are required for crack length measurements.

Finally, all the above suggestions may be applied to the aerospace Ti-6Al-4V/TiC metal matrix composite.

1. KEMPTON H.R., History of Powder Metallurgy, in Metals Handbook, 9th edition, v7, Powder Metallurgy, p.14-20, 1984
2. PHILIP S.W., Metal Matrix Composite : manufacturing Challenges, Tech. Pap. Soc. Manuf. Eng. 1985, Pap. EM85-106, p.11, 1985
3. FOLTZ V.J., Powder Metallurgy Metal Matrix Composites - Overview, Powder Metallurgy in Aerospace and Defense technologies proc., PM Aerosp. Def., 1991.
4. TAYA, M., ARSENAULT R.J., MMCs-Thermomechanical Behaviour, Pergamon Press, 6, 1989.
5. CHOU, T.W.; KELLY,A.; OKURA,A, Composites, v16, 187, 1986.
6. FINE, M.E., Dispersion strengthened Aluminum Alloys, edited by Y.M. Kim and W. Griffith ( The Metallurgical Society, Warrendale, PA), 103, 1988.
7. MURTY G.S.; KOCZAK, M.J. and FRAZIER W.E., scripta metall., v21, 141, 1987.
8. FRAZIER, W.E. and THOMPSON J.J., Dispersion Strengthened Aluminum Alloys, edited by Y.M. Kim and W. Griffith (The Metallurgical Society, Warrendale, PA), 573, 1988.
9. JOHNSON, R.E., J. Phys. Chem., v63, p.1655, 1959.
10. RACK, Henry J., MMCs, Advanced Materials and Processes, v7, p.23, 1989.
11. TURNER, P.S., J. Res. NBS, v37, p.239, 1946.
12. GEIGER A.L. and JACKSON M., Adv. Mater. Process., v7, 23, 1989
13. HASHIM, J. and SHTRIKMAN, J.,J. Mech, phys. Solids, v11, p.127, 1963.
14. J.Mat. Science, v23, p.1139, 1991
15. Engineering Properties of Selected Ceramic Materials, Batelle Memorial Institute (The American Ceramic Society, Ohio, 1966)
16. STEELMAN, T.E.; BAKALYAR, A.D. and KOROPKA, L., Aluminum Matrix Composite Structural Design Development, AFWAL-TR-86-3087, March 1987.
17. RIZZITANO F.J., ISSEROW S. and MALATESTA W.C., Powder Metallurgy in Defense Technology, v3, MPIF, Princeton, N.J., p.61-65, 1977
18. FROES F.H., Aerospace Materials for the Twenty-First Century, Swiss Materials, v2, 1990, p.23
19. COLUCCI F., Hypersonic Materials, Aerospace Composites and Materials, v3, 1991, p.4
20. DOYCHAK J., Metal- and Intermetallic-Matrix Composites for Aerospace Propulsion and Power Systems, Journal of Metals, v44, p.46-51, June 1992

- 
21. JOHNSON A.M., and WRIGHT P.K., Application of Advanced Materials to Aircraft Gas Turbine Engines (AIAA 90-2281), 1990
  22. RONALD T.M.F., Overview of NASP Materials and Structures Programs, NASA CP 10082, p.1-3, 1991
  23. GUZEI L.S., SOKOLOVSKAYA E.M., TSCHUNICHINA L.L., SHULEPOV V.I. and TSHEMLEVA T.A., The Interaction between Titanium Alloys and SiC-fibers, Proc. of the 9th Int. Conf. on Titanium, ed. by KINAWA H. and IZUMI O., v3, 1980
  24. BORISOVA A.L., MARTSENYUK I.S. and TURKEVICH V.Z., Effect of the Dispersion of Silicon Carbide on the Nature of Interaction of the Components of the Ti-SiC System, Soviet Powder Metallurgy and Metal Ceramics, v27, n10, p.799-802, March 1989
  25. CHOI S.K., CHANDRASEKARAN M. and BRABERS M.J., Interaction between Titanium and SiC, Journal of Materials Science, v25, p.1957-1964, 1990
  26. MASSALSKI T.B., Binary Alloy Phase Diagrams, ASM, 1986
  27. STORMS E.K., "Refractory Materials", v2, The Refractory Carbides, Academic Press, N.Y., 1967
  28. JAFFEE R.I., OGDEN H.R. and MAYKUTH D.J., Trans. AIME, v188, p.1261-1266, 1950
  29. CADOFF I. and NIELSEN J.P., Trans. AIME, v197, p.248-252, 1953
  30. EHRLICH P., Z. Inorg. Chem., v259, p.1-41, 1949
  31. GOLDFHOFF R.M., SHAW H.L., CRAIGHEAD C.M. and JAFFEE R.I., Trans. ASM, v45, p.953, 1953
  32. STORMS E.K., Refractory Materials, Volume 2, "The Refractory Carbides", Academic Press, New-York, New-York, 1967, p.6
  33. WEIJIE LIU, Precipitation of Ti(CN) in Austenite : Experimental results, analysis and modelling, Master's thesis, Department of Mining and Metallurgical Engineering, McGill University, Montreal, Canada, July 1987
  34. FROES F.H., Production of Titanium Powder, in Metals Handbooks, 9th edition, v7, p.164, 1984.
  35. MUNSON M.C., Events and Trends in Metal and Mineral Commodities, Journal of Metals, p.22-28, April 1993
  36. ELOFF C. Peter, Production of Metal Carbides, in Metals Handbooks, v7, 158, 1984.
  37. GOETZEL G.C., Cermets, in Metals Handbook, v7, 9th edition, p.806, 1984.
  38. BUDWORTH D.W., An Introduction to Ceramic Sciences, Pergamon Press, N.Y., 1970
  39. METCALFE A.G. and KLEIN M.J., in Titanium Science and Technology, Jaffee R.I. and Burke H.M. eds., Plenum Press, NY, p.2285, 1973
  40. KENNEDY J. and GESCHWIND G., *ibid*, p.2299

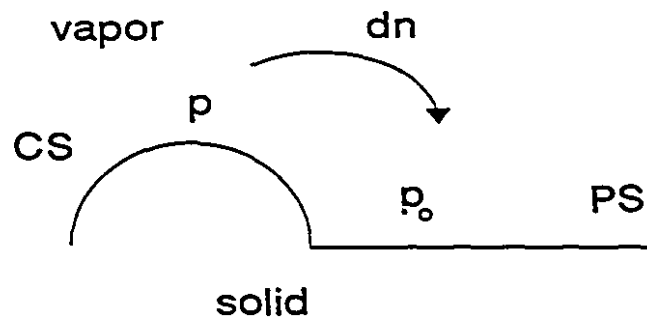
41. ABKOWITZ S. and WEIHRACH P., Adv. Mater. Proc., v31, p.136, July 1989
42. PANCHAL J.M. and VELA T., Wear Resistant Titanium-Titanium Carbide Composites for Lightweight Applications, Advances in Powder Metallurgy, v2, p.497-515,
43. XIA Z. and DENG Z., Sintered Titanium-Titanium Carbide Alloy, Modern Developments in Powder Metallurgy, Proc. of the Int. P/M Conf., v17, Publ. by MPIF, Princeton, NJ, p.569-576, 1984
44. SHANG J.K. and RITCHIE R.O., Monotonic and cyclic crack growth in a TiC-Particulate-Reinforced Ti-6Al-4V Metal-Matrix Composite, Scr. Metall. et Mat., v24, p.1691-1694, Sep 1990
45. KONITZER D.G. and LORETTO M.H., Microstructural Assessment of Ti6Al4V-TiC Metal-Matrix Composite, Mater. Sci. Tech., v5, p.627-631, 1989
46. ASM Committee on Physical Fundamentals of Consolidation, Physical Fundamentals of Consolidation, in Metals Handbook, 9th edition, v7, Powder Metallurgy, p.308-321, 1984
47. HECKEL, R.W., Diffusional Homogenization of Compacted Blends of Powders, Powder Metallurgy Processing, Kuhn, H.A. and Lawley, A., ed. Academic Press, N.Y., p.51-97, 1978
48. GERMAN R.M., Powder Metallurgy Science, MPIF, Princeton, N.J., 1984
49. EXNER, H.E., Principles of Single Phase Sintering, Reviews Powder Met. Phys. Ceram., v1, p.7-251, 1979
50. THUMMLER, F., and THOMMA, N., "The Sintering Process", Metall. Reviews, v12, p.69-108, 1967
51. ZWEBEN C., Metal Matrix Composites - an Overview, Carbide & Tool Journal, v20, p.7-10, Jul-Aug 1988
52. JONES, H., Rapid Solidification of Metals and Alloys, Monograph Series no. 8 (The Institute of Metallurgists), 1982.
53. Rapidly Solidified (RS) Aluminum Alloys - Status and Prospects, NMAB-S68 (National Academy press, Washington D > C >), 1981.
54. ELKABIR, G.; RABENBERG, L.K.; PERSAD, C. and MARCUS, H.L., Scripta Metall., v20, p.1411, 1986.
55. PERSAD, C.; RAGHNATHAN, S; LEE, B.H.; BOUREL, D.L.; ELIEZER, Z. and MARCUS, H.L., Mater. Res. Soc. Symp. Proc, v120, p.23, 1988.
56. GERNOT H.G., Titanium Powder Metallurgy and Composites, Proc. of the 4th Int. Conf. on Titanium, "Titanium '80", Journal of Science and Technology
57. ANDERSON P.J. and ELOFF P.C., Proc. on Titanium Powder Metallurgy Symp., Las Vegas, 1980.
58. HERBELL, T.P. and GLASGOW, T.K., NASA, DOE Highway Vehicle Systems Contractors Coordination Meeting, Dearborn, Michigan, October 17-20, 1978
59. ASTM C373-72, "Standard Test Method for Water Absorption, Bulk Density, Apparent Porosity, and Apparent Specific Gravity"

- 
60. WASHBURN E.W., Note on a Method of Determining the Distribution of Pore Sizes in a Porous Material, Proc. Nat. Acad. Sci., v7, p.115-116, 1921
61. ROOTARE H.M., A Review of Mercury Porosimetry, Advanced Techniques in P/M, Perspectives in P/M, v5, Plenum Press, N.Y., 1970
62. GOLDSTEIN J.I., NEWBURY D.E., ECHLIN P., JOY D.C., FIORI C. and LIFSHIN E., Scanning Electron Microscopy and X-ray Microanalysis, 2nd edition Plenum Press, N.Y., 1984
63. "Determining Average Grain Size", E 112, ASTM Vol.03.03, Philadelphia, 1984.
64. "Standard Test Methods for Microhardness of Materials", E 384, ASTM, Philadelphia, 1984, p.497-518.
65. SARIAN S., J. Appl. Phys, v41, p.4476, 1970
66. SARIAN S., J. Appl. Phys., v39, p.3305, 1968
67. TOKAR K., OEL H. and ILLIGEN A., Ber. Deut. Garam. Ges., v43, p.163, 1966
68. VILK U.N., Poroshkovaya Metallurgiya, v6, p.70-74, 1978

# Appendices

APPENDIX 1 : THOMSON-FREUNDLICH EQUATION

Let  $p_0$  and  $p$  be the vapour tension on the planar surface (PS) and on the convex surface (CS) respectively (assumption :  $p > p_0$  if convex surface):



Also,  $\mu_{sc}$  and  $\mu_{sp}$  are the chemical potentials. If  $p > p_0$ , there is transport of atoms by the vapour phase. For  $dn$  moles transported,

$$dG = \mu_{sc} dn_{sc} + \mu_{sp} dn_{sp} = (\mu_{sp} - \mu_{sc}) dn \quad (1)$$

however,

$$\mu = \mu^0 + RT \ln P \quad (2)$$

therefore,

$$dG = dn \cdot RT \ln \frac{P_0}{P} = -dn \cdot RT \ln \frac{P}{P_0} \quad (3)$$

## APPENDICES

---

Moreover,

$$dG = \gamma dS \quad (4)$$

From geometry of curves we have

$$dS = -dV \left( \frac{1}{R_1} + \frac{1}{R_2} \right) \quad (5)$$

Equation (4) becomes :

$$dG = -\gamma dV \left( \frac{1}{R_1} + \frac{1}{R_2} \right) \quad (6)$$

If  $\Omega_m$  is the molar volume, we have  $dV = \Omega_m dn$  and therefore :

$$dG = -\Omega_m dn \left( \frac{1}{R_1} + \frac{1}{R_2} \right) \cdot \gamma \quad (7)$$

By setting equal equation (3) and (6), we have

$$\ln\left(\frac{P}{P_0}\right) = \frac{\gamma \Omega_m}{RT} \left( \frac{1}{R_1} + \frac{1}{R_2} \right) = \frac{\gamma \Omega}{kT} \left( \frac{1}{R_1} + \frac{1}{R_2} \right) \quad (8)$$

with  $\Omega_m = N\Omega$  ( $\Omega$  atomic volume) and  $R = Nk$  ( $R$  gas constant).

As  $p \approx p_0$ , we can choose to write  $p = p_0 + \Delta p$   
Therefore,

$$\frac{\Delta P}{P_0} = \frac{\gamma \Omega}{kT} \left( \frac{1}{R_1} + \frac{1}{R_2} \right) \quad (9)$$

Equation (9) is the Thomson-Freundlich equation.

## APPENDICES

---

The first assumption  $p > p_0$  (convex surface) can be easily verified for a point on a sphere ( $R_1 = R_2 = R$ ) :

$$\frac{\Delta P}{P_0} = \frac{2\gamma\Omega}{kTR} > 0 \quad (10)$$

A more complex calculation would be needed to prove that a similar equation is obtained for difference in concentration ( $C > C_0$  for convex surface) :

$$\frac{\Delta C}{C_0} = -\frac{\gamma\Omega}{kT} \left( \frac{1}{R_1} + \frac{1}{R_2} \right) \quad (11)$$

APPENDIX 2 : THEORY OF SINTERING TRANSPORT MECHANISMS

Group	Mechanisms	Laws	$K_i$
$\frac{\Delta L}{L_0} = 0$	Surface transport Evaporation-Condensation	$\frac{X^3}{R} = K_1 t$	$(\frac{3P_0\gamma}{d^2})(\frac{\pi}{2})^{\frac{1}{2}}(\frac{M}{kT})^{\frac{3}{2}}$
	Surface diffusion	$\frac{X^7}{R^3} = K_2 t$	$56(\frac{\gamma\Omega D_s \delta_s}{kT})$
	Volume diffusion	$\frac{X^5}{R^2} = K_3 t$	$\frac{5\pi}{2}(\frac{D_v \gamma \Omega}{kT})$
$\frac{\Delta L}{L_0} \neq 0$	Bulk transport Viscous flow	$\frac{X^2}{R} = K_4 t$	$\frac{3\gamma}{2\eta}$
	Volume diffusion	$\frac{X^5}{R^2} = K_5 t$	$20\pi(\frac{D_v \gamma \Omega}{kT})$
	Intergranular diffusion	$\frac{X^6}{R^2} = K_6 t$	$96(\frac{\gamma\Omega D_B \delta_B}{kT})$

where  $\Delta L/L_0$  represents the shrinkage or approach of the centres of the particles.

APPENDIX 3 : SEDIMENTATION PRINCIPLES

Basic Principles

The Sedigraph instrument determines, by means of a finely collimated beam of X-rays, the concentration of particles remaining at decreasing sedimentation depths as a function of time. The process consists of pumping the dispersed powder into a glass cell. Then the particles are allowed to settle at different velocities according to their respective diameters. As the suspension settles, the mass of the particles in the suspension decreases, and the intensity of the X-ray beam increases. As settling proceeds, large particles settle faster than small ones. After a given time ( $t_i$ ), all particles larger in diameter than  $D_i$  have settled below the level of the X-ray beam. The concentration of particles at the X-ray beam level is equal to the original concentration of particles, minus all particles with  $D \geq D_i$ .

The logarithm of the difference in transmitted X-ray intensity is electronically generated, scaled, and presented linearly as "Cumulative Mass Percent" on the Y axis of an X-Y recorder. The instrument typically yields a particle diameter distribution over the range 50 to 0.1  $\mu\text{m}$ .

Theory

Sedimentation is based on that the measured equilibrium velocity of a particle through a viscous medium, resulting from the action of the gravitational force, is related to the size of the particle by Stokes' law. For spherical particles, Stokes' law is expressed by

$$D = Av^{\frac{1}{2}} = \left[ \frac{18\eta}{(\rho - \rho_0)g} \right]^{\frac{1}{2}} v^{\frac{1}{2}} \quad (12)$$

where  $D$  is the diameter of the spherical particle,  $v$  its equilibrium sedimentation velocity, and  $\rho$  its density. The fluid medium is characterized by viscosity  $\eta$  and density  $\rho_0$ ;  $g$  is the acceleration of gravity.

## APPENDICES

---

In practice truly spherical particles are seldom encountered. Since irregular shapes cannot be described by a single linear dimension, it is current practice to specify the size of non-spherical particles in terms of the diameter of a sphere of the same material that would have the same sedimentation velocity. Following this statement, the expression "Equivalent Spherical Diameter" (E.S.D.) has been universally adopted.

By Stokes law, a particle of diameter  $D$  will settle a distance  $h$  in time  $t$  according to the expression

$$D = A \left( \frac{h}{t} \right)^{\frac{1}{2}} \quad (13)$$

where  $A$  is given in equation 4.1. Consequently, after a given time  $t_i$  all particles larger than the corresponding diameter  $D_i$  will have fallen below a given distance  $h$  from the surface of the suspension. If the initial concentration of material was  $C_0$  g/ml, and the concentration after time  $t_i$  at distance  $h$  is  $C_i$  g/ml, then  $P_i$ , the weight percent of material finer than  $D_i$ , is given by

$$P_i = 100 \left( \frac{C_i}{C_0} \right) \quad (14)$$

By obtaining values of  $C_i$  after various times, the corresponding values of  $P_i$  and  $D_i$  may be calculated, which when plotted yield a cumulative distribution of particle size in terms of Stokes E.S.D.

APPENDICES

---

APPENDIX 4 : ARCHIMEDEAN RELATIVE DENSITY DATA

Table A4.1 Relative densities (%) at 1300°C

1300°C	0.5 hour	1 hour	2 hours	4 hours
0%n.a. <sup>1</sup>	77.1	78.0	86.5	76.7
0%	82.2	85.4	96.1	89.9
2.5%	81.0	85.2	93.0	99.4
5%	84.6	86.1	94.5	95.0
10%	82.0	81.8	92.0	93.6
15%	79.2	81.5	92.5	93.4
20%	78.6	80.7	89.8	91.2

Table A4.2 Relative densities (%) at 1350°C

1350°C	0.5 hour	1 hour	2 hours	4 hours
0%n.a.	81.3	81.2	87.3	89.1
0%	84.5	89.9	95.5	92.8
2.5%	87.9	88.2	94.4	96.0
5%	86.3	88.4	96.2	97.5
10%	83.3	86.7	93.9	95.0
15%	82.9	85.8	93.5	95.5
20%	82.1	84.7	90.1	92.8

---

<sup>1</sup> n.a. = non attrition milled

APPENDICES

---

Table A4.3 Relative densities (%) at 1400°C

1400°C	0.5 hour	1 hour	2 hours	4 hours
0% <i>n.a.</i>	81.9	85.5	94.3	89.5
0%	88.6	90.1	96.4	89.5
2.5%	88.3	90.2	95.6	95.8
5%	88.7	89.8	96.2	95.6
10%	87.1	86.7	95.1	95.6
15%	86.7	88.1	96.9	95.6
20%	84.3	86.6	93.8	95.0

Table A4.4 Relative densities (%) at 1440°C

1440°C	0.5 hour	1 hour	2 hours	4 hours
0% <i>n.a.</i>	81.00	88.3	96.1	92.2
0%	86.7	92.5	97.1	97.3
2.5%	88.5	94.6	95.6	93.8
5%	88.6	92.6	96.1	93.8
10%	83.7	90.7	95.2	93.5
15%	82.4	90.6	95.5	93.1
20%	82.2	89.9	94.1	92.7

APPENDICES

---

Table A4.5 Relative densities (%) at 1480°C

1480°C	0.5 hour	1 hour	2 hours	4 hours
0%n.a.	91.0	88.4	80.1	77.0
0%	94.9	95.3	97.2	94.0
2.5%	94.1	96.0	97.0	93.8
5%	96.4	96.0	97.9	94.8
10%	94.9	95.2	97.3	94.0
15%	93.8	88.8	96.5	92.3
20%	92.8	95.0	96.1	94.5

Table A4.6 Relative densities (%) at 1520°C

1520°C	0.5 hour	1 hour	2 hours	4 hours
0%n.a.	83.1	80.3	79.0	76.7
0%	88.3	85.8	88.1	93.2
2.5%	93.3	95.3	96.0	96.2
5%	93.0	96.0	98.9	94.0
10%	92.1	95.9	93.6	93.7
15%	92.2	95.7	96.0	90.9
20%	91.2	95.1	95.3	93.4

APPENDICES

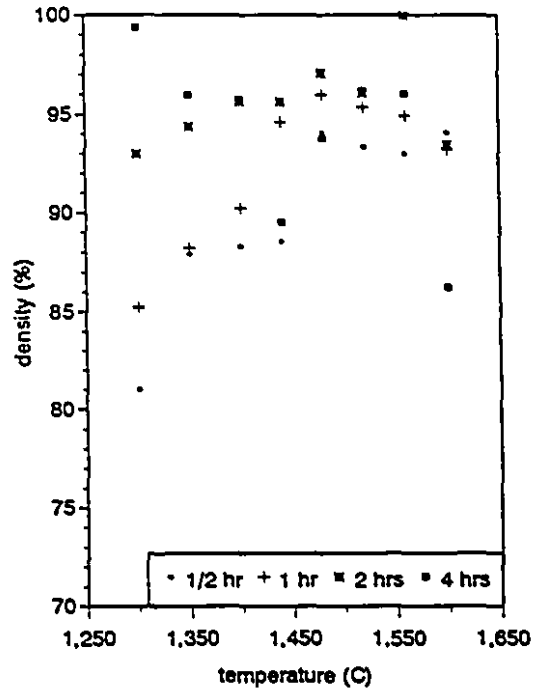
---

Table A4.7 Relative densities (%) at 1560°C

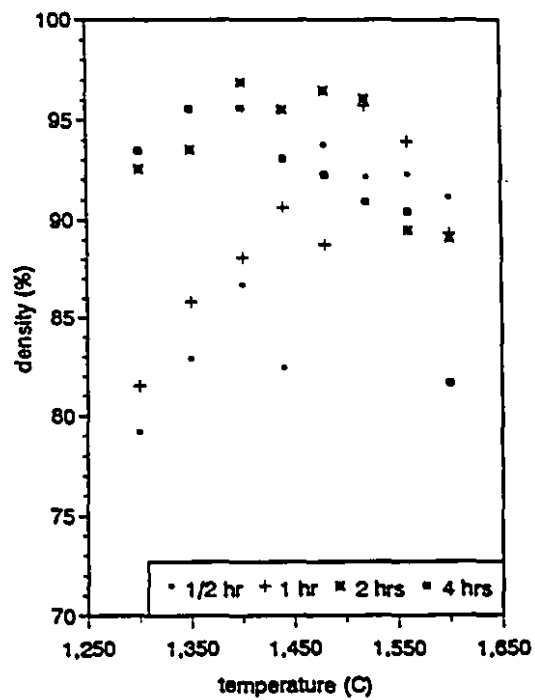
1560°C	0.5 hour	1 hour	2 hours	4 hours
0% <i>n.a.</i>	82.0	79.6	89.1	76.1
0%	88.2	84.0	90.7	86.3
2.5%	93.0	94.9	99.9	96.0
5%	92.2	96.1	94.9	94.7
10%	92.0	94.9	92.7	93.9
15%	92.3	93.9	89.5	90.4
20%	92.5	94.1	92.7	93.7

Table A4.8 Relative densities (%) at 1600°C

1600°C	0.5 hour	1 hour	2 hours	4 hours
0% <i>n.a.</i>	81.5	78.8	77.9	74.7
0%	92.8	91.1	91.6	84.3
2.5%	94.7	93.2	93.4	86.2
5%	94.1	93.5	92.3	82.5
10%	93.2	92.3	88.9	81.7
15%	91.1	89.3	89.1	81.7
20%	90.9	90.8	87.4	85.9



(a)



(b)

Figure A4.1 - Density vs temperature for (a) 2.5% (b) 15%

APPENDICES

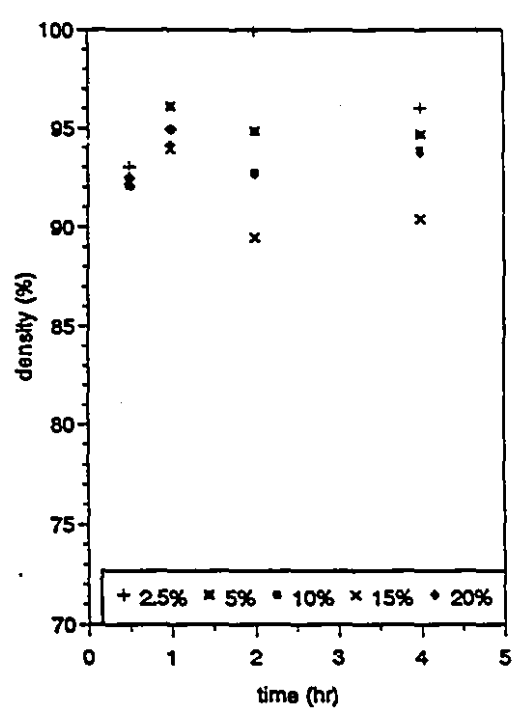
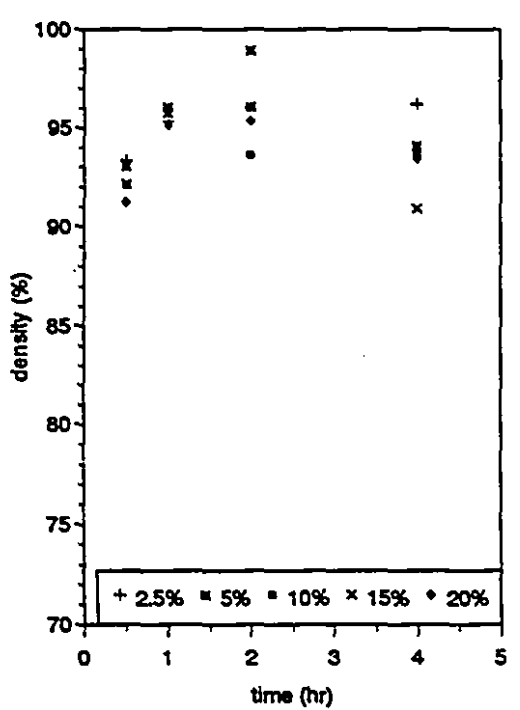
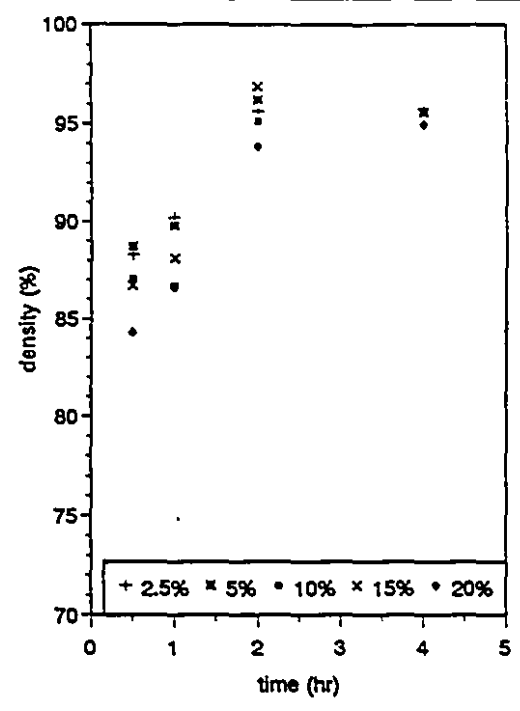
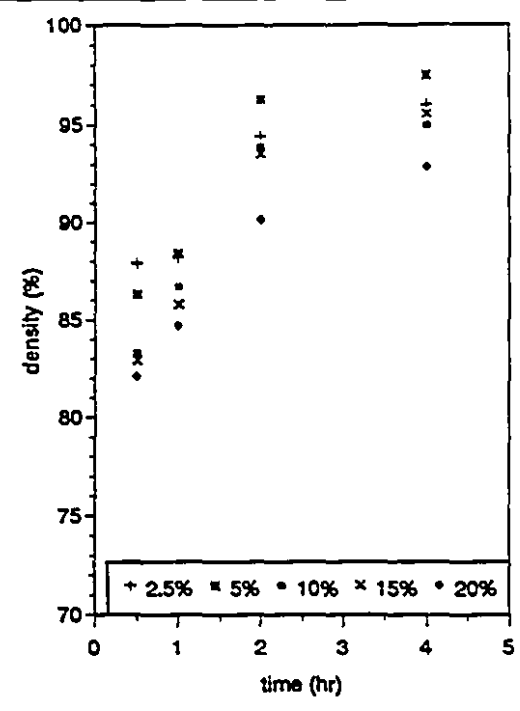


Figure A4.2 - Density vs time for (a) 1350°C (b) 1400°C (c) 1520°C (d) 1560°C

APPENDICES

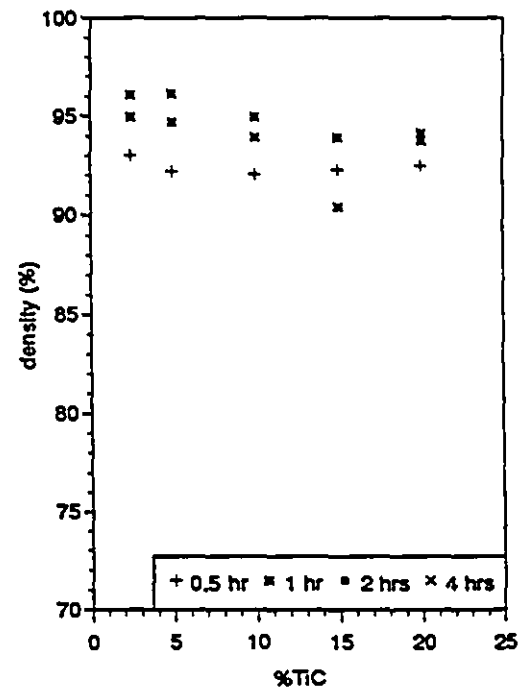
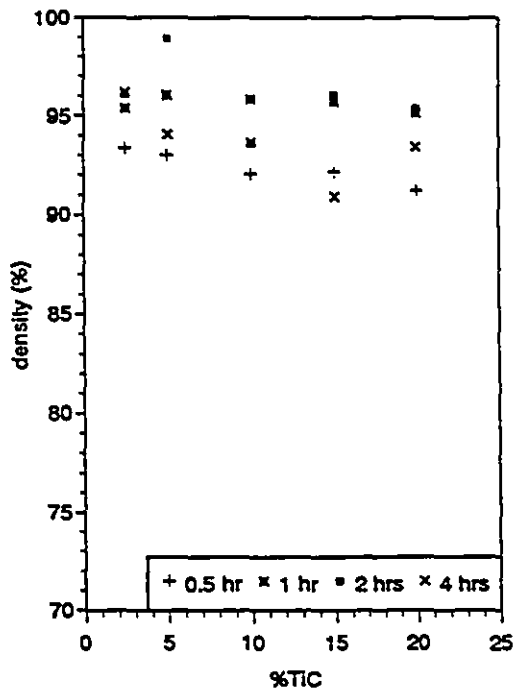
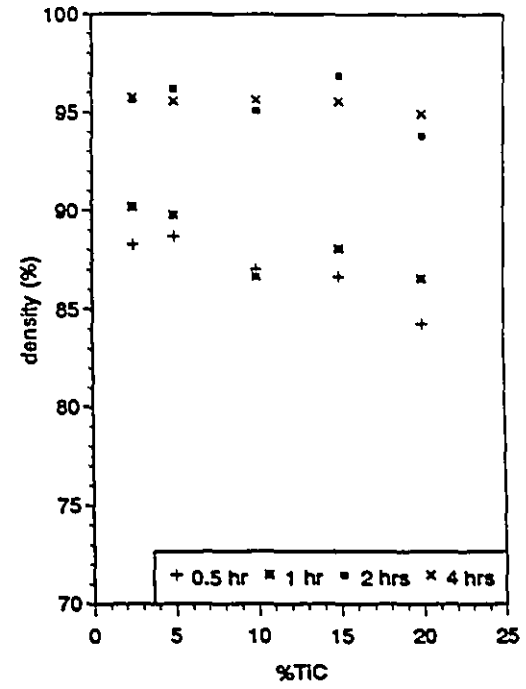
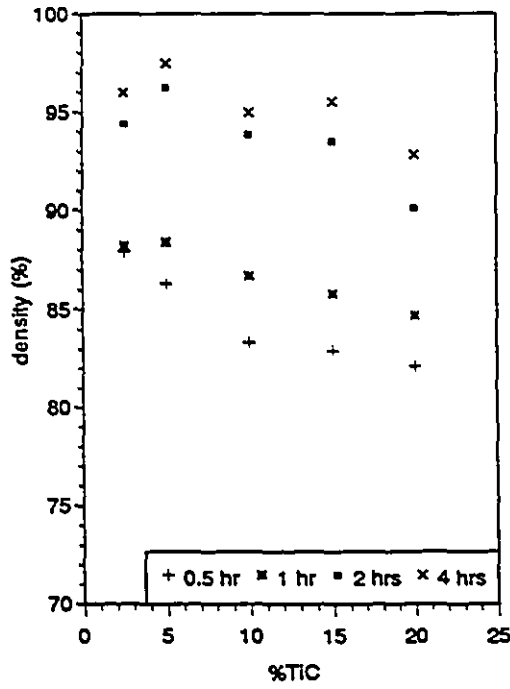


Figure A4.3 - Density vs %TiC for (a) 1350°C (b) 1400°C (c) 1520°C (d) 1560°C

APPENDICES

---

**APPENDIX 5 : COMPARISON OF RELATIVE DENSITIES MEASURED BY ARCHIMEDEAN METHOD AND BY IMAGE ANALYSIS**

**Table A5.1 - Comparison of relative densities measured by Archimedean method (on the left in %) and by Image analysis (on the right in %) at 1300°C**

1300°C	0.5 hour		2 hours		4 hours	
0%	82.2	84.2	96.1	97.9	89.9	99.9
2.5%	81.0	83.6	93.0	97.6	99.4	99.3
5%	84.6	87.2	94.5	99.8	95.0	99.1
10%	82.0	84.6	92.0	98.8	93.6	99.0
15%	79.2	81.8	92.5	98.0	93.4	98.3
20%	78.6	80.6	89.8	95.3	91.3	96.8

**Table A5.2 - Comparison of relative densities measured by Archimedean method (on the left in %) and by Image analysis (on the right in %) at 1440°C**

1440°C	0.5 hour		2 hours		4 hours	
0%	86.7	87.3	97.1	99.9	97.3	99.4
2.5%	88.5	91.1	95.6	99.9	93.8	99.7
5%	88.6	90.0	96.1	99.4	93.8	99.7
10%	83.7	89.5	95.2	99.4	93.5	98.3
15%	82.4	89.1	95.5	99.8	93.1	97.8
20%	82.2	88.6	94.1	98.5	92.7	97.1

APPENDICES

---

Table A5.3 - Comparison of relative densities measured by Archimedean method (on the left in %) and by Image analysis (on the right in %) at 1480°C

1480°C	0.5 hour		2 hours		4 hours	
0%	94.9	95.1	97.2	98.1	94.0	98.4
2.5%	94.1	97.8	97.0	99.4	93.8	98.7
5%	96.4	99.7	97.9	99.9	94.8	99.5
10%	94.9	98.6	97.3	99.3	94.0	99.0
15%	93.8	97.6	96.5	98.7	92.3	97.2
20%	92.8	96.4	96.1	98.1	94.5	94.0

Table A5.4 - Comparison of relative densities measured by Archimedean method (on the left in %) and by Image analysis (on the right in %) at 1600°C

1600°C	0.5 hour		2 hours	
0%	92.8	98.8	91.6	97.6
2.5%	94.7	99.9	93.4	99.7
5%	94.1	99.9	92.3	99.6
10%	93.2	99.3	88.9	98.7
15%	91.1	97.0	89.1	98.4
20%	90.9	96.4	87.4	94.9

APPENDICES

---

APPENDIX 6 : MICROHARDNESS DATA

Table A6.1 - Vickers Microhardness of the TiC phase in Ti-2.5wt%TiC

T (°C)	1/2 hr	2 hrs	4 hrs
1300	1450 ± 164	1304 ± 174	1101 ± 200
1440	1320 ± 213	1087 ± 167	982 ± 101
1600	1032 ± 82	1074 ± 91	1025 ± 259

Table A6.2 - Vickers Microhardness of the Ti matrix in Ti-2.5wt%TiC

T (°C)	1/2 hr	2 hrs	4 hrs
1300	253 ± 81	409 ± 67	429 ± 102
1440	276 ± 138	542 ± 38	514 ± 98
1600	470 ± 26	489 ± 35	439 ± 178

Table A6.3 - Vickers Microhardness of the TiC phase in Ti-5wt%TiC

T (°C)	1/2 hr	2 hrs	4 hrs
1300	1661 ± 136	1623 ± 128	1121 ± 149
1440	1171 ± 44	1078 ± 33	1070 ± 31
1600	1015 ± 37	942 ± 60	775 ± 93

APPENDICES

---

Table A6.4 - Vickers Microhardness of the Ti matrix in Ti-5wt%TiC

T (°C)	1/2 hr	2 hrs	4 hrs
1300	245 ± 5	245 ± 11	259 ± 9
1440	428 ± 7	446 ± 13	486 ± 13
1600	544 ± 6	547 ± 7	615 ± 43

Table A6.5 - Vickers Microhardness of the TiC phase in Ti-10wt%TiC

T (°C)	1/2 hr	2 hrs	4 hrs
1300	1636 ± 99	1414 ± 144	1052 ± 118
1440	1170 ± 29	1124 ± 46	993 ± 57
1600	1039 ± 89	858 ± 67	794 ± 64

Table A6.6 - Vickers Microhardness of the Ti matrix in Ti-10wt%TiC

T (°C)	1/2 hr	2 hrs	4 hrs
1300	258 ± 5	257 ± 6	316 ± 9
1440	269 ± 5	277 ± 5	386 ± 10
1600	343 ± 8	346 ± 7	564 ± 112

APPENDICES

---

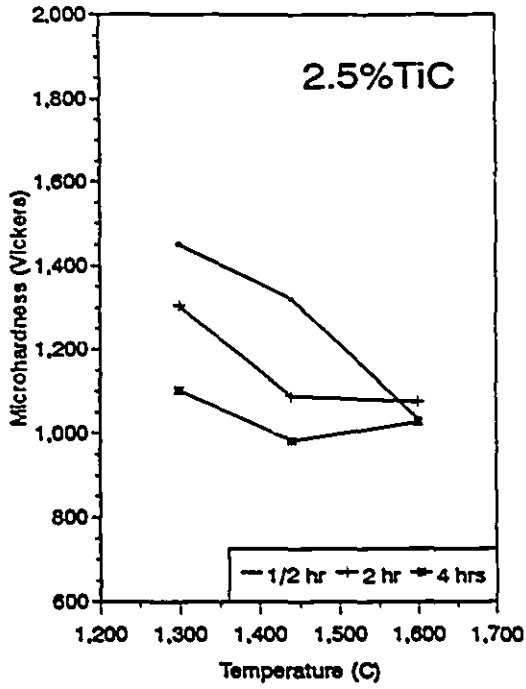
Table A6.7 - Vickers Microhardness of the TiC phase in Ti-20wt%TiC

T (°C)	1/2 hr	2 hrs	4 hrs
1300	1840 ± 196	1407 ± 137	1147 ± 131
1440	1208 ± 49	1075 ± 51	990 ± 24
1600	1190 ± 126	957 ± 78	815 ± 77

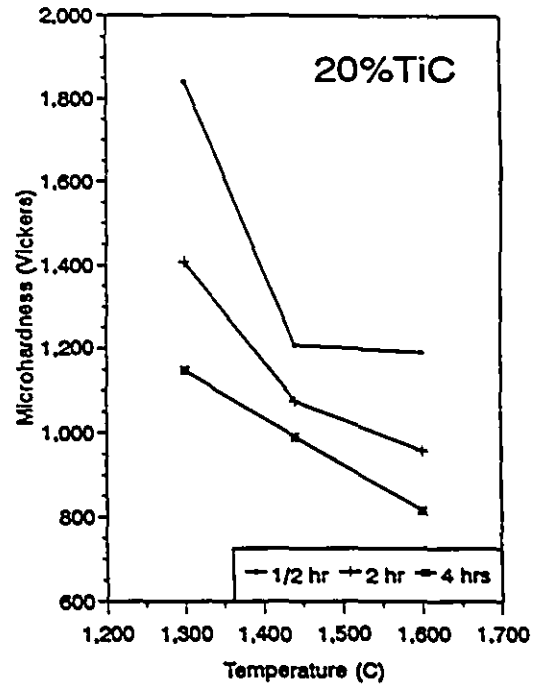
Table A6.8 - Vickers Microhardness of the Ti matrix in Ti-20wt%TiC

T (°C)	1/2 hr	2 hrs	4 hrs
1300	275 ± 9	256 ± 8	241 ± 11
1440	282 ± 6	285 ± 3	358 ± 7
1600	341 ± 12	319 ± 31	431 ± 46

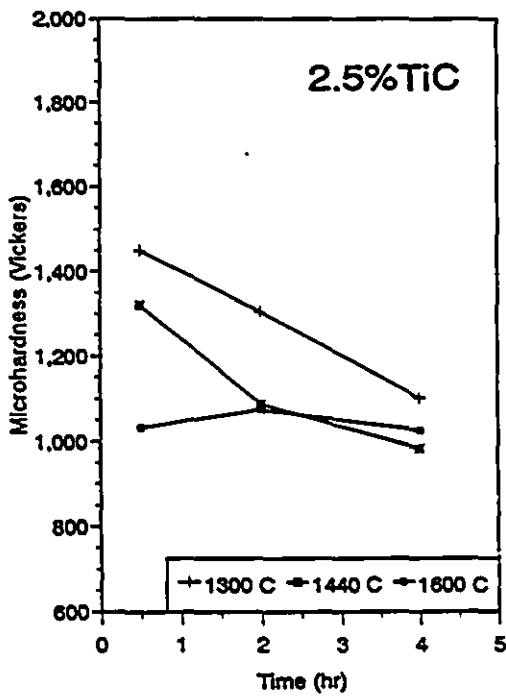
APPENDICES



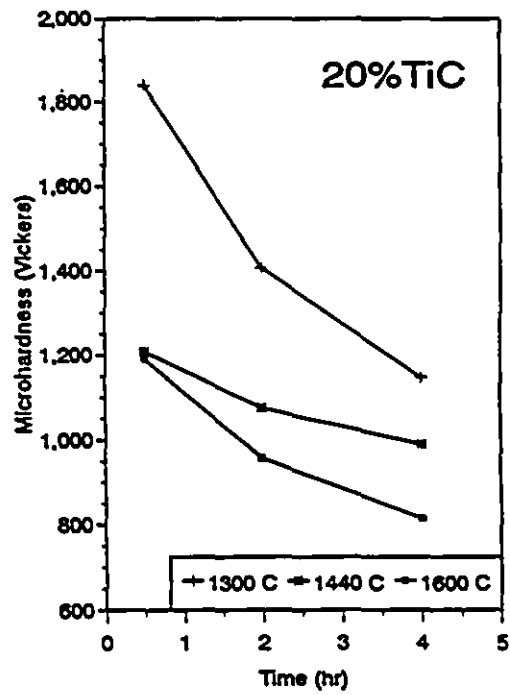
(a)



(b)



(c)



(d)

Figure A6.1 - Microhardness of TiC particles vs temperature for (a) 2.5%TiC and (b) 20%TiC and time for (c) 2.5%TiC and (d) 20%TiC

APPENDICES

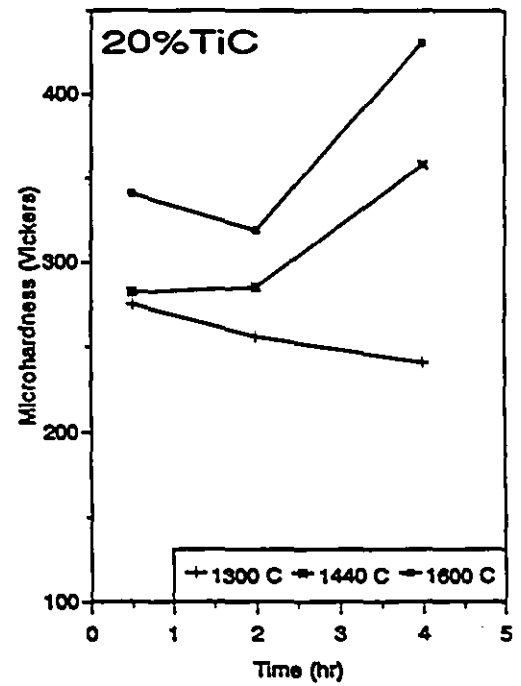
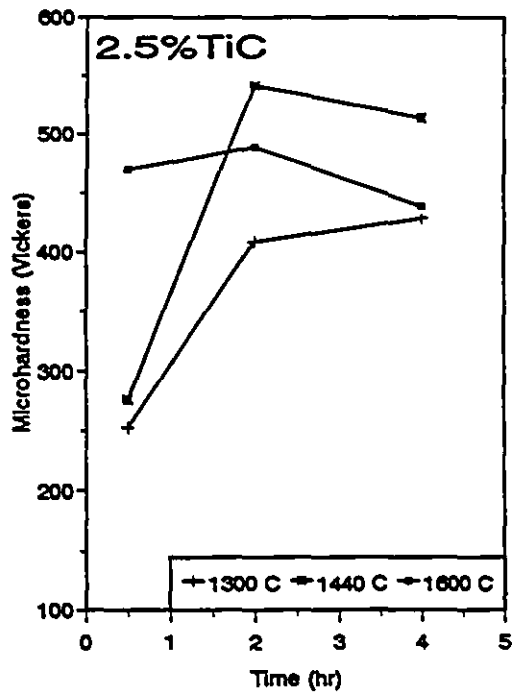
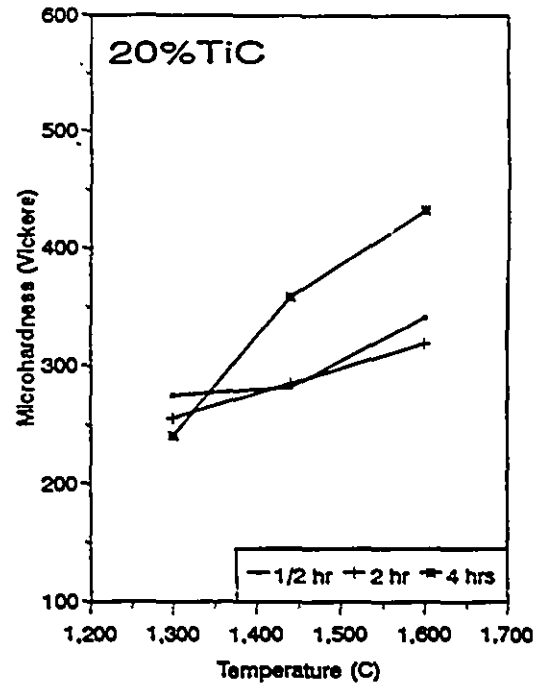
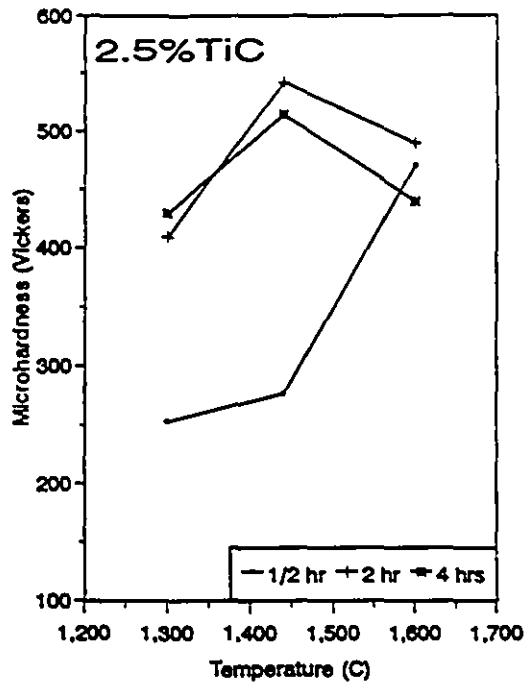


Figure A6.2 - Microhardness of Ti matrix vs temperature for (a) 2.5%TiC and (b) 20%TiC and time for (c) 2.5%TiC and (d) 20%TiC